CHARACTERISTICS OF SOUND RADIATION FROM TURBULENT PREMIXED FLAMES

A Dissertation
Presented to
The Academic Faculty

by

Rajesh Rajaram

In Partial Fulfillment
of the Requirements for the Degree of
Doctor of Philosophy
Aerospace Engineering

Georgia Institute of Technology

December 2007

CHARACTERISTICS OF SOUND RADIATION FROM TURBULENT PREMIXED FLAMES

Approved by

Dr. Timothy Lieuwen, Advisor
Associate Professor
School of Aerospace Engineering
Georgia Institute of Technology

Dr. Krish Ahuja
Associate Professor
School of Aerospace Engineering
Georgia Institute of Technology

Dr. Jerry Seitzman
Associate Professor
School of Aerospace Engineering
Georgia Institute of Technology

Dr. Rick Gaeta
Senior Research Engineer
Georgia Tech Research Institute
Georgia Institute of Technology

Dr. Jeff Mendoza
Installation Aerodynamics & Acoustics
Honeywell Aerospace

Date Approved: 10/09/2007

Dedicated to my family and friends who supported me throughout my doctoral studies

"Being a graduate student is like becoming all of the Seven Dwarves. In the beginning you're Dopey and Bashful. In the middle, you are usually sick (Sneezy), tired (Sleepy), and irritable (Grumpy). But at the end, they call you Doc, and then you're Happy."

- Unknown Origin

ACKNOWLEDGEMENTS

This dissertation could not have been written without the support Dr. Tim Lieuwen, who struck a fine balance as an advisor by allowing me to pursue my wild ideas and theories while ensuring the completion of this project. I express my sincere gratitude to Joshua Gray, who spent countless hours helping me acquire the necessary data. I would also like to acknowledge Yamada and Analisa for their help. I thank my lab engineers David, Andy, John H., Jason, & Bobby and the entire workshop team, without whom this experimental venture couldn't have been completed. I really appreciate Dr. Ahuja, Dr. Seitzman, Dr. Jagoda, and Dr. Neumier for their advice and support all through my doctoral program.

Among others, I would like to thank Santosh H for indulging me with countless coffees and discussions about "life, universe, and everything" that helped shape some of the ideas and theories put forth in this work. I am grateful to my friends and colleagues: Suraj, Muruganandam, and Venkat who provided immense technical and moral support for my work. I would also like to thank my wonderful friends: Madhumitha, Vetriventhan, Thao, and Augustin, fellow A2Zs: Jaya, Pradeep, Ramesh and Shreyas for adding color to what is otherwise called "a graduate student life." I would also like to thank my other friends and/or colleagues: Moshe, Mohan, Suzie, Al, Ben, John Cu., Nori, Saikumar, Antonio, Pritham, Quinguo, Santosh S., Shreekrishna, Akiva, Arun, Brian, Colby, Dmitry, Gopikrishna, Jayaprakash, John Cr., Kapil, Mael, Priya, Ping, Rob, Satyanarayana, Shai, Shashwath, Tom, Tudor, Yash, and Yogish for helping me strike a balance in my life.

I would also like to thank National Science Foundation for their interest and support in this endeavor.

Finally, I would like to thank my family for their continued support.

TABLE OF CONTENTS

LIST OF TABLES

LIST OF FIGURES

NOMENCLATURE

English Symbols

C	gain coefficient characterizing frequency dependence of $L_{f,coherence}$
c_0	speed of sound in far field
c_1	speed of sound in combustion zone
D	diameter of the burner
D_1	inner diameter of the turbulence generator slot
D_2	outer diameter of the turbulence generator slot
F	fuel mass fraction
F_{peak}	peak frequency of acoustic spectrum
f	frequency
f_{cutoff}	cutoff frequency characterizing coherence roll off
H	fuel heating value
k_0	wave number, ω/c_0
k_{cutoff}	wave number characterizing coherence roll off, $2\pi f_{cutoff}/c_0$
$L(r)$	sound pressure level measured at a distance r
L_{ref}	sound pressure level measured by the reference microphone
$L_{f,coherence}$	length scale characterizing the region of high coherence
$L_{f,average}$	length scale characterizing the point of maximum mean heat release rate
$L_{f,variance}$	length scale characterizing the point of maximum heat release rate fluctuations
$L_{f,spread}$	length scale characterizing the spread heat release rate fluctuations
l	integral length scale
m_f	fuel mass flow rate

n	exponent characterizing frequency dependence of $L_{f,coherence}$
P	acoustic power
p	pressure
p_o	far field mean pressure
Q_{char}	characteristic heat release rate
q	unsteady heat release rate per unit volume
R	distance between the microphone and the burner exit
$R(x,y)$	correlation coefficient between two measurement points (x,y)
$R(\tau)$	autocorrelation for a time lag τ
$R_{actual1}$	distance between microphone1 and the origin of combustion noise
$R_{actual3}$	distance between microphone3 and the origin of combustion noise
Re_D	Reynolds number, $U_{ave}D/\nu$
S_L	laminar flame speed
St	Strouhal number
U_{ave}	mean velocity
u	uncertainty
u'	turbulence velocity
t	time

Greek Symbols

α	slope of high frequency side of the acoustic spectrum
β	slope of low frequency side of the acoustic spectrum
$\delta(x)$	Kronecker delta
δ_L	flame thickness
Δf	band width per frequency point of Fourier transform

$\Delta L(\mathrm{r})$	difference sound pressure level between the measurement microphone and the reference microphone
ϕ	equivalence ratio
$\phi_{x,y}$	phase difference between two measurement points (x,y)
γ	ratio of specific heats
$\gamma^2_{x,y}$	coherence between two measurement points (x,y)
η	acoustic efficiency
ν	kinematic viscosity of air
ρ	density
ρ_o	density in ambient far field
τ_{lag}	time lag
ω	angular frequency
ω_{cutoff}	cutoff angular frequency characterizing frequency dependence of $L_{f,coherence}$

Notations

$\hat{..}$	Fourier coefficient
$..^*$	complex compliment
$..{}_0$	values of the ambient fluid
$\bar{..}$	time average
$\langle .. \rangle$	ensemble average

Abbreviations

SPL	Sound Pressure Level
OASPL	Overall Sound Pressure Level
LIF	Laser Induced Fluorescence

SUMMARY

Turbulent combustion processes are inherently unsteady and, thus, a source of acoustic radiation, which occurs due to the unsteady expansion of reacting gases. While prior studies have extensively characterized the total sound power radiated by turbulent flames, their spectral characteristics are not well understood. The objective of this research work is to measure the flow and acoustic properties of an open turbulent premixed jet flame and explain the spectral trends of combustion noise.

The flame dynamics were characterized using high speed chemiluminescence images of the flame. A model based on the solution of the wave equation with unsteady heat release as the source was developed and was used to relate the measured chemiluminescence fluctuations to its acoustic emission. Acoustic measurements were performed in an anechoic environment for several burner diameters, flow velocities, turbulence intensities, fuels, and equivalence ratios. The acoustic emissions are shown to be characterized by four parameters: peak frequency (F_{peak}), low frequency slope (β), high frequency slope (α) and Overall Sound Pressure Level (OASPL).

The peak frequency (F_{peak}) is characterized by a Strouhal number based on the mean velocity and a flame length. The transfer function between the acoustic spectrum and the spectrum of heat release fluctuations has an f^2 dependence at low frequencies, while it converged to a constant value at high frequencies. Furthermore, the OASPL was found to be characterized by $(F_{peak}\ m_f H)^2$, which resembles the source term in the wave equation.

CHAPTER 1

INTRODUCTION

Turbulent combustion processes are inherently unsteady and, thus, a source of acoustic radiation. This phenomenon occurs due to the unsteady expansion of reacting gases at the turbulent flame front. Locally, such an expansion appears as an unsteady creation of volume and behaves like a monopole source. Most practical combustion systems have an underlying turbulent flow that causes random perturbations to the flame. Hence, noise due to combustion is an integral part of the system.

Combustion noise is of interest for several reasons. First, stringent EPA and FAA rules on noise abatement in aircrafts have led to a large number of studies on various noise sources in aircraft systems including the airframe (includes flaps, landing gears, trailing edge other aerodynamic components, etc), the propulsion system (includes propellers, compressors, turbines, combustion/core, exhaust jet, etc), and the presence of the sonic boom in case of supersonic aircrafts. These studies indicate that for gas turbine based propulsion systems and auxiliary power units, combustion noise can be a significant noise source. It has been shown that at low engine speeds, the engine makes substantially more noise in the low frequency regime than that of a free-jet. This is attributed to the combustion noise produced by the system. The aircraft engine is maintained at low speeds during engine idling, taxiing, landing approach and cruise conditions. Thus, for a significant time the aircraft engine is maintained at lower engine speed when the aircraft is in or nearing ground where the noise requirements are stringent. Thus, a thorough understanding of the combustion noise production mechanism can help address this problem at the design phase of the engine.

Power generating gas turbine engines are usually located away from residential areas and hence do not always have to pass these stringent noise requirements. However the noise produced by the flame plays an important role in the dynamics in the combustion system. Combustion is the source for large amplitude oscillations at frequencies associated with natural combustor modes. Furthermore flames under near-lean-blowout conditions are known to produce distinctive acoustic emission when compared to a stable flame,[1] and hence the acoustic signature can be used to recognize the onset of lean-blowout. Thus we can see there is a need to understand how a combustion process produces noise, how to minimize the noise emissions, and also how to relate these noise emissions to combustor health and performance.

The objective of this research work is to measure the flow and acoustic properties of an open turbulent premixed jet flame and explain the measured trends. This study will help supplant the primarily empirical correlations, found in prior studies, with more physics based correlations of the parameters that control combustion noise production.

CHAPTER 2

LITERATURE REVIEW

Theory

Lighthill's theory,[2] for jet noise, laid the foundation for the current understanding of flow and combustion noise. The first explicit analysis and modeling of the source of combustion noise appears to have been performed by Bragg,[3] who treated the fluctuating flame as a monopole source. While this model was heuristic in nature, it laid the foundation for more rigorous analyses by Strahle,[4, 5] Hassan,[6] Chiu & Summerfield,[7] Doak,[8] Kotake,[9] and others. While the works of Chiu & Summerfield,[7] Doak,[8] and Kotake[9] were rigorous in following Lighthill's analogy, their formulation of the wave equation in a reacting flow made the extraction of the source term rather complex. However at low Mach number condition, the expressions for far-field acoustic pressure due to a flame front were quite similar. In order to understand some basic concepts consider the following wave equation with an unsteady heat source:[10]

$$\frac{1}{c_0^2}\frac{\partial^2 p}{\partial t^2} - \nabla^2 p = -\frac{\partial}{\partial t}\left(\frac{\rho_0(\gamma-1)q}{\rho c^2}\right) \quad \textbf{(1)}$$

where p refers to the unsteady pressure, c to the mean speed of sound, ρ is the fluid density, γ to the ratio of specific heats, and q to the rate of heat release per unit volume. The subscript ($_0$) refers to the values in the ambient fluid. For simplicity, Equation 1 does not include the effects of convection due to mean flow and refraction of sound due to temperature inhomogeneities, in order to focus on the effects of unsteady heat addition. Dowling's[11] and Strahle's[12] formulations account for the effects of convection and

refraction of sound. Most importantly, the equation shows that unsteady heat addition acts as an acoustic monopole source.

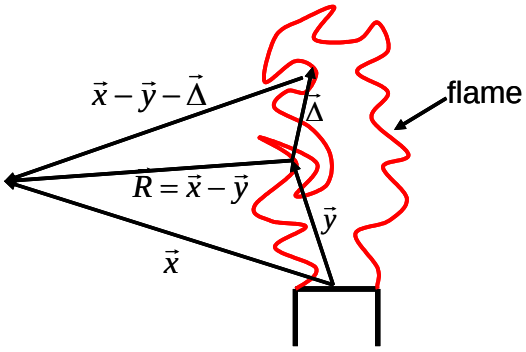

Figure 1 Schematic of turbulent flame and burner illustrating coordinate system used in the description of the acoustic field

The solution for Equation 1 can be written as a volume integral of the unsteady heat release over the combustion region. The coordinate system that is used in the solution is illustrated in Figure 1. In the figure, the points $\vec{y}$ describe the flame region, $\vec{x}$ denotes the "observation point" at which the acoustic emission from the flame is measured, and $\vec{R}$ denotes the vector pointing between the two. The solution of Equation 1 for acoustic pressure in the far-field is given by:[10]

$$\left(p-p_0\right)\left(\vec{x},t\right)=\frac{1}{4\pi\left|\vec{x}\right|}\frac{\partial}{\partial t}\int\left[\frac{\rho_0\left(\gamma-1\right)q}{\rho c^2}\right]_{\left(t-\left|\vec{R}\right|/c_0\right)}d^3y \quad (2)$$

Equation 2 shows that the acoustic pressure at the observation point $\vec{x}$ is related to the unsteady heat release rate integrated over the combustion region at a retarded time ($|\vec{R}|/c_0$) later. For open flames $\rho_0 c_0^2$ (which is a constant) and ρc^2 are approximately equal in value, so the equation can be reduced to the form:[13]

$$\left(p-p_0\right)\left(\vec{x},t\right)=\frac{\left(\gamma-1\right)}{4\pi\left|\vec{x}\right|c_o^2}\int\left.\frac{\partial q\left(\vec{y}\right)}{\partial t}\right|_{\left(t-\left|\vec{R}\right|/c_0\right)}d^3y \quad (3)$$

Hence the Fourier transform of Equation 3 yields:

$$\hat{p}(\vec{x},\omega)=\frac{(\gamma-1)}{4\pi|\vec{x}|c_o^2}\int -i\omega\hat{q}(\vec{y},\omega)e^{ik_0|\vec{R}|}d^3y \quad (4)$$

Thus the overall sound power is:

$$P=\frac{\overline{(p-p_0)^2}}{\rho_0 c_0}4\pi|\vec{x}|^2=\frac{(\gamma-1)^2}{4\pi\rho_0 c_0^5}\int\overline{\frac{\partial q}{\partial t}\left(y,t-{}^{|\vec{x}-\vec{y}|}\!/_{c_0}\right)\frac{\partial q}{\partial t}\left(y+\Delta,t-{}^{|\vec{x}-\vec{y}-\vec{\Delta}|}\!/_{c_0}\right)}d^3\Delta d^3y \quad (5)$$

Equation 5 shows that an accurate prediction of the noise produced by a turbulent flame requires not only a thorough understanding of the distribution of the amplitude heat release fluctuation but also the relative time lags between noise produced from various locations of the flame and the location of measurement. The power spectrum of combustion noise is given by:

$$P(\omega)=\frac{(\gamma-1)^2}{4\pi\rho_0 c_0^5}\omega^2\int\left\langle\hat{q}^*(\vec{y},\omega)\hat{q}(\vec{y}+\vec{\Delta},\omega)\right\rangle e^{-ik_0\left(|\vec{x}-\vec{y}-\vec{\Delta}|-|\vec{x}-\vec{y}|\right)}d^3\Delta d^3y \quad (6)$$

Equation 6 shows that the unsteady pressure measured at the observation point $\vec{x}$, at a frequency ω is due to unsteady heat release processes occurring at the same frequency. The phase term ($e^{-ik_0\left(|\vec{x}-\vec{y}-\vec{\Delta}|-|\vec{x}-\vec{y}|\right)}$) exerts significant influence on combustion noise at high frequencies, when the source becomes acoustically non-compact. Appendix III shows that, even when the sources at different locations become incoherent, this exponent plays a very important role in coherence between various microphone locations and thus will help define the acoustic compactness of the flame zone.

However evaluation of these integrals is not trivial. This requires a complete understanding of the spatial variation of heat release rate fluctuation. At low frequencies, this task is relatively easier because the flame zone is acoustically compact and the heat

release fluctuations are coherent. All these assumptions will fall away quickly as we start evaluating the integral for higher frequencies.

Several attempts have been made to either integrate those using turbulence models while others have tried rudimentary analyses to arrive at expressions for the acoustic efficiency and overall sound pressure level. Bragg[3] introduced the concept of acoustic efficiency with respect to combustion noise that was defined as the ratio of the acoustic power to the heating output of the flame. He tried to group the source term into various dimensionless groups and estimated the acoustic efficiency. He estimated that the efficiency η is of the order of 10^{-6}. This result is quite significant in understanding how small is the acoustic energy radiated by combustion when compared to the actual heat output of the flame. Giammar & Putnam[14] also performed a similar analysis for acoustic efficiency and obtained similar values for acoustic efficiency.

Hassan,[6] Strahle,[15] and others used various turbulence models to estimate the integral. However the deficiencies in turbulence modeling propagated in the combustion noise scaling which led to scaling of spectral parameters either being inadequate or use of correlations for turbulence which led to very combustor specific correlation-based scaling models.

Clavin & Siggia[16] and Clavin[17] presented a fractal analysis of combustion noise that predicted a power law dependence of the spectrum at high frequencies ($f^{-5/2}$). Using Kolmogorov scaling arguments that assumed a $k^{-5/3}$ inertial subrange velocity spectrum and fractal analysis on an acoustically compact, corrugated flame, they arrive at an acoustic power spectrum in the corresponding frequency range with an $f^{-5/2}$ dependence. Huff's[18] analysis predicted an f^{-2} dependence for spray combustion.

However all of the analysis inherently assumed combustion to be a compact source. Kotake[9] recognized the need to understand the correlation between heat release rate oscillations at various locations of a flame. However lack of availability of actual time correlation of heat release fluctuations impeded the progress in that respect. Furthermore it should be noted that the monopole discussed above is only due to the unsteady expansion of gases across the turbulent flame due to heat release fluctuations. On the other hand, Truffaunt *et al*[19] showed that even at low Mach numbers the difference between number of moles of reactants and products could give rise to additional source terms which could be significant in some hydrocarbon-oxygen flames.

Evaluation of Source term

The source term for combustion noise can be evaluated using optical techniques. The light emission due to radicals present in a reaction has been used to measure the heat release fluctuations. Price *et al*[20] made one of the earliest attempts to evaluate the source term of combustion noise. They found that the overall variance of the rate of change of C_2 radical emission correlated well with the overall sound power. Strahle[21, 22] showed that the overall sound pressure level can be closely correlated using optical techniques (C_2 radical emissions) and ion density probes, while Fox & Bertrand[23] used saturation current measurements to demonstrate the same. However all these studies used their measurements to correlate overall sound pressure level. Moreover, the source evaluation techniques were either single spatial point measurement or an overall emission measurement. While they were excellent techniques to evaluate the overall sound pressure, the evaluation of the spectrum of combustion noise would require a better understanding of the spatial coherence in heat release fluctuations. Wäsle *et al*[24] used

high speed LIF images to understand the spatial correlation of heat release fluctuation in jet and swirl flames. They found regions of negative correlation between different locations of their flames. Although spatial correlations provide a significant improvement in our understanding, spatial coherence and cross spectrum of heat release oscillation is critical in our understanding of the scaling of the spectrum of combustion noise.

Experimental Data

There is a significant amount of data that is available for combustion noise measured for both open turbulent flames (premixed and non-premixed) and for gas turbines (commonly referred as core noise). While the data measured for gas turbines[25, 26, 27, 28] is more practical flow conditions, its interpretation is complicated by the presence of other noise sources like jet noise in the exhaust, turbine and compressor noise. Furthermore the combustor itself produces significant entropy noise (noise produced by the acceleration of hot gas pockets through the nozzle) and other hydrodynamic fluctuations.[29] While there have been several attempts to separate these noise sources using coherence techniques,[30, 31, 32, 33] they all inherently assume the flame to be a compact source at all frequencies which is yet to be established even in open flames. Turbulent non-premixed flames have to account for the mixing which also complicates the problem. Hence the data that will be discussed next will be primarily restricted to open, turbulent, premixed flame noise data, while a few other cases are considered when pertinent.

Overall Sound Pressure Level

Most of the available data consist of correlations between the overall sound pressure level and the geometry or operating flow conditions. For example, the data in

Putnam[34] and Kilham & Kirmani[35] illustrate the combustion noise characteristics of various burners as a function of heat input, equivalence ratio and upstream turbulence levels. In general, these studies found that the total sound emissions from the flame scaled with its overall heat release rate. At a fixed heat release rate, the dependence of its acoustic emissions upon air velocity, equivalence ratio, burner diameter, and burner shape was more complex as the effects of these parameters, often coupled, could also depend on the turbulence characteristics of the incoming flow.

A significant number of experiments have been conducted for characterizing the overall noise produced by flames under various flow conditions. As a result, a large empirical database exists in the literature of measurements of overall sound power level as a function of burner geometry, flow rate, and reactant kinetic characteristics (e.g., equivalence ratio or fuel type).[15, 34, 36, 37] Key results are summarized in reviews by Mahan[38] and Dowling.[10] However these empirical correlations are less useful for conditions outside their data range.

For example, Strahle[15] analyzed the scaling of combustion noise which, combined with empirically derived expressions for parameters like turbulence intensity and correlation lengths, led to the following correlation:

$$P \propto F^{-0.42} S_L^{2.16} U_{ave}^{1.82} D^{3.44} \quad (7)$$

Through a direct regression analysis of their data, using similar parameters, they arrived at similar correlation values:

$$P \propto F^{-0.4} S_L^{1.83} U_{ave}^{2.67} D^{2.78} \quad (8)$$

Although this correlation was obtained for a fairly wide range of conditions in terms of velocity, flame speeds (not as significantly wide as others), and burner

diameters, this experiment was conducted in an experimental set-up where there were no external turbulence generators. Hence these correlations are derived for data where the mean and the turbulent flow properties could not be independently varied. This is a significant issue as it is known, see Kilham & Kirmani,[35] that turbulence characteristics have a significant role in overall noise produced by the flame. While Kilham & Kirmani[35] showed the role of turbulence, they did not incorporate its role in their correlation resulting in a function with coefficients similar to that of Strahle:

$$P \propto F^{-0.28} S_L^{1.83} U_{ave}^{2.67} D^{2.81} \quad (9)$$

Although they showed through their data that turbulence plays a very significant role in combustion noise, they correlated only the OASPL to only the mean flow parameters. They concluded that the correlation with mean flow parameters adequately captures the trend, although the role played by turbulence is undeniable.

The most significant issue with the available correlations is that they are largely empirical and not based firmly upon an underlying model. Thus they tend to have little predictive ability for conditions outside the dataset they are derived from. For example, the correlation developed by Strahle in Equation 8 was based on a combustor that did not have any provision to vary the turbulence intensity independent of the mean velocity. Hence their correlation cannot be used to predict noise output for combustors that have provisions to change the turbulence intensity independent of the mean flow. Hence in spite of large database being already available, there is still a significant void in the total noise prediction capabilities.

Spectral Characteristics

Although the total sound power of turbulent flames has been extensively cataloged, their spectral characteristics have been given significantly less attention. The limited experimental data show that combustion noise is broadband in nature; Typical spectra of combustion noise emissions can exceed background noise levels for frequencies from ~100 Hz to over 20 kHz.[39, 40] The broadband spectrum of combustion noise typically increases with frequency until it reaches a maximum and then rolls off into the background level (see Figure 2). Experiments show that flame noise levels peak in the low frequency range of 200-1000 Hz.[38, 41] Other data also indicate the presence of multiple peaks in the acoustic spectrum.[42] However these multiple peaks may be due to room reflection effects.

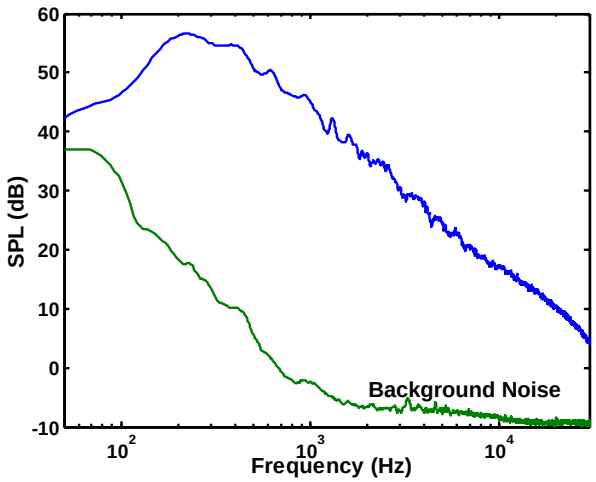

Figure 2 Combustion noise spectrum for the case of D = 10.9mm, U_{ave} = 21.8m/s, turbulence intensity = 1.5%, Fuel = Natural Gas, and ϕ = 0.95

Studies have shown that the acoustic spectrum varies with flow conditions and burner configurations. Petela & Petela[43] observed that the scaling of the sound pressure level with the overall heat release rate was not localized in frequency space, i.e. the change in the sound pressure level occurred over a broad range of frequencies, all the

way up to 25 kHz. Kotake & Takamoto[41, 44] studying the effect of burner diameter and shape, flow velocity, and turbulence intensity on the combustion noise spectrum up to about 1 kHz in frequency, found the following: increases in diameter, velocity or the turbulence level caused a corresponding increase in overall sound pressure level of the flame; that, for a given velocity and equivalence ratio, increases in diameter led to increases in combustion noise power over the entire range of frequencies, with a slight downward shift of the frequency of peak emissions; that the shape of the burner affects the overall sound power as well as the frequency of peak emissions; and that, the overall sound power of rectangular burners was higher than square or circular burners, which they attributed to its larger perimeter relative to its area. The same trend was also found in the high frequency component of the spectrum.

The frequency of peak amplitude emissions has been discussed extensively in the literature. However this has not resulted in any conclusive determination of its controlling parameters. A number of analyses have assumed a Strouhal number scaling, based on burner diameter and jet exit velocity, similar to the jet noise spectral scaling, for F_{peak}.[15, 45] Such a scaling assumes that the combustion noise scales similarly to flow noise. However, the physics behind noise production in a turbulent flame involves other non fluid mechanic factors, such as chemistry. Shortcomings of this type of Strouhal number scaling are highlighted in several other studies.[41, 46, 47] There has also been suggestions of a Strouhal number scaling based on the integral length scale and intensity of velocity fluctuations in the underlying turbulence.[15, 48] However this scaling also has the same shortcoming as the previous, as it does not capture the known dependencies of F_{peak} upon chemical kinetics.

Other workers have suggested that the peak frequency is controlled by the underlying kinetic rates, not fluid mechanics.[47, 49, 50] For example, Abugov & Obrezkov[50] suggested that the characteristic scales for the Strouhal number scaling were the diameter of the burner and the laminar flame speed. However the problem with this approach is that it completely neglects the known influence of fluid mechanics upon peak frequency. For example, Smith & Kilham[45] showed that the peak frequency increased with flow velocity while the chemical parameters were held constant. Shivashankara *el al*[47] published the following empirical result for the peak frequency:

$$F_{peak} = 12.57 U_{ave}^{0.18} D^{-0.08} S_L^{0.52} F^{-0.69} \quad (10)$$

As can be seen, this correlation incorporates fluid mechanics (U_{ave}), geometry (D) and chemical kinetics (S_L and F) influences upon F_{peak}. Thus we can see that there has been no consensus on the scaling of the peak frequency.

Another parameter that has been characterized in the spectrum of combustion noise is the slope of the roll off at the high frequency side of the spectrum. Several studies have also measured the existence of a spectral region, beyond the peak frequency, with a power law dependence upon frequency. Abugov and Obrezkov[50] found that the spectrum exhibits a power law dependence with an exponent of –5/2 over the 2 kHz to 10 kHz frequency range. This power law behavior, with a similar exponent, was also measured by Belliard.[51] Clavin & Siggia[16] predicted a similar value of -5/2; they assumed the flame to be compact, and that the roll off is purely due to the roll off in the turbulence in the intermediate scales. However it is yet to be shown that the combustion is a compact noise source even at those high frequencies.

Directionality of Combustion Noise

Studies have shown that there is a marginal directionality in the noise radiated from an open turbulent flame. Smith[52] measured directional characteristics of the overall sound pressure level of combustion noise. He found that the noise level was fairly omnidirectional at low Reynolds number. However at higher flow rates the angle of maximum noise radiation moved towards the axis of the burner. He attributed some of this effect on the location of maximum noise radiation being near the flame tip while the angles were measured from the exit of the burner. Overall, at low Reynolds numbers (<10,000) the difference in overall sound pressure level between various angles was ~3dB with the angle of maximum radiation being ~80° from burner axis, while at a higher Reynolds number of 25,000 the difference rose to ~5 dB with the angle of maximum radiation being 40°.

Shivashankara[53] measured the directionality of the different spectral components of the acoustic signal for various fuels and burner diameters. He found that the difference between the maximum and minimum overall sound pressure levels was about 4dB. However, significantly more directionality was observed in the spectral components with frequencies larger than the peak frequency (about 300 Hz). He found that the spectral decay after the peak was substantially faster at 15° (with respect to vertical axis starting from the exit of burner) than at 120°. This directional characteristic was attributed to the refraction of sound due to the temperature gradients present in a flame and its plume[12].

Concluding remarks

As discussed, studies have provided a significant body of experimental data that characterize the total sound power emitted by turbulent flames over a wide range of

parameters and configurations. Scaling these data with theoretical and semi-empirical correlations has achieved limited success. Data is available that presents the characteristics of the spectrum of acoustic emissions (although usually over limited frequency ranges, for frequencies of only 1 kHz or less). However, these data are limited and the manner in which the acoustic spectrum reflects fundamental flow and chemical kinetic processes is not understood. In addition, no systematic studies characterizing the manner in which flow characteristics, burner configuration, fuel kinetics, and fuel heat content affect the acoustic spectrum exist. Furthermore, even in the existing spectral studies there is little discussion about the accuracy of their spectral estimates. As discussed in Chapter 4, this issue requires great care because the acoustic power spectrum varies by several orders of magnitudes over the relevant spectral bands. If not properly accounted for, errors can render the spectral estimates of the lower amplitude, high frequency emissions meaningless.

CHAPTER 3

EXPERIMENTAL DESIGN AND INSTRUMENTATION

Combustor Design

This section describes the design of the combustor and flow preparation section. The study being an investigation of acoustic properties of open flames, it was critical to have a combustor design that not only produced an open turbulent flame, but also that has an upstream flow containing minimal noise from upstream sources. Any upstream noise produced by flow regulators, bends and so forth would also behave like a monopole source at the burner exit, similar to combustion noise. This would make it very difficult to separate this noise from combustion noise. Furthermore, it was desired to have a flow preparation section that would produce variable turbulence levels, with reasonably uniform mean and turbulent velocity profiles across its cross section. Figure 3 shows the schematic of the burner facility that was used in this dissertation.

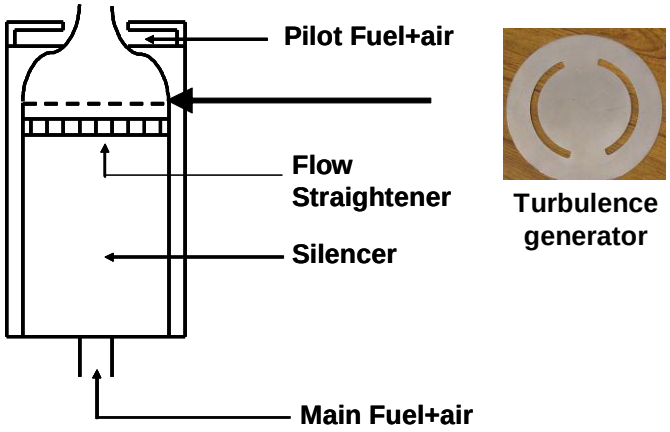

Figure 3 Schematic of the piloted burner with a picture of the turbulence generator

A converging section produces a uniform velocity profile at its exit. This design required an upstream quiescent flow. An industrial silencer was used to decelerate the flow, coming through the pipes, into a section of diameter 101.6 mm that is large

compared to both the diameter of the exit of the burner and the inlet flow pipes. This not only simulated the quiescent upstream conditions similar to that of the inlet of wind tunnels, but also suppressed any extraneous upstream noise present in the flow. Four different nozzles with diameters of 34.8, 17.3, 10.9, and 6.4 mm were used in this study. This enabled high contraction ratios of 8.5:1, 34.6:1, 86.5:1 and 256:1 respectively. High contraction ratios led to a uniform velocity profile with a very small boundary layer. The boundary layer thickness expectedly reduced with increasing contraction ratios. This led to the time averaged velocity at the center to be closer to the mean velocity (calculated from measured upstream flow rates) as the contraction ratios increased. The time averaged center velocity was found to be 20% more than the overall mean velocity in the case of the 34.8 mm burner compared to less than 3% that was measured in the case of the 6.4 mm burner. The exit velocities were significantly higher than the flame speeds of any fuel-air mixture used. Hence these flames required a separate stabilizing mechanism. Hence a small pilot flame ring was used to anchor the flame.

The presence of the silencer also produced a flow with low turbulence level, less than 1%. The turbulence characteristics of the exit flow in the burners were manipulated with an axisymmetric version of the device described by Videto and Santavicca[54]. These devices consist of 1.27 mm thick plates with semicircular slots cut out. The inner diameter (D_1) and outer diameter (D_2) of the slots were the characteristic dimensions of the turbulence generator; varying these values allows the turbulence level of each burner to be varied independent of flow velocity by altering the blockage area of the upstream flow. In this way, turbulence intensities ranging from 8 - 13% for the 34.8 mm burner, 2 -

13% for the 17.3 mm, 1 - 7% for the 10.9 mm and 0.6 - 2.4% for the 6.4 mm burners were obtained. The dimensions of the turbulence generators are given below:

Burner Diameter (mm)	Serial No.	D_1 (mm)	D_2 (mm)	Number of Slots	Angle of Slots (°)	Blockage (%)	Turbulence Intensity Range (%)
34.8	3481	63.5	88.9	2	160	66.7	8.25 - 8.84
34.8	3482	50.8	88.9	2	160	54.2	7.98 - 9.43
34.8	3483	50.8	76.2	2	160	72.2	12.41 - 12.82
17.3	1731	50.8	76.2	2	160	72.2	2.27 - 2.43
17.3	1732	69.9	76.2	2	160	92.0	2.87 - 3.25
17.3	1733	96.5	101.6	2	160	91.3	9.23 - 12.59
17.3	1734	71.1	76.2	2	160	93.6	4.09 - 5.64
10.9	1091	71.1	76.2	2	160	93.6	1.27 - 1.46
10.9	1092	63.5	68.6	2	160	94.2	2.23 - 2.42
10.9	1093	73.7	76.2	4	70	98.6	2.70 - 3.26
10.9	1094	73.0	76.2	2	70	99.1	6.23 - 6.93
6.4	0641	60.3	63.5	2	160	96.6	0.77 - 0.80
6.4	0642	47.6	50.8	2	160	97.3	0.64 - 0.84
6.4	0643	60.3	63.5	8	35	97.0	0.73 - 0.80
6.4	0644	47.6	50.8	2	70	99.4	2.30 - 2.40

Table 1 Dimensions of the turbulence generators used in this study

The exit velocities were maintained such that the minimum Re_D ($=U_{ave}D/\nu$) was at least 10,000. The high velocities sometimes resulted in localized extinction of the flame, mainly in the tip. These permanent holes in the mean flame structure would result in a significant portion of the fuel escaping and not burning. These flames had significantly different acoustic properties. Hence only the conditions that produced statistically stable flames with a combustion zone, with no local extinctions were studied.

Anechoic Facility

The acoustic data were measured in an anechoic chamber. The external and the internal dimensions (measured from tips of wedges) of the anechoic chamber are 4.11(L) x 3.22(W) x 3.58(H) m and 2.92(L) x 2.20(W) x 2.54(H) m respectively, see Figure 4.

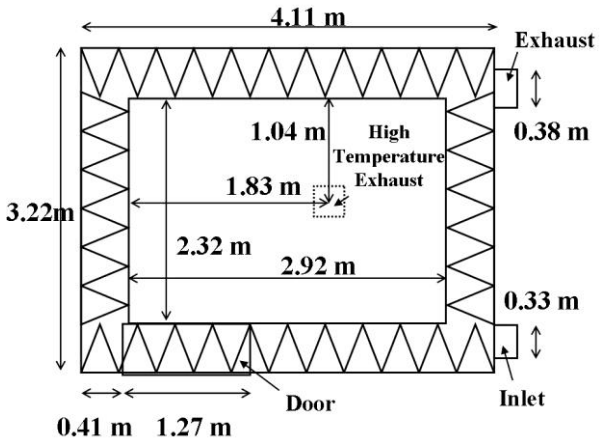

Figure 4 Georgia Tech Combustion Lab Anechoic Chamber, plan view

The chamber walls are fitted with 45.7 cm foam, see Figure 5. All the wedges on the floor are removable in order to make it easier to arrange test equipments. Air is re-circulated through the chamber by baffled exhaust and inlet ducts. This environment essentially eliminates the acoustic feedback provided in a reverberant acoustic field.

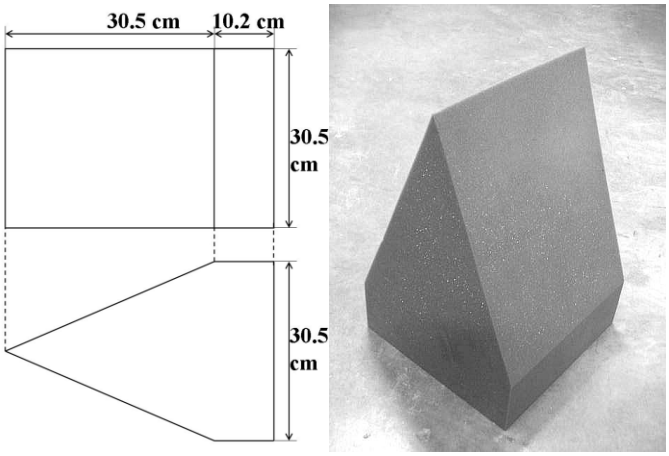

Figure 5 Sketch and photograph of acoustic foam wedge (Polyurethane) used in the anechoic chamber

A high temperature exhaust is situated on the ceiling and guides the heat generated by a combustor beneath it, see Figure 6.

Figure 6 Photograph of the anechoic chamber interior looking toward the high temperature exhaust

The quality of the anechoic chamber was characterized with the use of a "point source" and the deviation from its $1/R^2$ law dependence in its far field.[55] Details are provided in the Appendix II. The results summarizing chamber performance are plotted in Figure 7. Absolute maximum deviation from the inverse square law was found to settle within 1dB above 400Hz and to be attenuated down to 0.5 dB above 1250Hz. The characteristics below 200 Hz did not have a good $1/R^2$ dependence suggesting that either/both the spectra measured at those frequencies were taken in the near field of the source and/or there are severe room reflections.

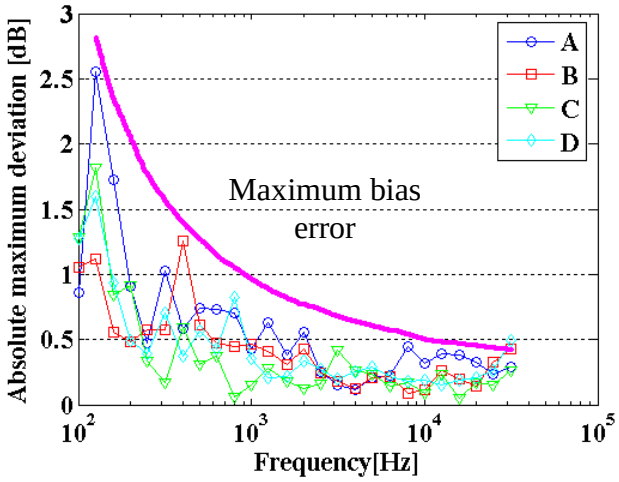

Figure 7 Frequency versus absolute maximum deviation from inverse square law

Instrumentation

1. Acoustic Measurement

The acoustic data were obtained with 3 Brüel & Kjær microphones (two 4939 and one 4191 type) that were placed at a distance of 1.02 m from the burner at angles of 45º, 65º, and 90º from the vertical axis of the burner. The raw microphone signals were fed into Krohn-Hite Butterworth type band pass filters. The output analog stream was then acquired as digitized data with a 12-bit National Instruments data acquisition board (PCI-MIO-16E-1). The voltage limits of acquisition and microphone output gain were both adjusted so as to keep any digitization issues to a bare minimum (<0.25%). The acoustic data were obtained at a data rate of 80 kHz. The data were fed through 4^{th} order Butterworth high and low pass digital filters set at lower and upper frequencies of 50 Hz and 35 kHz, respectively.

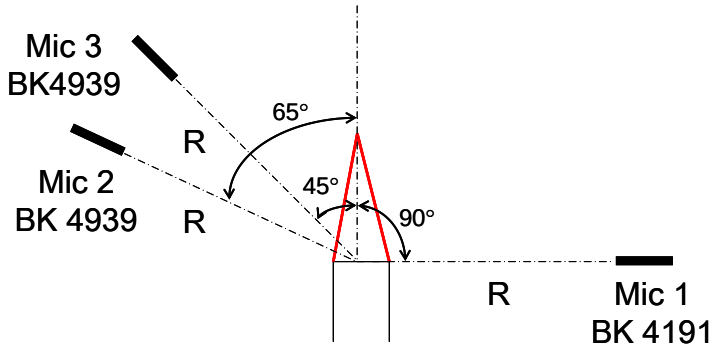

Figure 8 Location of microphones with respect to the burner

2. Turbulence Measurement

The upstream turbulence intensities were measured using a DANTEC dynamics' Constant Temperature hotwire Anemometer (CTA). The exit velocity profile was measured using a generic miniature straight probe, with a wire diameter of 5μm, held using a straight probe holder. The hotwire probe was guided across the burner diameter with the use of a mechanical traverse.

However in the case of the smallest burner (D = 6.4 mm), the hotwire length (length =1.25 mm) was comparable to the radius of the burner. This made it very difficult to ensure the complete exposure of the wire to the flow while traversing the wire across the burner. Furthermore the uncertainty, in locating the center of the burner at the beginning of the experiment was of the order of ±0.5 mm. Due to these difficulties, the exit profile was not measured for this burner diameter.

The center velocity alone was measured using a 90° probe holder. The raw turbulence data were also obtained at 80 kHz (similar to the acoustic data). This data was filtered at 30 kHz. This was due to the fact that the filter settings in the hotwire system had only a limited number of options for the low pass frequency settings.

3. Flame Imaging

Since understanding the flame dynamics was an integral part of this dissertation, high speed video images were taken. This was done using a Phantom High Speed Video Camera. The camera was sensitive to light in both the visible spectrum and the infrared wavelengths. The infrared emission in the post flame zone was quite significant compared to the flame zone radical emissions and thus would affect any calculation from these images. In order to mitigate this problem, a Schott BG-38 filter (transmits more than 90% between 360 nm and 575 nm) was used to cut off emissions in infra-red wavelengths and transmit only the visible light. This would include radiation from almost all the major radicals, i.e. CH* (390 and 430 nm), C_2* (510 nm), CO_2* (a very low continuous background signal from 300 nm - 600 nm), except OH (310 nm). The filter primarily cutout black body radiation and signals from H_2O bands over 600 nm. The

presence of radicals is a good indicator of the flame zone (spatial error ~ $O(\delta_{flame})$) and hence can be considered as a good indicator of the local heat release.

The chemiluminescence data were obtained at various frame rates depending on their purpose. In order to obtain mean and variance image of the flame for each of the flow conditions, 1000 chemiluminescence images were obtained at a frame rate of 1000Hz for each of the flow conditions. This set of data was very useful in obtaining rational correlation of acoustic parameters. In order to understand the temporal flame dynamics in detail, two flow conditions were imaged at much higher frame rate.

Case1: D = 10.9 mm, Fuel = Natural gas, U_{ave} = 21.8 m/s, ϕ = 0.95, turbulence intensity = 1.5%, Frame rate = 2700 Hz, Number of frames = 4 sets of 8192 frames each.

Case 2: D = 34.8 mm, Fuel = Acetylene, U_{ave} = 9.7 m/s, ϕ = 0.63 and turbulence intensity = 8.5%, Frame rate = 2000 Hz, Number of frames = 6 sets of 1023 frames each.

CHAPTER 4

DATA REDUCTION

This section describes in detail how various parameters were estimated from the raw data that were acquired. This would help us understand the challenges and limitations in estimation of some of the parameters that help us understand combustion noise.

Estimation of the Acoustic Spectrum

Each acoustic data set contained 1,048,576 ($=10^{20}$) sample points per channel. They were obtained at a sampling frequency of 80 kHz. The data for each channel was then divided into 64 ensembles of continuous data containing 16,384 points per ensemble. The power spectrum of each ensemble was calculated using a standard fast fourier transform (FFT) algorithm and then averaged across the 64 ensembles. Since the data that were obtained were broadband in nature, further smoothening was possible by averaging the spectra across neighboring points in the frequency domain. This smoothening was done over a 15-point width (7 points on either side) across the individual frequency points. This enabled easier identification of parameters, such as peak frequency and low and high frequency spectral slopes. Thus, all SPL estimates of the acoustic signature from turbulent flames have a 4.88 Hz resolution. The spectral data were then converted to dB (ref. 20 μPa) after correcting for all the gain factors used during data acquisition. The uncertainty associated with random error of the resulting measurement was found to be ±1.3 dB at 95% probability (see Appendix I). It has to be noted that this doesn't account for the uncertainty in the flow conditions and hence the overall uncertainty can be expected to be higher than 1.3dB.

However, there were other bias errors that need to be quantified and minimized. Spectral leakage was of particular concern due to the wide range in magnitude of acoustic power (about five orders of magnitude) over the measured frequency range. A Hann window minimized leakage in all spectral calculations. The use of the Hann window increases the side lobe roll-off rate due to leakage from 6dB/Octave for a rectangular window to 18dB/Octave. In order to overcome the reduction in amplitude of the spectrum due to the use of the Hann window, the spectrum was multiplied with the ratio of the actual power of the spectrum (variance of the time series data) to the total power in the windowed spectrum.

The spectral data were then corrected for the microphones' frequency response (based on the data provided by Brüel & Kjær) and acoustic absorption due to humidity in atmosphere. Ahuja[55] suggested that the correction factor should be applied after calculating the spectrum at a Δf of 1Hz. Since the Δf is fairly low (4.88 Hz), the correction factors were applied directly to the spectrum. The difference in the final spectra calculated using the two procedures were quite minimal ($<10^{-3}$ dB).

Another source of bias error is the presence of reflections at low frequencies due to the presence of the chamber walls. While this error was measured, there was very little that could be done to actually minimize this issue. Hence care was taken to guard ourselves from making any erroneous interpretation of the data at the low frequency end. The dependence of this bias error upon frequency is shown in Figure 7, while the methodology for estimating the error is described Appendix II.

Figure 9 compares the raw spectrum of a single ensemble and the resulting ensemble averaged, corrected spectrum.

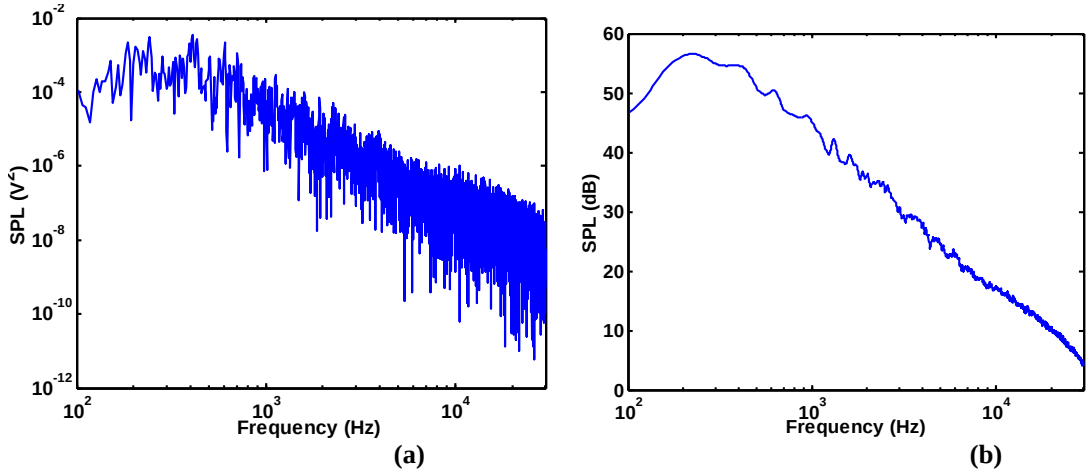

Figure 9 a. Raw spectrum of a single ensemble b. spectrum after averaging and application of correction factors for the case of D = 10.9mm, U_{ave} = 21.8m/s, turbulence intensity = 1.5%, Fuel = Natural Gas, and ϕ = 0.95

Characteristic Parameters in Spectrum

Since the typical spectrum (shown in Figure 2) has a very simple overall shape, it was parameterized in this study with four quantities. These are frequency of maximum noise radiation (F_{peak}), Overall Sound Pressure Level (OASPL), and spectral rise and decay rates on the high and low frequency sides.

However, the actual measurement of each of these parameters from the spectrum provided its own unique set of challenges. The challenges and the method of measurement to overcome these challenges for each of these parameters are discussed below.

1. Peak Frequency

The bias error due to acoustic reflection with in the anechoic chamber causes undulations in the low frequency side of the spectrum. This posed a problem in the measurement of the peak frequency, particularly in the cases where it fell below 200 Hz. If the peak frequency is simply defined as the frequency at which the calculated spectrum is at its highest, then this value would be biased by the local crests and troughs of the

undulation in the spectrum. This problem was overcome with the use of a fourth order polynomial curve-fit of the spectrum. The peak frequency was defined as the point where the fit was at its highest. Care was taken to ensure that this fit was robust to variation in frequency range over which it was calculated. This enabled a better estimate of the peak frequency. Figure 10 illustrates the curve-fit used in one such case.

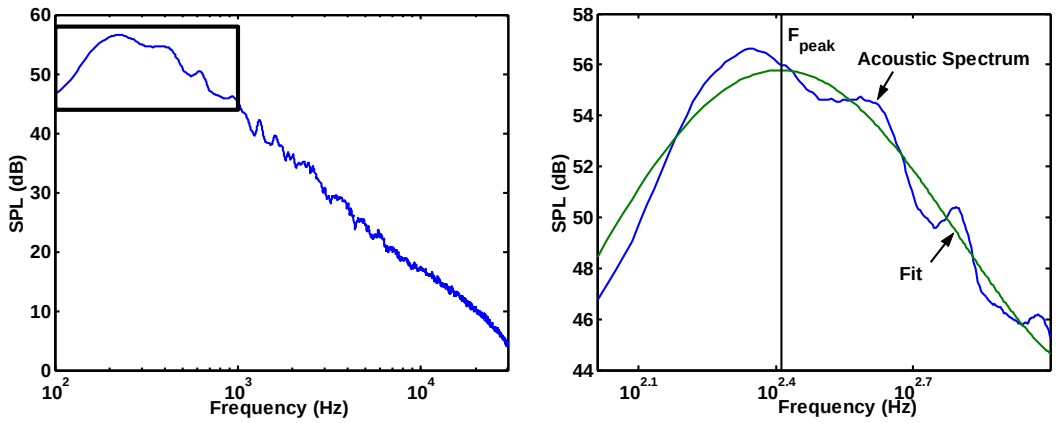

Figure 10 Measurement of Peak Frequency for the case of D = 10.9mm, U_{ave} = 21.8m/s, turbulence intensity = 1.5%, Fuel = Natural Gas, and ϕ = 0.95

2. OASPL

The OASPL was calculated as a summation of the SPL values in the corrected spectrum. This was done to account for the frequency dependent corrections applied to the raw data in the frequency space.

3. Slope of high frequency side (α)

The combustion noise spectrum exhibits a nearly power law spectral decay for f> $2F_{peak}$ (see Figure 11) up to frequencies of about 10-15 kHz. The spectral decay rate was characterized by fitting a linear curve to the log plot of the spectrum at the high frequency end to determine the parameter (α) in the expression $P(f) \propto f^{-\alpha}$. However, the choice of the frequency range over which this was calculated is important. The power law behavior was measured for frequencies over 2.5 times the peak frequency up to ~10 kHz. This

ensured that the frequency range over which the power law behavior was estimated was made to be sufficiently large while ensuring that they do not include the non-linear sections of the spectrum.

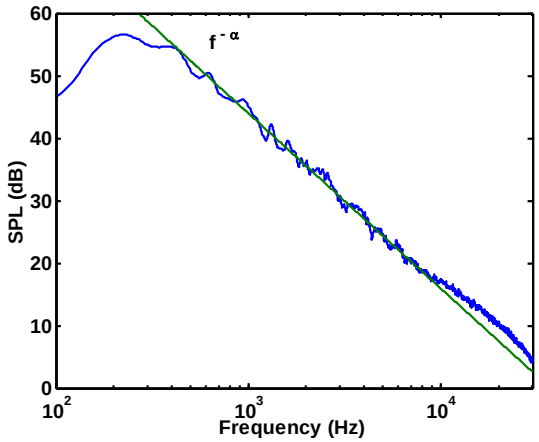

Figure 11 Measurement of the spectral decay coefficient in the high frequency side-band for the case of D = 10.9mm, U_{ave} = 21.8m/s, turbulence intensity = 1.5%, Fuel = Natural Gas, and ϕ = 0.95

4. Slope on low frequency side (β)

The combustion noise spectra also seem to exhibit power law behavior at the low frequency sideband of the spectrum ($P(f) \propto f^{\beta}$). The measurement of this parameter posed the most significant challenge. The undulations in the spectra, due to reflection in the anechoic chamber, increased with decreasing frequency. The cut-off point for any measurement made in this anechoic chamber was set at 100 Hz, although the frequency at which the room begins to conform to ISO3745[56] was actually higher. This was done to accommodate measurement of combustion noise for large burners in this study. Furthermore, the background noise level in the anechoic chamber increased with decreasing frequency, eventually dominating the noise measurement at low frequencies (usually less than 100Hz). Thus, an accurate measurement of any parameter that is based on the spectral data at the low frequency regime posed the most challenge.

Obtaining an accurate linear curve-fit it required a sufficient number of points. The maximum frequency used in the curve-fit had to be sufficiently farther away from the peak frequency because of the non-linear behavior of the spectrum near the peak frequency while the minimum frequency value that was used in the calculation had to have lower level of reflection issues while still maintaining a high signal to noise ratio. Hence this parameter was measured only for cases where the peak frequency was higher than 600 Hz, so as to have enough number of points to make a reasonable estimate of this parameter. Figure 12 shows the linear curve-fit done for a typical combustion noise spectrum.

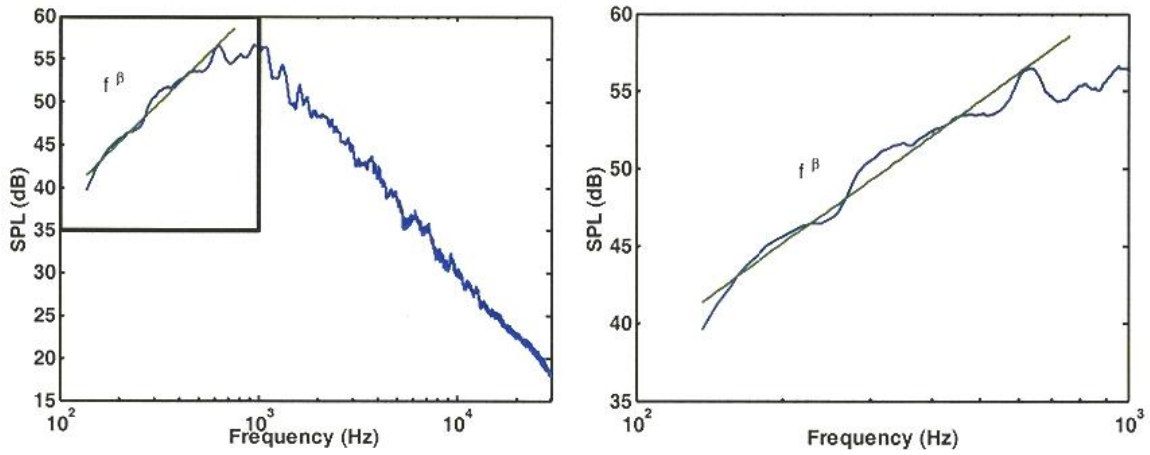

Figure 12 Curve-fit on the low frequency side for the estimation of β for the case of D = 6.4mm, U_{ave} = 40m/s, turbulence intensity = 0.8%, Fuel = Acetylene, and ϕ = 0.71

Estimation of Acoustic Cross Spectrum and Coherence

The cross spectrum and coherence were calculated using standard FFT based methods. However this methodology can introduce bias error when time lag between the various measurement locations is comparable to the time period of individual ensembles[57]. Hence care had to be taken that any time lag between the microphones that could occur in the regimes of high coherence had to be very small when compared to the

time period per ensemble of calculation. The data were divided into sets of 16,384 points (same as the auto spectrum calculations); each ensemble had 50% overlap with the next ensemble. Thus these calculations were done with 127 equally spaced ensembles.

Characteristic Parameters in Cross Spectrum and Coherence

The parameters that were obtained from the coherence and cross spectrum were:

1. Limit of high Coherence – f_{cutoff}
2. Phase of Cross Spectrum

1. Limits of high Coherence

A typical coherence calculated between the data collected with two different microphones is shown in Figure 13. The coherence value is fairly high at low frequencies, then dips, and then rises again before falling to nearly zero at high frequencies. This behavior can be characterized with the use of cutoff frequencies. Figure 13 and Figure 14 shows two cut-off frequency points. The cut-off values for coherence level were kept quite low so that it will be insensitive to local undulations in coherence function. The cut-off frequency (f_{cutoff}) defined in Figure 13 is defined as the point where the coherence dips below 0.75 of the maximum value of coherence for that particular case. This cut-off is used to primarily characterize the acoustic compactness of the flame zone. Other cutoff values (other than 0.75) were also evaluated and it led to similar conclusions obtained from this cutoff criterion.

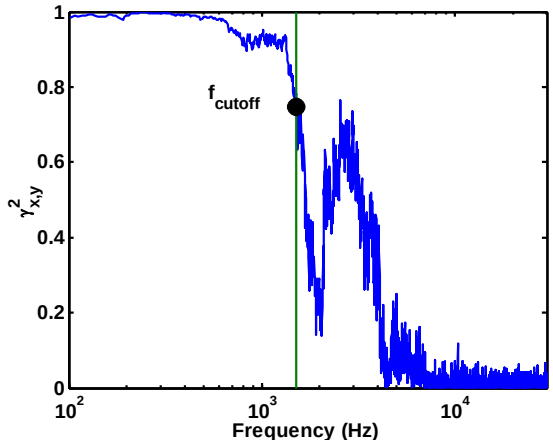

Figure 13 Graph illustrating typical dependence of coherence upon frequency showing procedure for the estimation of cutoff frequency for the case of D = 10.9mm, U_{ave} = 21.8m/s, turbulence intensity = 1.5%, Fuel = Natural Gas, and ϕ = 0.95

2. Time lag based on phase relationships

If two measurements of the same source have a constant time lag between them, then the phase difference between the two (i.e. the phase of the cross spectrum) will vary linearly with frequency. Furthermore the slope of the linear variation of phase with frequency is given by:

$$\frac{\partial \phi_{x,y}}{\partial f} = 2\pi\tau_{lag} \quad (11)$$

where τ_{lag} is the time lag between the two measurements.

The time lag can be calculated using a linear fit between the phase of the cross spectrum and frequency. However, the value of coherence at a particular frequency has a direct effect on the accuracy of the phase that can be calculated from cross spectrum at that frequency. Hence the frequency regime over which this time lag is calculated has to have a very high coherence value. This offers the upper bound for the frequency up to which the cross spectrum can be used for this time lag calculation. Furthermore even small reflections within the anechoic chamber could affect the accuracy of this

calculation. Since the room reflections increase with decreasing frequency, this offers a lower bound for the frequency regime of interest.

The upper cut-off frequency shown in Figure 14 was set as the point where the coherence dropped below 0.95 times the maximum value. The lower cut-off frequency was set at a point where it drops below 0.95 times the maximum value of coherence, unless that point is below 200 Hz. In that case the, cut-off value was set at 0.97 times the maximum value.

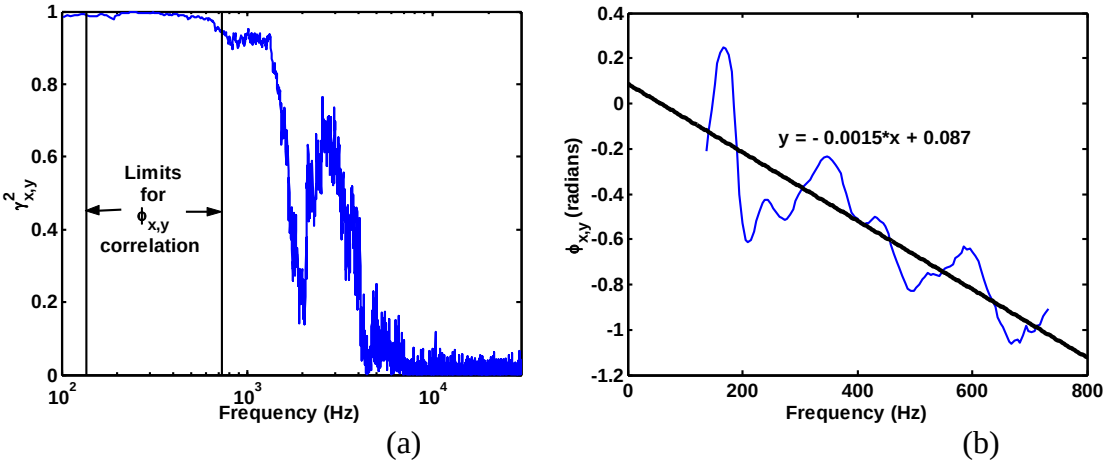

(a) (b)

Figure 14 a. Frequency range used for the cross spectrum analysis b. Phase difference vs. frequency for the case of D = 10.9mm, U_{ave} = 21.8m/s, turbulence intensity = 1.5%, Fuel = Natural Gas, and ϕ = 0.95

Estimation of upstream velocity characteristics

The velocity profiles at the exit of the burners were measured using a hotwire anemometer that was traversed across the diameter of the burner using a mechanical traverse. A set of 65,536 points, sampled at 80 kHz, were measured at each location, burner diameter, and velocity conditions. These 65,536 points were used to calculate the mean and turbulence velocity profile for each of the flow condition.

The center velocity was also measured using the same hotwire probe, but with a 90° probe holder which reduces interference to the flow. In this case 1,048,576 sample

points (same as acoustic data) were measured at 80 kHz. This data was divided into 64 equally spaced ensembles. The FFT algorithm was applied to each of the ensembles. The spectrum calculated across each ensemble was then averaged across all the other ensembles.

CHAPTER 5

COLD FLOW CHARACTERISTICS

Velocity Characteristics

Since upstream turbulence can affect combustion noise, the knowledge of the flow field is very critical in this study. In order to maintain a turbulent flow, the Reynolds number of the flow (based on mean exit velocity and diameter of the burner) was kept above 10,000. Its maximum value was 30,000. The mean velocity and the rms velocity profile for the burners 34.8, 17.3 and 10.4 mm burners are shown in Figure 15, Figure 16, and Figure 17 respectively. As discussed in Chapter 3, the exit profile of 6.4 mm burner was not measured.

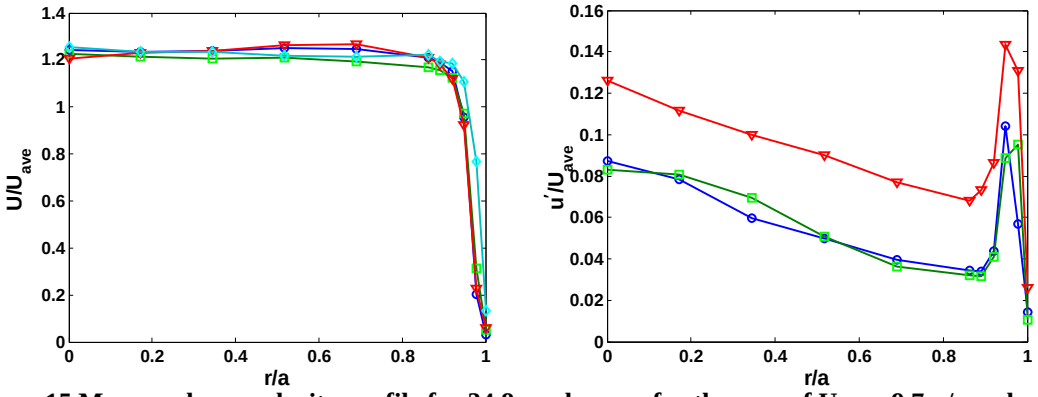

Figure 15 Mean and rms velocity profile for 34.8mm burner for the case of U_{ave} = 9.7m/s and turbulence generators o 3481 □ 3482 ▽ 3483

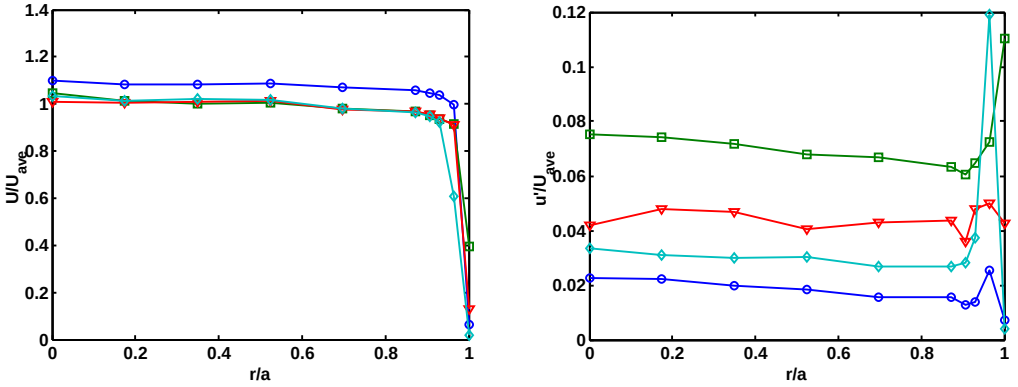

Figure 16 Mean and rms velocity profile for 17.3 mm burner for the case of U_{ave} = 26.1m/s and turbulence generators o 1731 ◊ 1732 □ 1733 ▽ 1734

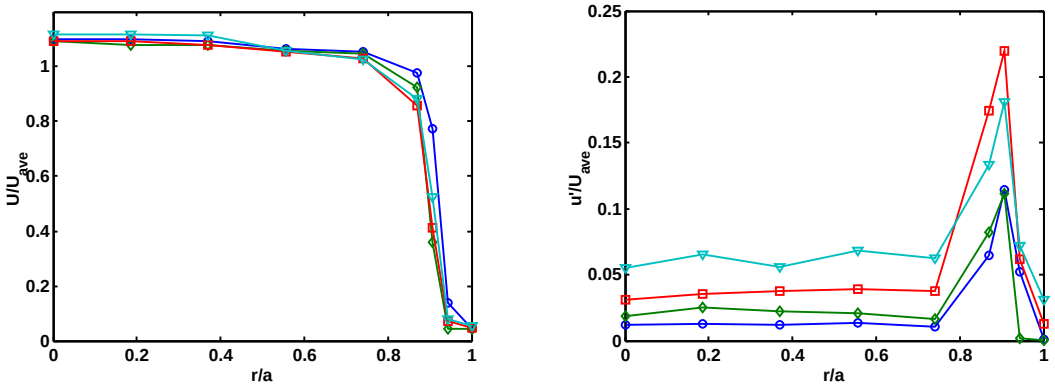

Figure 17 Mean and rms velocity profile for 10.9mm burner for the case of U_{ave} = 21.8m/s and turbulence generators o 1041 ◊ 1042 □ 1043 ▽ 1044

The time averaged velocity profile is fairly flat, with the center velocity being closer to the spatially averaged velocity as the contraction ratio increased. The turbulence profile is also fairly constant across the profile as the contraction ratio increased. Thus, we can see that the burner set-up achieved the desired velocity profile. Also, the center velocity measured is a good representative of the entire profile. These results further suggest that the mean and turbulence velocity profile was uniform, even for the 6.4 mm burner, due to higher contraction ratio, even though the profile was not characterized.

Figure 18 shows the spectra of the 1-D turbulent kinetic energy that was measured at the center for the four burners at various mean velocities. The spectrum of the 1-D turbulent kinetic energy decreases with increasing frequency. However during the measurement, the magnitude of the spectrum fell below the background noise level of the hotwire system. The background noise level of the hotwire would appear as a constant with frequency when the spectrum of the raw voltage alone is plotted. However, when a nonlinear transformation (between the measured voltage and velocity) is applied, then the

spectrum of the background noise level is appearing to increase with frequency. Hence the spectra at those frequencies have to be disregarded when the cold flow turbulence characteristics are characterized. Hence the frequency above which the spectrum is affected by the background noise level is marked by a black line.

However in the frequencies where an accurate measurement of the spectrum was possible, it is evident from these figures that the mean velocity plays a very important role on the frequency at which roll off occurs. In addition, none of the spectra have a distinctive inertial sub-range. However, it appears that the smaller diameter cases seem to have a slope closer to the $f^{-5/3}$ expected in the inertial sub-range. This is due to the fact that, as the diameter was decreased, the mean velocity was increased to maintain high Reynolds number.

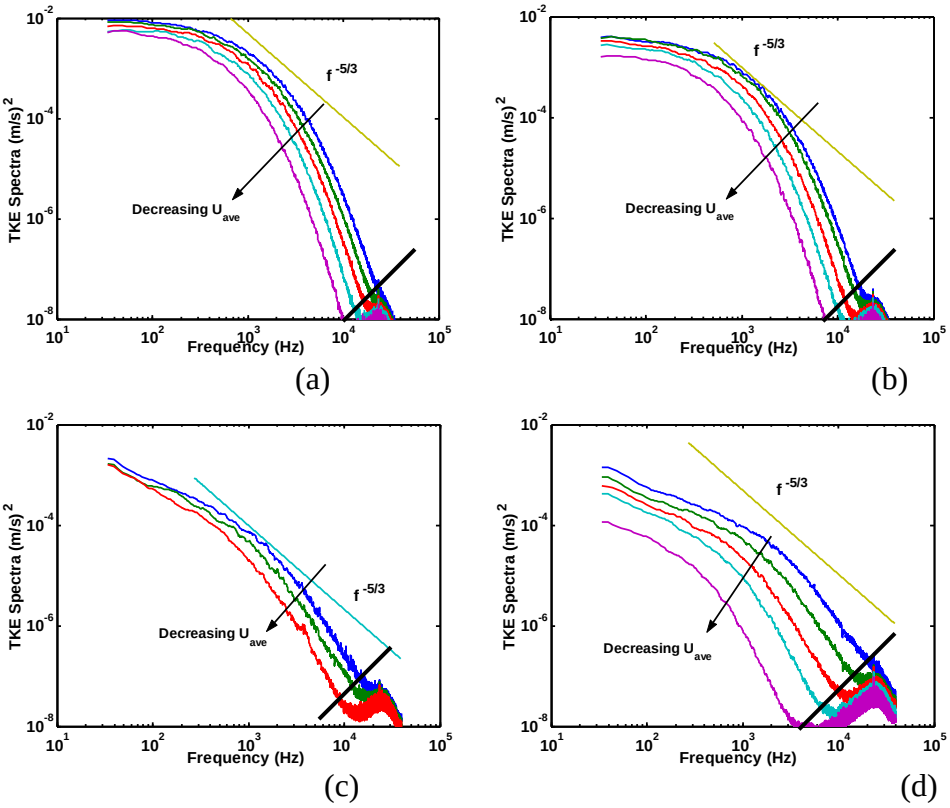

Figure 18 Spectra of 1-D Turbulent Kinetic Energy for the cases a. D = 34.8mm, Turbulence Generator = 3481 and U_{ave} =9.7, 8.6, 7.5, 6.4, 5.4 m/s b. D = 17.3mm, Turbulence Generator = 3481 and U_{ave} = 26.1, 21.8, 17.4, 13.1, 8.7 m/s c. D = 10.4mm, Turbulence Generator = 3481 and U_{ave} = 21.8,

19, 16.3 m/s and d. D = 6.4mm, Turbulence Generator = 3481 and U_{ave} = 56.3, 48.3, 40.2, 32.2, 24.1 m/s.

Acoustic Characteristics

The industrial silencer, in addition to being a settling chamber that makes the flow uniform, was also used to suppress any upstream noise. This is very important because any upstream noise generated by the upstream valves etc also behave like a monopole source which makes it very difficult to separate them from combustion noise. Hence the flow noise without the flame was also measured to understand the background noise in the system.

Figure 19 illustrates the background noise present in the system with and without the flow. It clearly shows that the cold jet noise makes very little noise compared to the exhaust fan system, which is clearly greater than the electronic noise in the measurement system up to 1 kHz. The flow with the pilot flame on makes higher noise than the flow with no pilot flame. However the overall back ground is still much lower than the combustion noise.

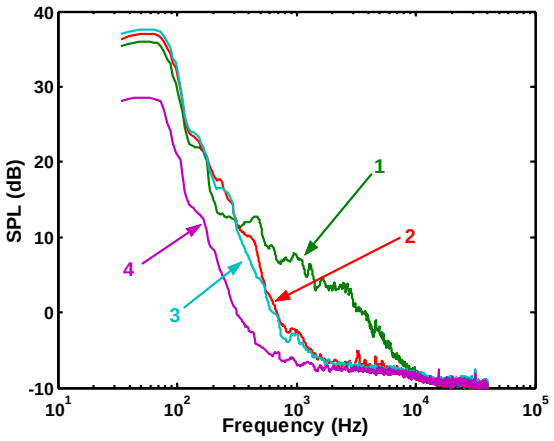

Figure 19 Illustration of the background noise in the system 1. D = 10.9 mm, U_{ave} = 21.8 m/s, pilot flame on & exhaust fan turned on, 2. D = 10.9 mm, U_{ave} = 21.8 m/s, pilot flame off & exhaust fan turned on, 3. No flow with the exhaust fan turned on and 4. No flow and exhaust fan turned off

Thus we can say that the current burner design achieved its stated goal of having a uniform mean velocity profile, with the turbulence being both spatially uniform and independent of the mean velocity, and the upstream flow carries very little noise.

CHAPTER 6

SOURCE CHARACTERIZATION AND TURBULENT FLAME DYNAMICS

Formulation of any rational correlation of combustion noise properties requires a thorough understanding the heat release dynamics responsible for the noise production. As discussed earlier, the intensity of chemiluminescence emitted by the flame is a measure of the heat release at that location. Hence an analysis of high speed video of chemiluminescence images of a turbulent flame provides insight into the dynamics of the flame that contributes to its noise production.

High speed images will be discussed in detail for two conditions. Then, another set of images recorded at lower frame rate (recorded at 1000 Hz) for the entire acoustic data set will be used to show correlation of the parameters derived out of the earlier discussion for the entire flow conditions.

The first set that will be discussed in detail is that of: Case 1 - D = 10.9 mm, Fuel = natural gas, U_{ave} = 21.8 m/s, ϕ = 0.95 and the turbulence intensity = 1.5%. At this condition four sets of 8192 images (totaling 32,768 frames), at a recording rate of 2700 Hz, were obtained for this analysis. Figure 20 shows the instantaneous image of the flame. The image, as expected, is axisymmetric owing to its turbulent nature.

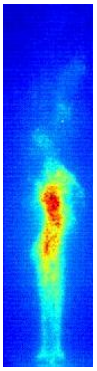

Figure 20 Instantaneous image of the flame

The mean and variance of every pixel in the high speed video for the above case is shown in Figure 21(a, c). Figure 21(b) is a plot of the intensity images (of a. mean and c. variance) integrated radially as a function of height. This provides insight into the location of maximum intensity and axial spread of intensity for both the mean and variance images.

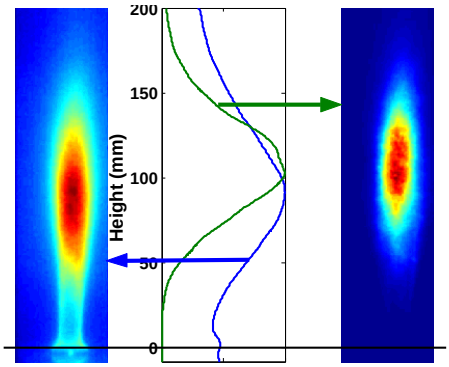

Figure 21 (a) Mean image, (c) Variance image, (b) Radially integrated intensity of a and c as a function of height

The mean image reveals that although the turbulent flame is asymmetric in its instantaneous realization, it is axisymmetric on average. A characteristic mean flame length can be calculated from these mean images.

A mean flame length is a very common parameter that is used to characterize a turbulent flame. However, the noise production at the combustion zone is due to unsteady

heat release. Hence it is important to look at the variance image as it represents the spatial distribution of the unsteady heat release (see Figure 21(b, c)). Comparing the mean and variance images, it can be seen that both show an axisymmetric behavior. However, the integrated intensity reaches a maximum farther down stream for the variance image than for the mean image. Thus the length scale parameter associated with the variance image is different from that of the mean image.

Based on the mean and variance image of the flame, three different length scales are defined. It will be shown in the later chapters which of them are significant, based on the parameter that is being scaled.

The first length scale definition is based on the mean image of the flame. Although this chapter mainly discusses the characteristics of unsteady part of flame heat, mean flame characteristics is one of the most commonly recorded parameters of an open flame. This flame length from the mean image, $L_{f,average}$ is defined as the distance from the burner exit to the axial location where the horizontally integrated intensity of the mean image reaches a maximum.

The second length scale definition is based on the variance image of the flame. This flame length from the variance image, $L_{f,variance}$ is defined as that distance from the burner exit where the horizontally integrated intensity of the variance image reaches a maximum. This length scale is analogous to the $L_{f,average}$ calculated from the mean image. This defines the center for the zone of activity that will be discussed in this chapter and its distance from the exit of the burner. The third flame length scale is also based on the variance image. This length scale, $L_{f,spread}$ is defined as that distance between the heights where the horizontally integrated intensity of the variance image crosses $1/4^{th}$ of the

maximum value. The three definitions are illustrated in Figure 22. Figure 23 compares the same length scales with their respective processed images.

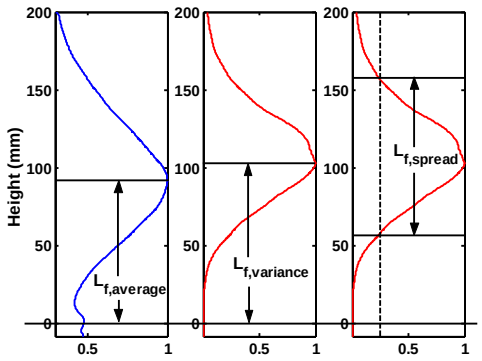

Figure 22 Radially integrated intensity vs. height in a. Mean image ($L_{f,average}$ definition), b. Variance image ($L_{f,variance}$ definition), c. Variance image ($L_{f,spread}$ definition)

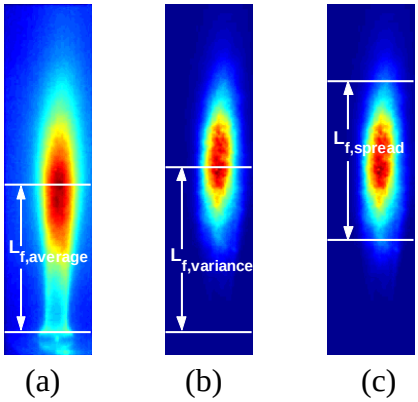

Figure 23 Illustration of the flame lengths derived from a. Mean image ($L_{f,average}$ definition), b. Variance image ($L_{f,variance}$ definition), c. Variance image ($L_{f,spread}$ definition)

Figure 24 compares, for all the cases using the lower speed chemiluminescence images, the three length scales defined. It can be seen that the parameters are correlated with each other but are not identical. This suggests that under certain circumstances the flame lengths can be used interchangeably. However we have to exhibit caution that while the trends may be similar in spite of such a substitution, they might not necessarily explain the physics satisfactorily. Moreover when different types of open flames are compared the relationship between these three length scales might not be the same.

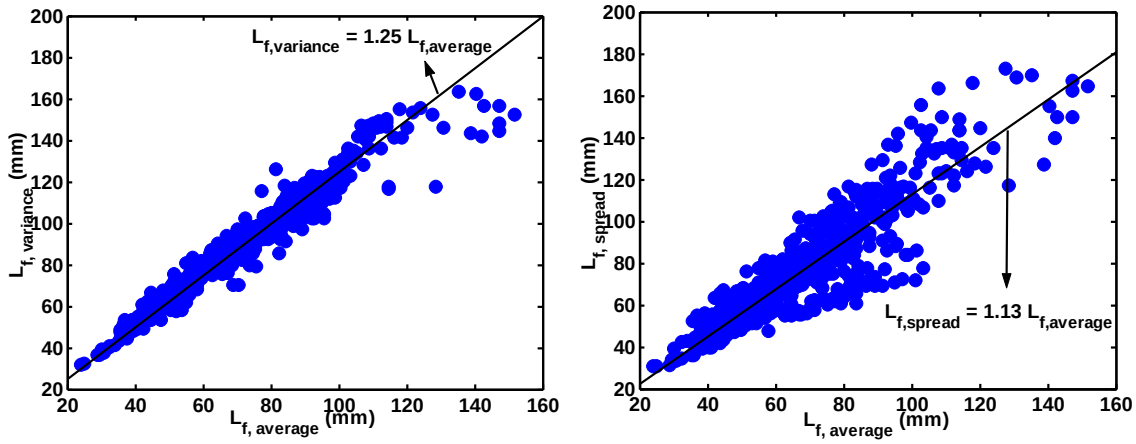

Figure 24 Comparison of $L_{f,average}$ with a. $L_{f,variance}$ b. $L_{f,spread}$

In order to further analyze the spatio-temporal variation of the heat release oscillation in the flame, the spectrum of intensity variation at each pixel of the domain was obtained for Case1. The 4 image sets (of 8192 frames each) were further divided in to ensembles of 1024 images that had 50% overlap to maximize the number of averages for the SPL calculation at each pixel. Hence the Δf for this set of data is 2.64 Hz. Then the pixel of maximum intensity was chosen at each frequency point and cross spectrum and coherence – for that frequency - were calculated for all other pixel locations with respect to the chosen pixel. This was done to better understand the special correlation of local heat release oscillations at each frequency. Figure 25 shows the spatial distribution of the heat release oscillation (normalized to the same maximum) at 4 different frequencies. The white horizontal lines in each of the images represent the height at which the (horizontally) integrated intensity drops below 25% of the maximum value.

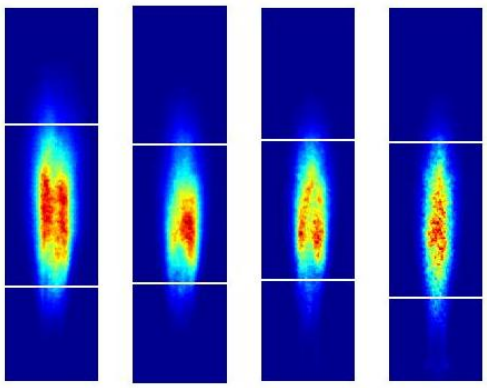

Figure 25 Spatial variation of intensity oscillation for Case1 at frequencies of (a) f = 100.2 Hz, (b) f = 200.4 Hz, (c) f = 400.8 Hz, and (d) f = 801.6 Hz

In order to compare the spatial distribution of chemiluminescence oscillations the radially integrated intensities for each of those frequencies are plotted against the height in Figure 26.

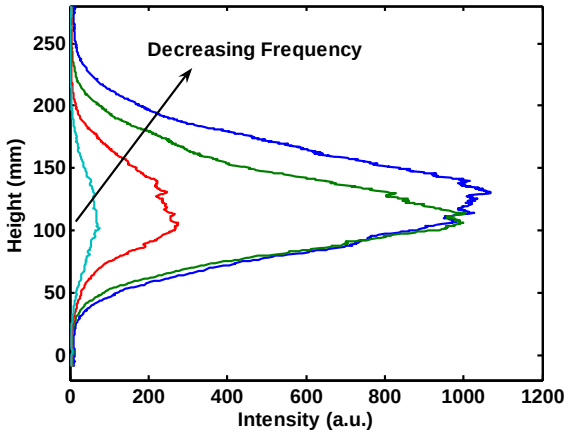

Figure 26 Radially integrated intensity for the images in Figure 25

While examining Figure 25 and Figure 26, the most important observation (across all these frequencies) is that the region of maximum heat release oscillation is away from the base of the flame and quite close to the tip of the flame. It can also be easily seen that the maximum intensity at 100.2 and 200.4 Hz frequency points are fairly similar while the number drops dramatically at 400.4 Hz and continues to drop at 801.6 Hz.

Another trend that needs to be noticed in Figure 25 is the variation of the cutoff lines (lower and upper) across the images. Figure 27 compares the two cutoff points

across all frequencies. The plot results show that the source region drops closer to the burner exit with increasing frequency.

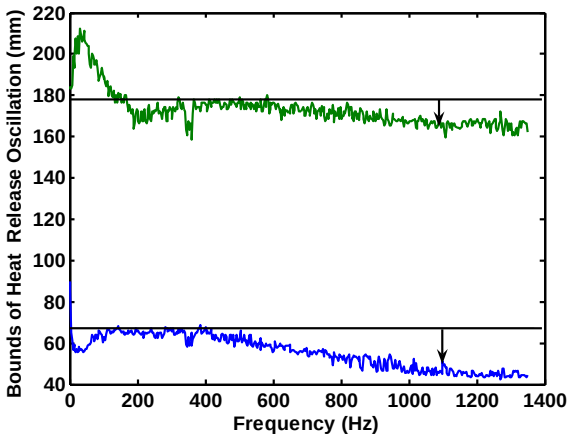

Figure 27 Upper and lower cutoff points as a function of frequency.

When the characteristics of the upper cutoff point is examined, we can see a initially sharp roll off at the low frequency end, but then a gradual rolling off at higher frequencies. This clearly showed that the region of intensity oscillations does move upstream as the frequency increased. It should be noted that the length scale of intensity variation does not change much in the frequencies measured. However the lower cutoff point should eventually stop regressing upstream at high frequencies once it reaches the burner exit, while the upper cutoff point will continue regressing upstream. Thus eventually the length scale of intensity variation will decrease with frequency although not significantly. This spatial variation of intensity can be expressed as a $e^{-\left(\left(y-L_{f,deviation}(\omega)\right)/L_{f,spread}(\omega)\right)^2}$ variation. However it should be noted that such a definition of intensity variation would most naturally require the cutoff value for the $L_{f,spread}$ to be e^{-1} instead of ¼.

The region of activity was further analyzed using coherence and cross spectrum calculation. For each frequency, the spatial point where the amplitude of oscillation was

the highest was identified and the coherence and cross spectrum between that point and the entire domain was calculated. Figure 28 shows the spatial variation of coherence between the reference point and the entire domain, while Figure 29 shows the spatial variation of the phase of the cross spectrum calculated for the same frequencies as the spectrum shown in Figure 25, i.e. 100.2, 200.4, 400.8, and 801.6 Hz.

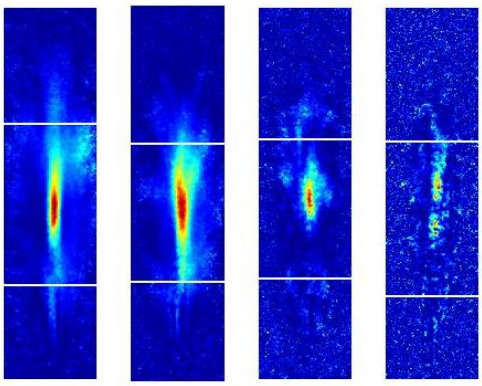

(a) (b) (c) (d)

Figure 28 Spatial variation of coherence with respect to the location of maximum amplitude for each frequency at frequencies of a. 100.2 Hz, b. 200.4 Hz, c. 400.8 Hz, and d. 801.6 Hz

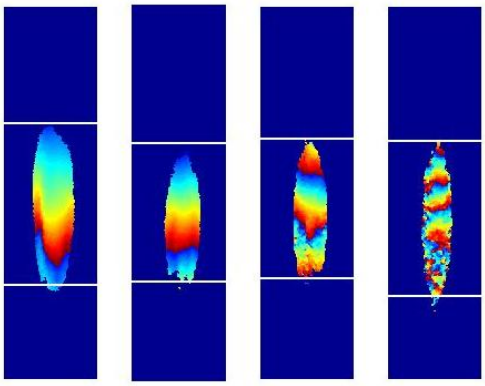

(a) (b) (c) (d)

Figure 29 Spatial variation of phase with respect to the location of maximum amplitude for each frequency at frequencies of a. 100.2 Hz, b. 200.4 Hz, c. 400.8 Hz, and d. 801.6 Hz

Figure 28 shows that the region of activity is well correlated at low frequencies (hence high spatial coherence), while it becomes almost uncorrelated at higher frequencies. Figure 28 shows the variation in the coherence region with frequency, clearly illustrating the decrement in the coherence region with frequency.

Figure 29 also shows that the phase images have fairly horizontal bands, and that the bands get closer at higher frequencies, suggesting the presence of a convective phenomenon in the heat release rate oscillations. However, this does not mean that the burning turbulent flame zone is physically being convected along the flame zone. This can be better explained with the use of a steady laminar flame. If there is an impulse perturbation in the flow, the flame will react locally to this impetus. The disturbance is felt at the base of the flame first and then the local adjustment of the flame to this impetus travels along the flame zone as the disturbance is carried along the flame by the flow. Hence, far away from both the flame base and flame tip, the flame will behave similarly to the impetus, but this behavior will occur at different points in time depending on how far down stream the flame location is with respect to the flame base. Hence a flame analysis will show as though the heat release rate disturbance is traveling along the flame while there is no actual convection of the flame zone itself.

Thus we can say that at low frequencies, the heat release oscillation in the flame is a highly coherent phenomenon where the disturbances are just convected downstream. However at higher frequencies this large scale oscillation behavior is increasingly replaced by the local turbulent fluctuations of the flame which are not spatially coherent. Hence the zone of high coherence occupies the entire flame zone at low frequencies while shrinking at higher frequencies.

In order to better evaluate this change in behavior of heat release oscillation with frequency, the individual frames of instantaneous heat release oscillations were radially integrated and then analyzed in the frequency domain. In order to reduce errors in calculation, only the pixels whose variance was more than 50% of the maximum value in

the variance image were used. Although this region would shift upstream at very high frequencies, Figure 27 suggests this movement is quite insignificant in the frequencies that could be measured with this high speed images. This effect will have to taken into account at very high frequencies (f >>1 kHz). Since the convective behavior is predominant in only one direction (along the axis of the burner), this integration effectively reduced the flame analysis into a one dimensional problem.

One Dimensional Spectral Analysis of Flame

This one dimensional analysis was performed for 2 sets of data:

Case1: D = 10.9 mm, Fuel = Natural gas, U_{ave} = 21.8 m/s, ϕ = 0.95, the turbulence intensity = 1.5%, Frame rate = 2700 Hz.

Case 2: D = 34.8 mm, Fuel = Acetylene, U_{ave} = 9.7 m/s, ϕ = 0.63 and the turbulence intensity = 8.5%, Frame rate = 2000 Hz.

Case 1 consisted of 4 sets of axial intensity variation of 8192 each. These sets were further divided in to ensembles of 1024 for Fourier analysis with a 50%. Hence the Δf for this set of data is 2.64 Hz. This is similar to the way the images were analyzed.

Case 2 consisted of 6 sets of axial intensity variation of 1023 each. These sets were further divided in to ensembles of 256 for Fourier analysis with a 60%. Hence the Δf for this set of data is 7.81 Hz.

Figure 30 shows the variation intensity oscillation as a function of frequency.

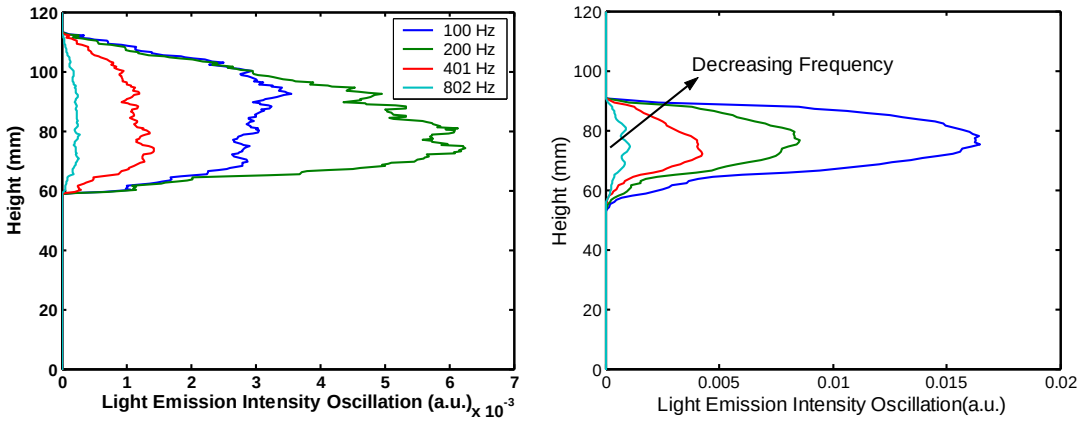

(a) (b)

Figure 30 Axial variation of intensity oscillation for the frequencies of ~100 Hz, 200 Hz, 400 Hz and 800 Hz for a. Case 1, b. Case 2

To further analyze the spatial relationship of heat release oscillations at various frequencies, the point where the overall intensity oscillation is the maximum is used as the reference point and then coherence and cross spectrum for all other axial locations are calculated. Figure 31 and Figure 33 shows the axial variation of coherence and phase of cross spectrum.

Figure 31 shows that the region of high coherence decreases as a function of frequency. This trend is better illustrated by the use of a coherence length scale. This $L_{f,\,coherence}(\omega)$ is defined as the characteristic length scale which fits the spatial coherence (for coherence > e^{-1}) using the curve-fit $e^{-\left(\left(y-L_{f,deviation}(\omega)\right)/L_{f,scoherence}(\omega)\right)^2}$. The spatial variation of $L_{f,\,coherence}(\omega)$ as a function of frequency is illustrated in Figure 32.

Figure 33 shows that the existence of convection phenomenon, which resulted in high coherence along the flame length at low frequencies. The convection velocity was found to be 15.3m/s for Case 1 (U_{ave} = 21.8m/s) and 12.4m/s for Case 2 (U_{ave} = 9.7m/s).

This convection velocity was calculated for all other cases that were imaged at 1000Hz. However, for the cases with high mean velocities, the variation in phase across the flame length was too low to make an accurate estimate of convection velocity. Figure

34 compares the convection velocity, for the cases where it was possible, to calculate to its mean velocity. We can see that the spread in the estimate of the convection velocity increased with increase in mean velocity. However we can still see that the convection velocity is of magnitude similar to the mean velocity. Thus the convection velocity being similar to the mean velocity further proves the theory on why the flame perturbations appear to have a convective behavior at low frequencies.

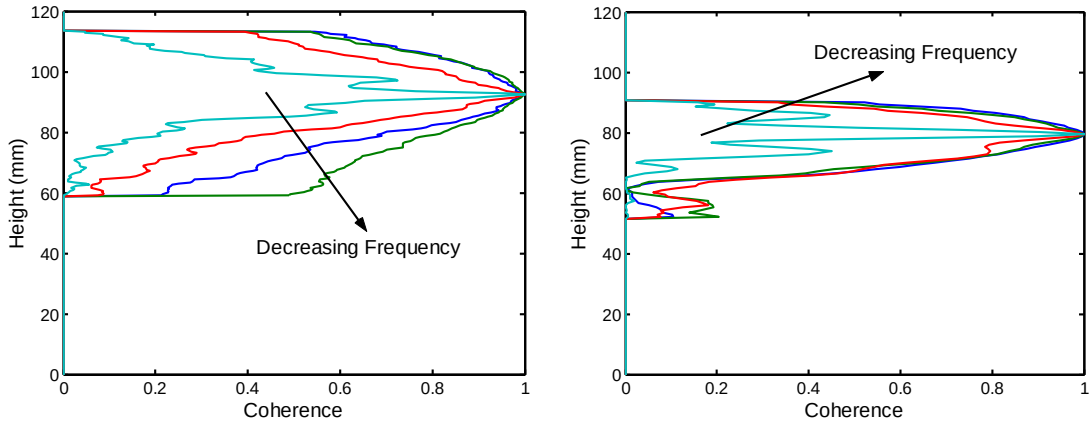

Figure 31 Axial variation of coherence with respect to the location of maximum intensity oscillation for a. Case 1, b. Case 2

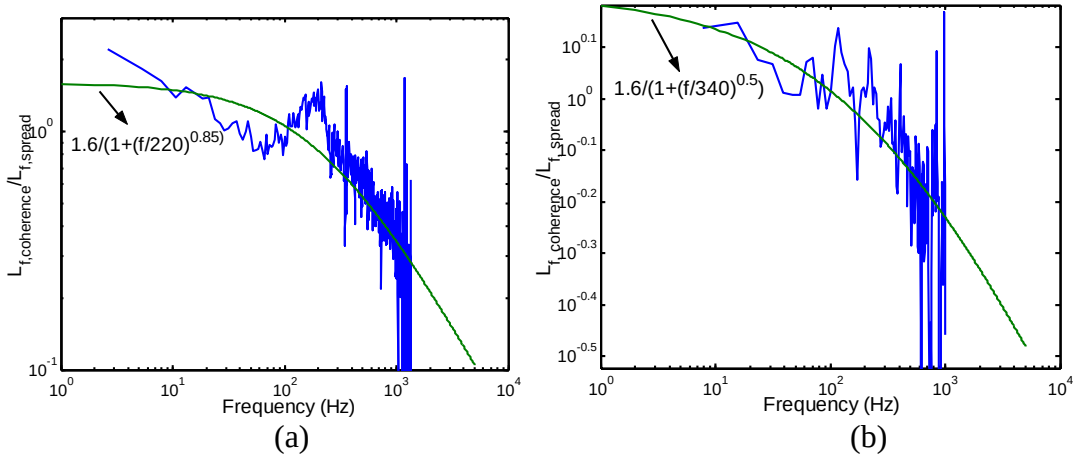

Figure 32 Comparison of $L_{f,coherence}$ with frequency for a. Case1, b. Case2

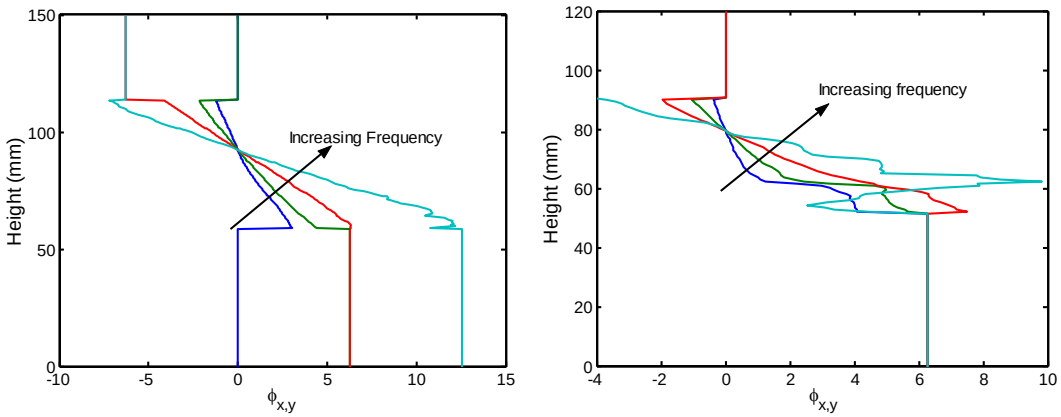

Figure 33 Variation of phase, with respect to the location of maximum variance, along the length of the flame for a. Case 1, b. Case 2

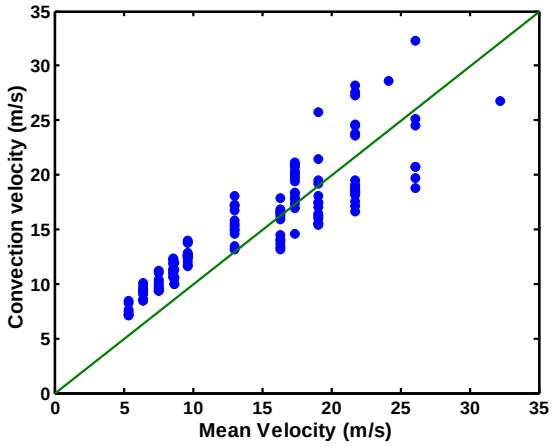

Figure 34 Comparison between convective velocity and the mean velocity

Recall the equation for acoustic spectrum, Equation 6 in Chapter 2:

$$P(\omega)=\frac{(\gamma-1)^2}{4\pi\rho_0 c_0^5}\omega^2\int\left\langle\hat{q}^*(y,\omega)\hat{q}(y+\Delta,\omega)\right\rangle e^{-ik_0\left(|\vec{x}-\vec{y}-\vec{\Delta}|-|\vec{x}-\vec{y}|\right)}d^3\Delta d^3y \quad (12)$$

Using Figure 30, Figure 31, Figure 32, and Figure 33 we can now evaluate the integral for this one-dimensional problem and can gain useful insight into this problem. Using the definition of coherence and cross spectrum:

$$\gamma^2(y,y+\Delta,\omega)=\frac{\left|\left\langle\hat{q}^*(y,\omega)\hat{q}(y+\Delta,\omega)\right\rangle\right|^2}{\left\langle\left|\hat{q}(y,\omega)\right|^2\right\rangle\left\langle\left|\hat{q}(y+\Delta,\omega)\right|^2\right\rangle} \quad (13)$$

$$\left\langle \hat{q}^*(y,\omega)\hat{q}(y+\Delta,\omega)\right\rangle = \left|\left\langle \hat{q}^*(y,\omega)\hat{q}(y+\Delta,\omega)\right\rangle\right| e^{-i\varphi_\Delta} \quad (14)$$

Figure 33 clearly shows a convective phenomenon. So the phase relationship between 2 spatial points with non-zero coherence is given by:

$$\varphi_\Delta = \frac{\Delta}{U_{convection}} \quad (15)$$

Thus

$$\left\langle \hat{q}^*(y,\omega)\hat{q}(y+\Delta,\omega)\right\rangle = \left(\left\langle \left|\hat{q}(y,\omega)\right|^2\right\rangle \left\langle \left|\hat{q}(y+\Delta,\omega)\right|^2\right\rangle\right)^{1/2} \sqrt{\gamma^2(y,y+\Delta,\omega)}\, e^{-i\omega\Delta/U_{convection}} \quad (16)$$

To obtain an analytical solution for this integral, further simplifications were performed.

1. The heat release also seems to have an $e^{-\left(\left(y-L_{f,deviation}(\omega)\right)/L_{f,spread}(\omega)\right)^2}$ dependence. However, obtaining an analytical expression with this behavior for spatial heat release distribution was not possible. Hence to further simplify the problem, the heat release fluctuation is assumed to be spatially uniform within the confines of the flame length.

$$\left\langle \left|\hat{q}(y,\omega)\right|^2\right\rangle = \left\langle \left|\hat{q}(\omega)\right|^2\right\rangle \quad (17)$$

2. The spatial coherence behavior can be expected to change when different points of the flame are used for the base point. In order to simplify this problem, spatial coherence behavior is assumed to be the same at all spatial locations and self similar with frequency and it has an e^{-y^2} dependence.

$$\gamma^2(y,y+\Delta,\omega) = \gamma^2\left(\frac{|\Delta|}{L_{f,coherence}(\omega)}\right) = e^{-\left(\frac{|\Delta|}{L_{f,coherence}(\omega)}\right)^2} \quad (18)$$

3. The coherence length scale has a fairly flat profile until it reaches a cutoff frequency and then it begins to roll off. This can be easily modeled as a low pass filter of the form:

$$L_{f,coherence}(\omega) = C\frac{L_{f,spread}}{1+\left(\frac{\omega}{\omega_{cutoff}}\right)^{n}} \quad (19)$$

Furthermore, the $e^{-ik\left(\left|\vec{x}-\vec{y}-\vec{\Delta}\right|-\left|\vec{x}-\vec{y}\right|\right)}$ term, reflecting different arrival times from various points in the source to the observer, is relevant only when the two source points are coherent with each other. At low frequencies, the entire flame is compact and, hence, this term is unity. At high frequencies, the zone of coherence shrinks and hence remains much smaller than the corresponding wave lengths. Hence the coherence function γ^2 over larger length scales tending to zero will outweigh the effect of the $e^{-ik\left(\left|\vec{x}-\vec{y}-\vec{\Delta}\right|-\left|\vec{x}-\vec{y}\right|\right)}$ term. Thus, the phase parameter plays little role in the autospectrum. However, it should be noted that it plays a very important role in coherence between acoustic measurements that are acquired in two non-collinear directions (see Appendix III). Overall the term $e^{-ik\left(\left|\vec{x}-\vec{y}-\vec{\Delta}\right|-\left|\vec{x}-\vec{y}\right|\right)}$ can be neglected in the autospectrum calculation.

Thus the equation reduces to:

$$P(\omega) = \frac{(\gamma-1)^2}{4\pi\rho_0 c_0^5}\omega^2\left\langle\left|\hat{q}(\omega)\right|^2\right\rangle\int_0^{L_{f,spread}}\int_{-y}^{L_{f,spread}-y} e^{-\frac{1}{2}\left(\frac{|\Delta|}{L_{f,coherence}(\omega)}\right)^2} e^{-i\omega\Delta/U_{convection}}\,d\Delta dy \quad (20)$$

Reorganizing the equation we obtain:

$$I(\omega) = \frac{P(\omega)}{\left\langle\left|\hat{q}(\omega)\right|^2\right\rangle}\frac{4\pi\rho_0 c_0^5}{(\gamma-1)^2} = \omega^2\int_0^{L_{f,spread}}\int_{-y}^{L_{f,spread}-y} e^{-\frac{1}{2}\left(\frac{|\Delta|}{L_{f,coherence}(\omega)}\right)^2} e^{-i\omega\Delta/U_{convection}}\,d\Delta dy \quad (21)$$

The analytical solution for this integral is given by:

$$
\begin{aligned}
I(\omega) = {} & \omega^2 \frac{e^{\frac{-b^2}{4a}-aL_f^2}}{4a^{3/2}}\left(2\sqrt{a}e^{\frac{b^2}{4a}-ibL_{f,spread}}\left(1+e^{2ibL_{f,spread}}-2e^{ibL_{f,spread}+aL_{f,spread}^2}\right)\right) \\
& + \omega^2 \frac{e^{\frac{-b^2}{4a}-aL_{f,spread}^2}}{4a^{3/2}}\left(e^{aL_{f,spread}^2}\sqrt{\pi}\left(\left(-ib-2aL_{f,spread}\right)Erf\left(\frac{-ib-2aL_{f,spread}}{2\sqrt{a}}\right)\right)\right) \\
& + \omega^2 \frac{e^{\frac{-b^2}{4a}-aL_{f,spread}^2}}{4a^{3/2}}\left(e^{aL_{f,spread}^2}\sqrt{\pi}\left(\left(ib-2aL_{f,spread}\right)Erf\left(\frac{ib-2aL_{f,spread}}{2\sqrt{a}}\right)\right)\right) \\
& + \omega^2 \frac{e^{\frac{-b^2}{4a}-aL_{f,spread}^2}}{4a^{3/2}}\left(e^{aL_{f,spread}^2}\sqrt{\pi}\left(2bErfi\left(\frac{b}{2\sqrt{a}}\right)\right)\right)
\end{aligned}
\tag{22}
$$

Where

$$a = \frac{1}{2L_{f,coherence}(\omega)^2}$$

$$b = \frac{\omega}{U_{convection}}$$

There 5 parameters (C, ω_{cutoff}, n, $L_{f,spread}$ and $U_{convection}$) that could determine the characteristics of the "integral". Hence it is critical that we understand the role each parameter plays in the neighborhood of the correlations determined by the data analysis.

The base condition that was used for comparison was that of Case1 (C = 1.6, ω_{cutoff} = 220Hz, n = 0.85, $L_{f,spread}$ = 0.099m and U_{ave} = 21.8m/s). It is assumed that the mean velocity is equal to the convection velocity, which is a reasonable approximation based on Figure 34. Figure 33 to Figure 39 illustrate the sensitivity of the integral to each of these parameters. First, Figure 35 clearly shows that the value of "n" plays little role in the determination of the peak frequency for the integral. Figure 36 shows that the variation in the cutoff frequency ω_{cutoff}, plays little role in the determination of the peak

frequency once it is greater than 120 Hz. Figure 37 shows that once the region of coherence is greater than or equal to the flame spread at the low frequencies, the C value plays very little role in determining the peak frequency. In contrast Figure 38 and Figure 39 show that the $U_{convection}$ and $L_{f,spread}$ plays a very important role in determining the peak frequency.

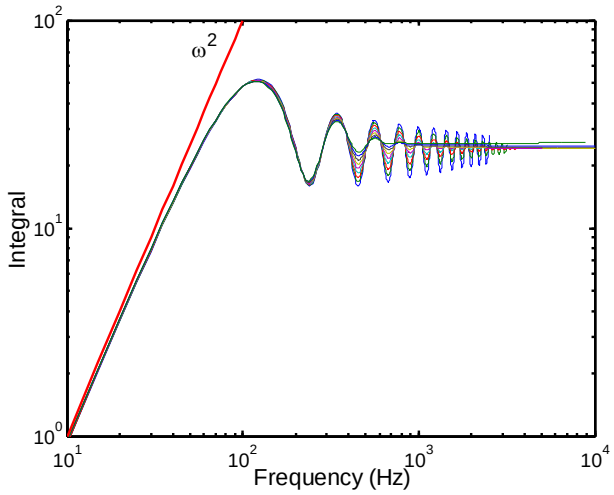

Figure 35 Variation in the integral for various n (0.3 – 1.1) with frequency for the case of $L_{f,spread}$ =0.099mm, $U_{convection}$ = 21.8m/s, C=1.6, and ω_{cutoff} = 220Hz

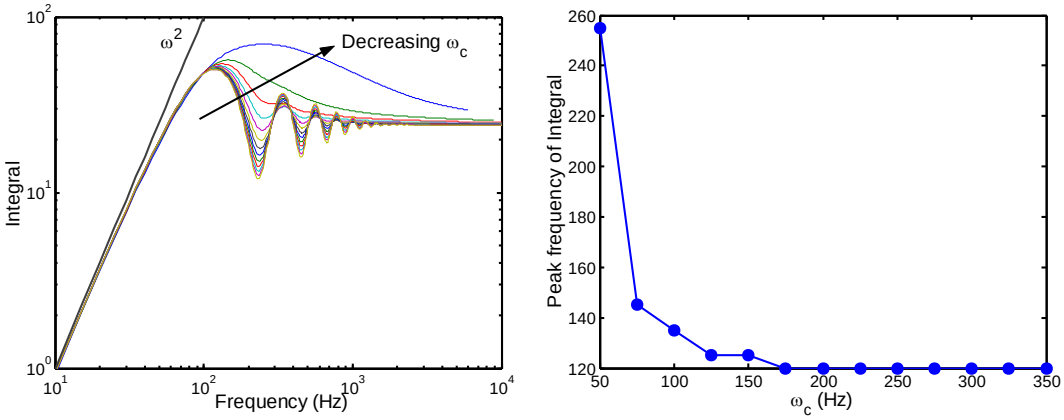

Figure 36 Variation in the integral for various ω_{cutoff} (50 – 300Hz) with frequency for the case of $L_{f,spread}$ =0.099mm, $U_{convection}$ = 21.8m/s, C=1.6, and n=0.85

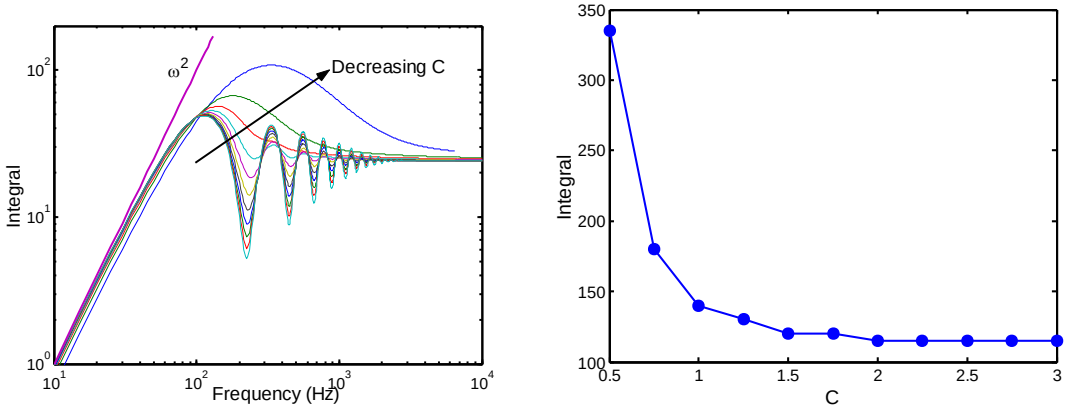

Figure 37 Variation in the integral for various C (0.5 - 3) with frequency for the case of $L_{f,spread}$ =0.099mm, $U_{convection}$ = 21.8m/s, ω_{cutoff} = 220Hz, and n=0.85

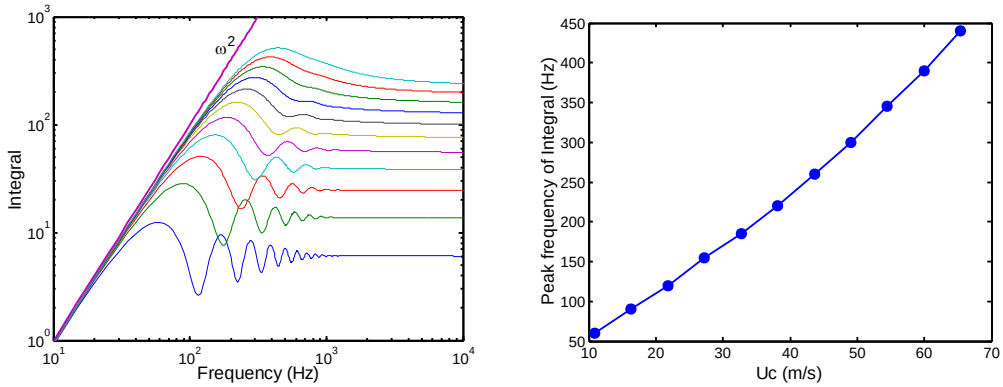

Figure 38 Variation in the integral for various $U_{convection}$ (10 – 65 m/s) with frequency for the case of $L_{f,spread}$ =0.099mm, C =1.6, ω_{cutoff} = 220Hz, and n=0.85

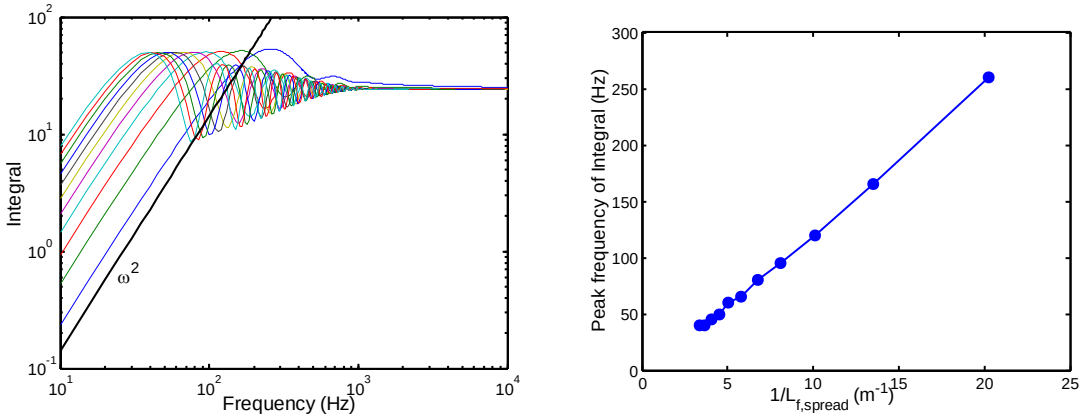

Figure 39 Variation in the integral for various $L_{f,spread}$ (0.05 – 0.3 m) with frequency for the case of $U_{convection}$ = 21.8m/sC =1.6, ω_{cutoff} = 220Hz, and n=0.85

Thus we can see that the factors that have a dominant effect on the peak frequency of the integral are the flame length $L_{f,spread}$ and the convection velocity $U_{convection}$. The peak frequency is directly proportional to the convective velocity and inversely proportional to the flame length. Thus we can see:

$$f_{peak\_integral} \propto \frac{U_{convection}}{L_{f,spread}} \quad (23)$$

Other than the variation in the peak frequency, the integral displays 2 characteristics for all the cases. At "low frequencies" the integral displays an ω^2 dependence, while at "high frequencies" the integral becomes independent of ω.

Summarizing this chapter we can say that at low frequencies, the disturbances along the flame are convected and hence flame oscillations at these frequency range is a large scale phenomenon. Hence the flame oscillations tend to be coherent over the entire flame domain. We can predict that its acoustic spectrum will have an ω^2 factor to its heat release oscillation spectrum.

$$P(\omega) \propto \omega^2 \left\langle \left| q(\omega) \right|^2 \right\rangle \quad (24)$$

In contrast, at "high frequencies" the region of high coherence starts shrinking as the localized behavior starts dominating. This shrinkage in coherence region contributes to a constant factor to its heat release oscillation spectrum. Hence:

$$P(\omega) \propto \left\langle \left| q(\omega) \right|^2 \right\rangle \quad (25)$$

The deviation from the ω^2 behavior occurs due to destructive interference between the noises produced by different parts of the flame. This behavior gives rise to an oscillatory behavior to the integral which eventually dies once the flame becomes increasingly incoherent spatially. The frequency at which the integral departs from its ω^2

behavior and begins its oscillatory behavior is strongly dependent on a strouhal number based on the convection velocity and $L_{f,spread}$. However it should be noted that the flame was assumed to be of constant amplitude spatially to get an analytical expression. In reality the spatial heat release fluctuations resembles more an $e^{-\left(\left(y-L_{f,deviation}(\omega)\right)/L_{f,spread}(\omega)\right)^2}$ type of distribution. This will result in the departure from ω^2 behavior occurring at higher frequencies and the post ω^2 zone will not be as oscillatory but will make a smooth transition to its constant values. This can be seen in Figure 40 where the integral is compared across the two different distributions of heat release oscillations. They both have an ω^2 dependence at low frequencies, whereas at high frequencies the constant distribution ripples down to a constant value while the e^{-y^2} distribution seems to be approaching the constant value only at $y\rightarrow\infty$.

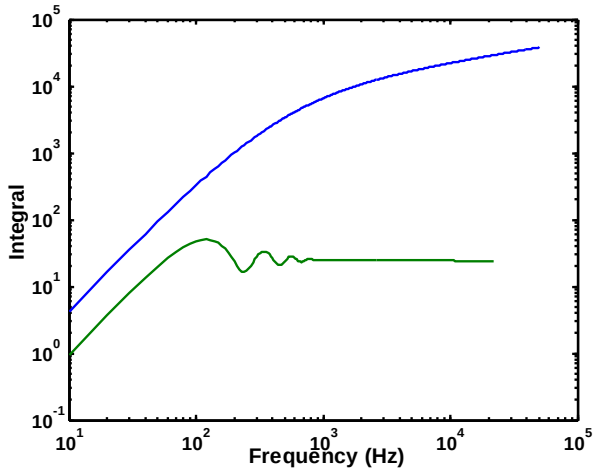

Figure 40 Comparison of the 1-D model integrals between the cases of constant amplitude of flame oscillations (green) and exp(-y^2) distribution of amplitude (blue)

CHAPTER 7

RESULTS

Chapter 6 described the turbulent flame dynamics, whose fluctuations are ultimately responsible for production of noise. This chapter presents actual acoustic measurements of turbulent flame noise and correlates these with the source dynamics. This acoustic data presented in this chapter were obtained from 530 test points obtained over a range of burner diameters (6.4 – 34.8mm), exit velocities (Re_D 10,000 – 32,000), turbulence intensities (u'/S_L 0.1-6.8), fuels (acetylene, natural gas and propane) and equivalence ratios (0.4 or tip loss to 1.1 or flashback). The test matrix is shown in Figure 41 and detailed in Appendix IV.

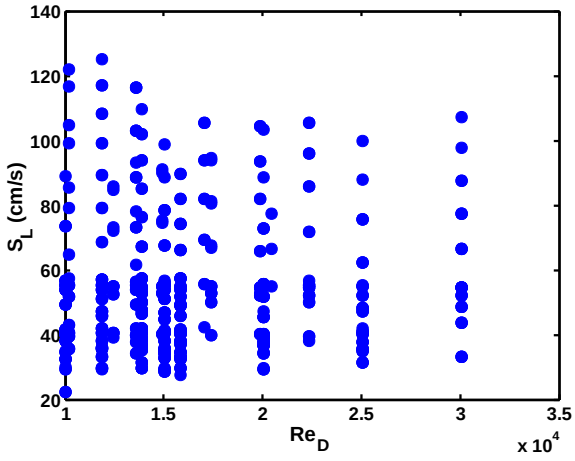

Figure 41 Range of S_L and Re_D for the entire test matrix

Source Location

The spectral images of the turbulent flames have indicated that the region of maximum heat release oscillation at low frequencies is near the flame tip. The location of maximum heat release oscillation should be the origin of noise production at those frequencies. Hence, the point where the intensity of the variance image of the flame is at

its highest can be considered as the origin of the noise source distribution. This region of noise production (that was identified from the variance image) is downstream of the nozzle exit, while the microphones were placed equidistant from the burner exit. Consequently the microphones cannot be equidistant from the origin of combustion noise. Since the microphones were placed in the far field of the noise source, this difference will have negligible effect on their relative amplitudes. However this will result in a time lag between the two microphone measurements. Figure 42 illustrates how the noise source being near the tip would result in a time lag ($\tau_{expected\ from\ image} = (R_{actual1} - R_{actual3})/c$) between the combustion noise data obtained by the microphones.

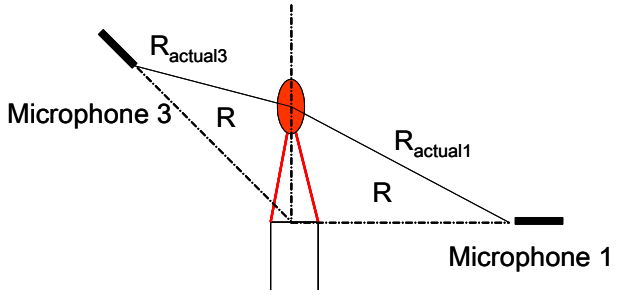

Figure 42 Schematic of the microphone location relative to the noise source location showing $R_{actual1} > R_{actual3}$

The acoustic data for the sample case discussed in detail in the previous chapter (Case 1: D = 10.9 mm, Fuel = natural gas, U_{ave} = 21.8 m/s, ϕ = 0.95 and the turbulence intensity = 1.5%) is used to further demonstrate this point. Figure 43 illustrates the results from two methods which could be used to calculate the time lag between 2 microphones that were placed at an angle of 45° and 90° with respect to the axis of the burner. The first one is a direct method using correlation between the raw acoustic data that was collected by the two microphones. The correlation coefficient was calculated for various time offset between the data. The time lag $\tau_{lag\_correlation}$ can be defined as that time offset between the two simultaneous data for which the correlation coefficient reaches a

maximum value. It can be seen in Figure 43b that the microphone placed at 45° leads the one placed at 90°, which is quite expected based on the Figure 42. The second method is the one that is based on the phase of the cross spectrum calculated between the two microphone measurements (discussed in detail in Chapter 4).

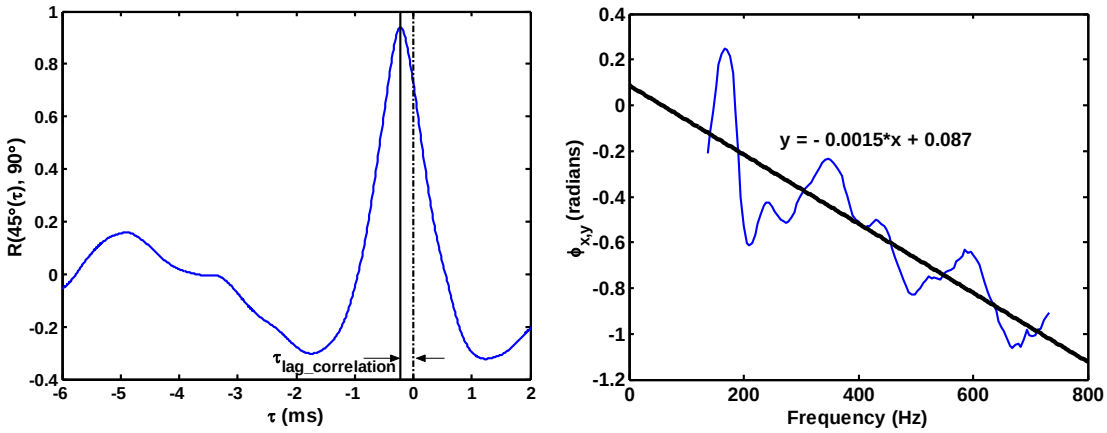

Figure 43 a. Correlation coefficient between 45° and 90° microphones as a function of time lag, b. Phase of cross spectrum between same two microphones in the frequency regime of high coherence for the case: D = 10.9 mm, Fuel = natural gas, U_{ave} = 21.8 m/s, ϕ = 0.95 and the turbulence intensity = 1.5%

The sample calculation below compares the time lags calculated using the two methods (using the acoustic data) to the expected time lag value (based on the origin of noise identified from the variance image). This clearly demonstrates the fact that the location of maximum intensity identified in the variance image is indeed the origin of combustion noise.

Distance of microphone from burner (R) = 1.01 m

Height of maximum intensity oscillation ($L_{f,\ deviation}$) =0.1026 m

Room Temperature = 21.8 °C $\Rightarrow$ speed of sound (c) = 344.4m/s

Actual distances of microphones from the flamer tip:

$R_{actual1} = \sqrt{R^2 + L_{f,deviation}^2} = 1.0212$ m

$R_{actual3} = \sqrt{R^2 + L_{f,deviation}^2 - 2RL_{f,deviation}\cos 45^\circ} = 0.9462$ m

Comparison of time lags calculated from the three methods:

$\tau_{lag\_expected\ from\ image}$ = (R_actual1 - R_actual3)/c = 218 μs

$\tau_{lag\_correlation}$ = 213 - 225 μs (difference in correlation coefficient < uncertainty)

$\tau_{lag\_crossspectrum} = 0.0015/2\pi$ = 239 μs

Figure 44 compares the time lags expected based on the noise source location identified from the variance images to the time lags calculated from cross spectra of all 530 cases. Figure 44 clearly demonstrates that the location of maximum intensity in the variance image is an excellent estimate of the location of actual noise production.

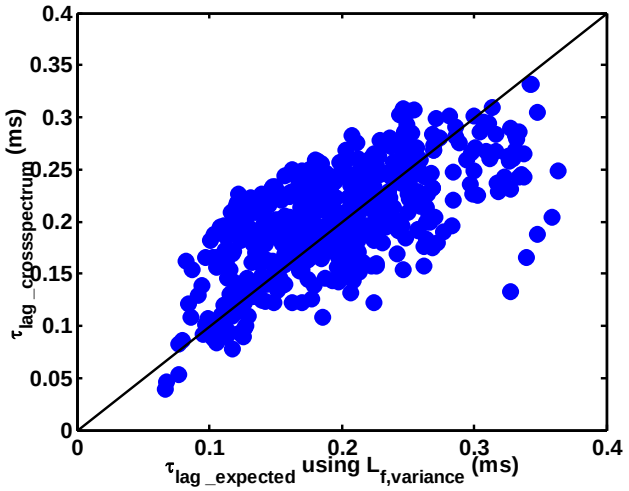

Figure 44 Comparison of time-lags calculated using cross spectrum to the time lag expected with the origin of combustion of noise characterized by $L_{f,variance}$ for all the cases

Coherence of Noise source

Appendix III showed that for a noise source, that consists of a set of spatially distributed independent random sources (equal in amplitude), the length scale of the

distribution determines the frequency up to which coherence between two non-collinear acoustic measurements is unity. At the same time, the length scale of the noise distribution determines the frequency up to which it is acoustically compact. Hence the two cutoff frequencies should be related. It should also be noted that the cutoff frequency for the coherence function is also a function of the angle between the two measurements.

Chapter 6 showed that the flame zone becomes spatially incoherent and, hence, independent at high frequencies. Consequently, the characteristic length scale of the spread of intensity in the variance image of the flame zone ($L_{f,spread}$) should determine the frequency at which the distribution would become acoustically non-compact. Since the three microphones were placed at different angles with respect to the flame, any two of them would be sufficient to determine a cut-off frequency for coherence.

Figure 45(a) plots the dependence of the coherence between the 45° and 90° microphone data upon frequency (for Case1). It shows that the sound at these two locations is highly coherent up to about 1 kHz, then begins to roll off, though in a non-monotonic manner, and becomes essentially zero about 4 kHz. This behavior of the coherence function is characterized by a cutoff frequency. As described in Chapter 4, the cutoff frequency for coherence was defined as the frequency at which the coherence dropped to 0.75 times its maximum value. Figure 45b compares the cutoff frequency measured from the coherence plot to length scale of the spread ($L_{f,spread}$) of variance image for all the cases. It can be seen that the product $K_{cutoff}\, L_{f,spread}$ is nearly constant, and that the correlation coefficient between K_{cutoff} and $L_{f,spread}^{-1}$ is 0.84. Thus we can see that a turbulent flame is not a coherent noise source at all frequencies, and the frequency

at which the coherence is a measure of the frequency up to which the flame is acoustically compact.

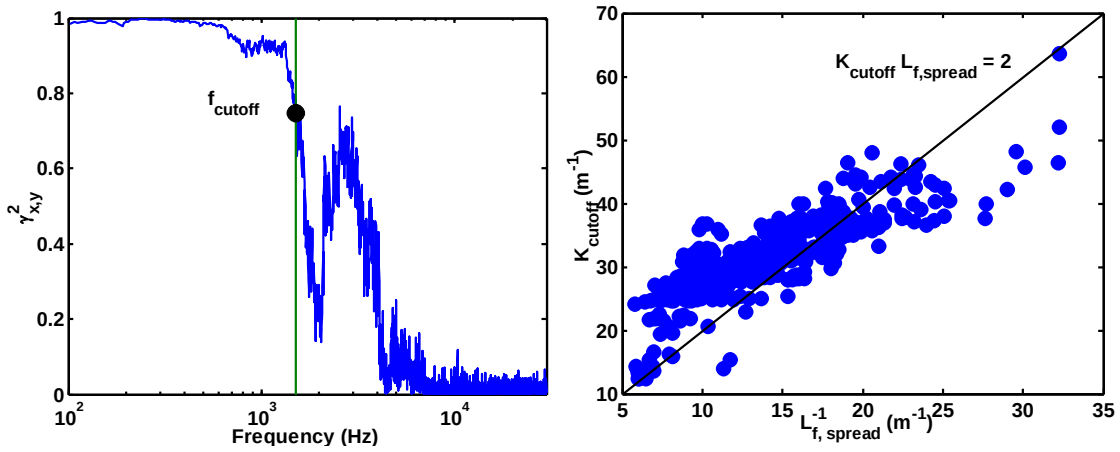

Figure 45 a. Dependence of coherence between the microphones at 45° and 90° upon frequency and the illustration of the cutoff frequency definition, b. Dependence of the cutoff wave number upon flame characteristic length, $L_{f,spread}$ for all data points

Spectral Characteristics

The model discussed in Chapter 6 predicted the spectral characteristics at various frequency regimes. The model predicted distinct low and high frequency behaviors and the presence of a characteristic frequency separating the two.

Figure 46a shows a typical spectrum of the overall chemiluminescence oscillation (summed over all the spatial points in its 1-D representation) of an open flame of Case 1 that was discussed in detail in Chapter 6. At low frequencies, it has a fairly flat amplitude profile with frequency, while rolling off at higher frequencies. Figure 46b compares the acoustic spectrum of the open flame to that of the cold flow when the flame is absent. It is quite clear that the combustion noise spectrum is significantly higher than the cold flow noise at most frequencies. The bias error shown in the figure is the same as the one measured in Figure 7. It can be seen that the presence of a large bias error at low frequencies, due to room reflection, can explain the presence of undulations in the

acoustic spectrum of combustion. The acoustic spectrum typically rises with frequency at low frequencies, reaches a maximum value before rolling off at higher frequencies.

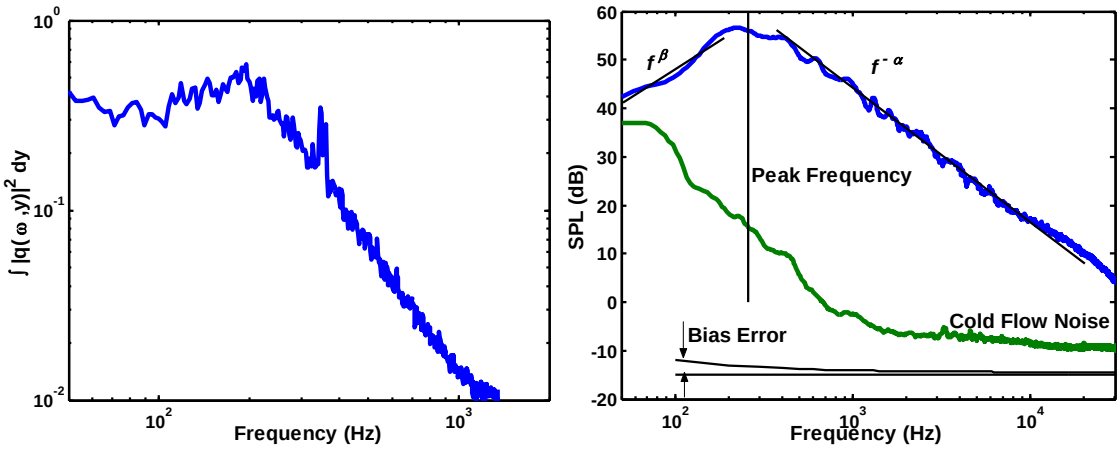

Figure 46 a. Spectrum of the overall heat release oscillation, b. Comparison of the acoustic spectrum of the flame with that of the cold flow and the bias error due to room reflections in the anechoic chamber

This behavior of the acoustic spectrum can be characterized by four parameters:

1. The frequency of peak acoustic emission (F_{peak})
2. Slope of the low frequency side during its rise ($P(f) \propto f^{\beta}$)
3. Slope of the high frequency roll off ($P(f) \propto f^{-\alpha}$)
4. Overall Sound Level produced by the flame (OASPL)

1. Peak Frequency

The model in Chapter 6 predicted that the behavior of $P(\omega)/\langle|q(\omega)|^2\rangle$ would be different on either side of a characteristic frequency, $U_{convection}/L_{f,spread}$. Hence, it can be expected that the characteristic frequency of the model be the same as peak frequency if the spectrum of heat release fluctuations is independent of frequency at least up to $U_{convection}/L_{f,spread}$. However it should be noted that the roll off in the heat release oscillations is also at a frequency similar to this characteristic frequency in the model which could also contribute to the presence of a peak in the acoustic spectrum. The roll-

off in heat release oscillation spectrum would significantly affect the characteristics of the peak frequency of the acoustic spectrum if and only if (1) the frequency at which the roll-off in the heat release oscillation spectrum begins is significantly lower than the characteristic frequency of the model, and (2) the roll-off in the spectrum occurs much faster than f^{-2}. This is because the model has an f^2 behavior at its low frequency side. So for the acoustic spectrum to actually roll-off, the spectrum of spatially coherent heat release fluctuations has to roll off faster than f^{-2} for it to induce roll off in the acoustic spectrum.

However it has already been shown that the low frequency fluctuations in the flame are due to large scale fluctuations of the flame tip. Hence, it would be unlikely that the frequency at which the heat release oscillations begin to be predominantly a localized phenomenon and hence begin roll off in amplitude be lower much than the characteristic frequency of the model. In addition, the spectra of heat release fluctuations have not been found be much faster than f^{-2} to effect a roll off in the acoustic spectrum. Hence we can expect a Strouhal number dependence of the peak frequency of the acoustic spectrum.

As shown in Figure 34, it can be expected that the mean velocity U_{ave} should scale the convective velocity $U_{convection}$. Thus, the peak frequency should be characterized by a Strouhal number that is based on U_{ave} and $L_{f,spread}$ being the characteristic velocity and length scale respectively. Figure 47 plots the peak frequency as a function of the ratio of the mean velocity and flame spread for all the cases for which the acoustic spectrum and the flame length ($L_{f,spread}$) were measured. It clearly shows a strong Strouhal number dependence of the peak frequency.

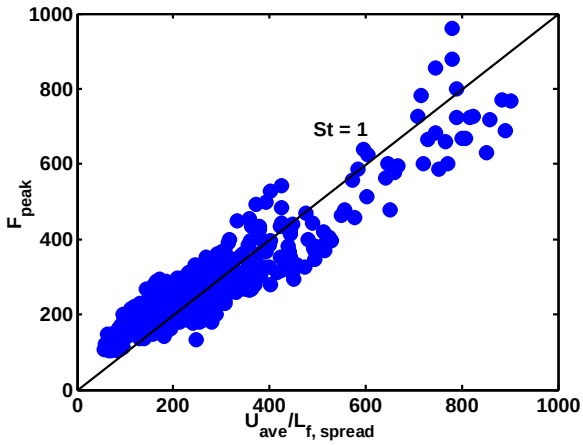

Figure 47 Strouhal number dependence of the peak frequency

Although a number of studies suggested that there has to be a Strouhal number correlation for the peak frequency, they did not substantiate their claim with the appropriate characteristic length and velocity scale. Strahle[15] and Smith[45] suggested a Strouhal number correlation based on burner diameter and jet exit velocity, similar to the jet noise spectral scaling. Strahle[15, 48] also attempted a correlation based on the integral length scale and intensity of velocity fluctuations in the underlying turbulence. Although both achieved limited success, they did not capture the known dependencies of F_{peak} upon chemical kinetics[41, 46, 47]. Abugov & Obrezkov[50] among others[47, 49] have suggested a scaling based on chemical kinetics alone. Abugov & Obrezkov[50] suggested that the characteristic scales for the Strouhal number scaling were the diameter of the burner and the laminar flame speed. However the problem with this approach is that it completely neglects the known influence of fluid mechanics upon peak frequency. For example, Smith & Kilham[45] showed that the peak frequency increased with flow velocity while the chemical parameters were held constant. Furthermore the correlations of the peak frequency were often done for a very narrow range of flame speeds and mean velocities.

This resulted in correlations that worked only in that narrow range of the parametric study.

In contrast the current study attempted to correlate over a much wider range of all the parameters that could affect the combustion noise properties and hence was able to demonstrate the deficiencies in all other characteristic length and velocity scale. The flame length, on the other hand, is the length scale that includes the effects of mean flow, turbulence and chemistry which was missing in other characteristic lengths such as diameter, integral length scale, etc. Thus a rational Strouhal number correlation was achieved over a wide range of flow conditions.

2. Low Frequency Slope (β)

The model predicted that the low frequency side of the acoustic spectrum will have a $P(\omega) \propto \omega^2\langle|q(\omega)|^2\rangle$ behavior. At low frequencies the $\langle|q(\omega)|^2\rangle$ has been found to have a typically flat profile or at least a weak dependence with frequency, i.e. $\langle|q(\omega)|^2\rangle \propto \omega^k : k << 1$ (see Figure 46a). Hence we can expect a $P(\omega) \propto \omega^2$ behavior at low frequencies.

To the best of our knowledge, the low frequency acoustic sideband has not been previously characterized in the literature. Accurate measurement of its characteristics is hindered by signal to noise problems, as this spectral range usually corresponds with regimes of high background noise and also the undulations due to room reflection.

In order to reduce the effect of room reflections, only the cases that had high peak frequency were used to characterize this parameter. Cases with high peak frequencies provided significant number of points in the low frequency side of the acoustic spectrum

that enabled the measurement of β with as little bias error as possible. Even then uncertainty in the measurement of β was quite high (~0.5).

However, only acetylene air flames in the 6.4 mm burner had F_{peak} significantly higher than 600Hz. Hence in Figure 48, which illustrates the range of values over which β varied, only those cases were plotted. Note that the value of β to be a nearly constant value around 2 confirming the result predicted by the model. However it has to be noted that the β value is slightly biased towards the higher side of 2. This could be due to a variety of reasons:

1. Bias error in the measurement of β due to the presence of undulations in the acoustic spectrum.
2. The spectrum of the heat release oscillations may have a slightly positive slope at low frequencies. This requires the chemiluminescence images of flames to be recorded for much longer time, so as to enable an accurate estimate of the slope of the spectrum of heat release fluctuations at that frequency range.

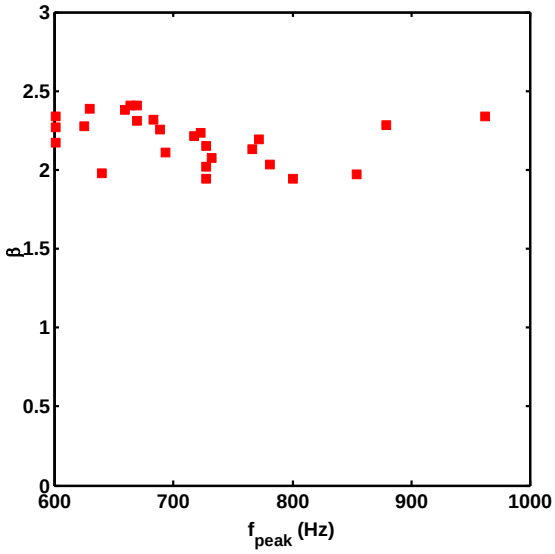

Figure 48 Dependence of low frequency decay exponent (β) upon F_{peak} for acetylene-air mixture in the 6.4 mm burner

3. High Frequency Slope (α)

Clavin & Siggia[16] and Clavin[17] provided insight into these decay exponents with their theoretical analysis of combustion noise. Using Kolmogorov scaling arguments and, in particular, assuming a $k^{-5/3}$ inertial subrange spatial velocity spectrum, they arrive at an acoustic power spectrum in the corresponding frequency range with an $\alpha = 5/2$ dependence. In contrast, the current study does not consider the transfer function between heat release fluctuations and upstream turbulence. The current model predicted that the high frequency side of the acoustic spectrum will have a $P(\omega) \propto \langle |q(\omega)|^2 \rangle$ behavior. Hence, the acoustic spectrum should follow the spectrum of heat release fluctuations at higher frequencies.

However, due to prohibitively large computer memory required to store long time-period of high speed images, high speed video were not obtained for all the cases. 1000 frames recorded at 1000Hz frame rate were obtained for all flame conditions. The only cases for which long time periods of high speed images were obtained was for the ones discussed in detail in Chapter 6 (Case 1 and Case 2). Figure 49 compares the spectrum of heat release oscillations for both Case 1 and Case 2 with its corresponding acoustic spectrum. The figure clearly shows that the roll off rates of the spectrum heat release fluctuations is similar to the acoustic spectrum roll off for both the cases. This can be better seen in Figure 50, where the transfer functions between the acoustic spectrum and the spectrum of chemiluminescence fluctuations for both the cases are shown. As expected from the model, the transfer function follows an f^2 dependence at low frequencies and becomes constant at higher frequencies. The undulations present in the transfer function are due to the ripples present in the acoustic spectrum (due to room

reflections). The deviation in the transfer function at high frequencies for Case 2 is most probably due to aliasing. This could've been avoided if the flame had been recorded at a much higher frame rate. Furthermore, the bandwidth of the heat release fluctuations measured is much lower than the bandwidth over which the acoustic spectrum rolls off. Hence in order to perform a quantitative study of the transfer function, the flames will have to be recorded at a much higher frame rate in order to overcome the issue to aliasing and to capture the decay rate exponent at much higher frequencies over which α is being estimated. However this could not be done with the available equipment.

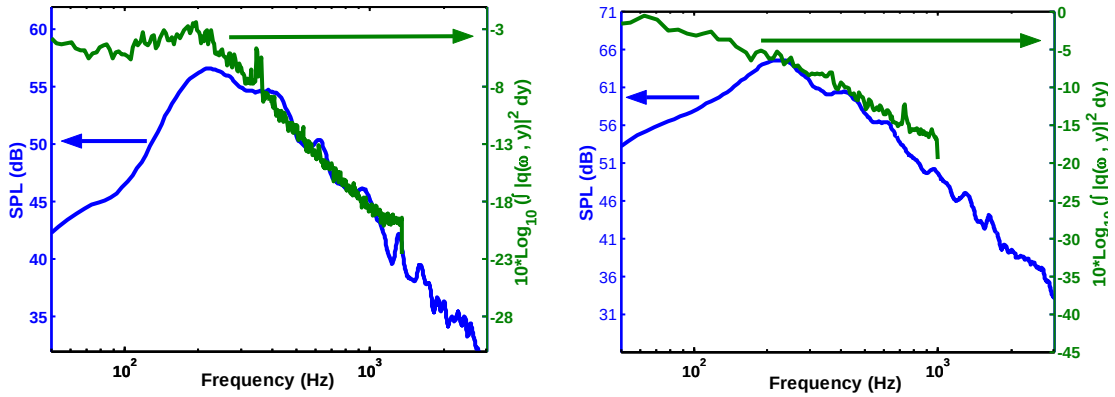

Figure 49 Comparison of spectrum of heat release fluctuations to the acoustic spectrum for a. Case 1 b. Case 2

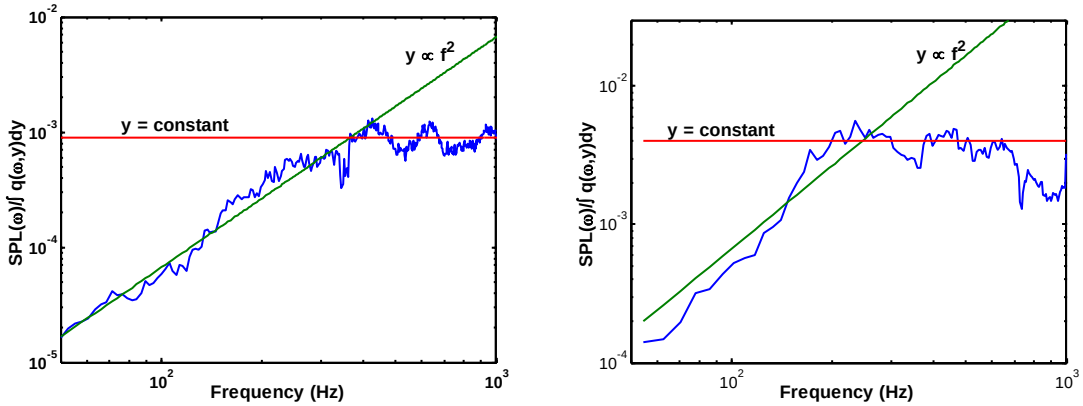

Figure 50 Comparison of transfer function between the acoustic spectrum and spectrum of heat release fluctuations for a. Case 1 b. Case 2

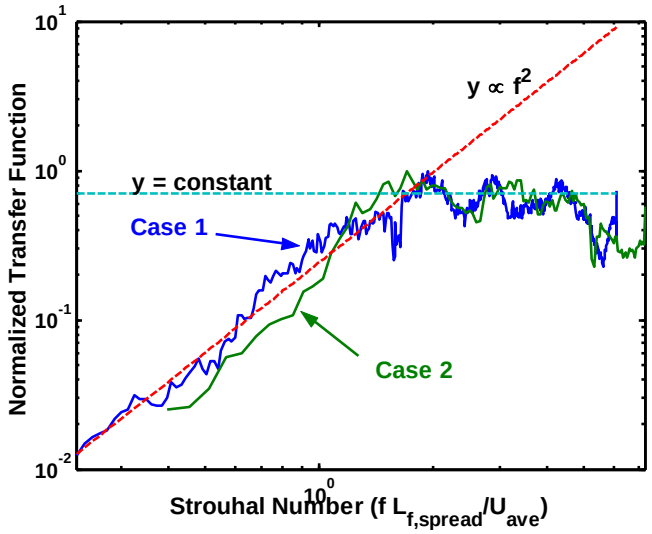

Figure 51 Comparison of the normalized transfer functions for Case 1 and Case 2

We next present correlations for α for all other cases where high speed imaging was not available. Figure 52 plots the value of α upon u'/S_L, F_{peak}, S_L and $T_{adiabatic}$. Note that the value of α ranges between approximately 2.2 and 3.1. Belliard [51] and Wäsle *et. al* [58] also measured values of α>2.5 in their data. We can see that the value of α does not correlate well with any of the flow parameters. The same was found to be true to all other parameters even in a multivariate regression. Hence a regression based on mean flow parameters is not possible to rationally correlate α.

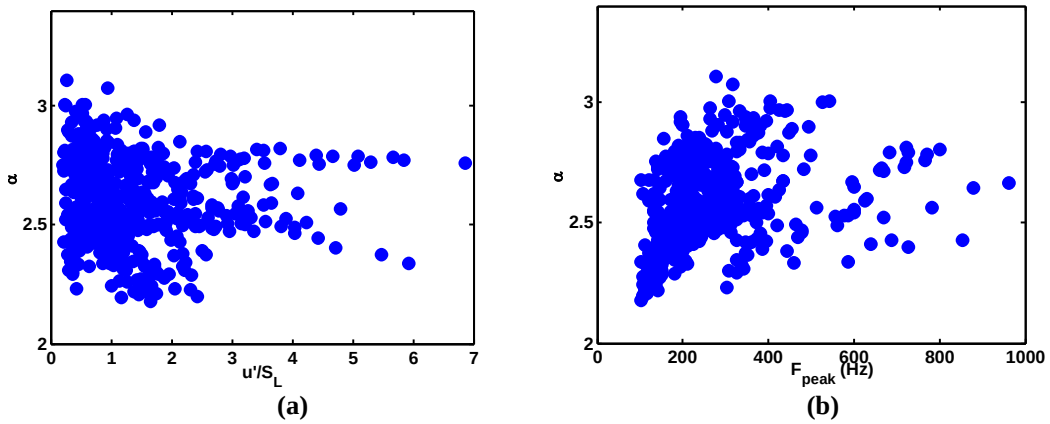

(a) **(b)**

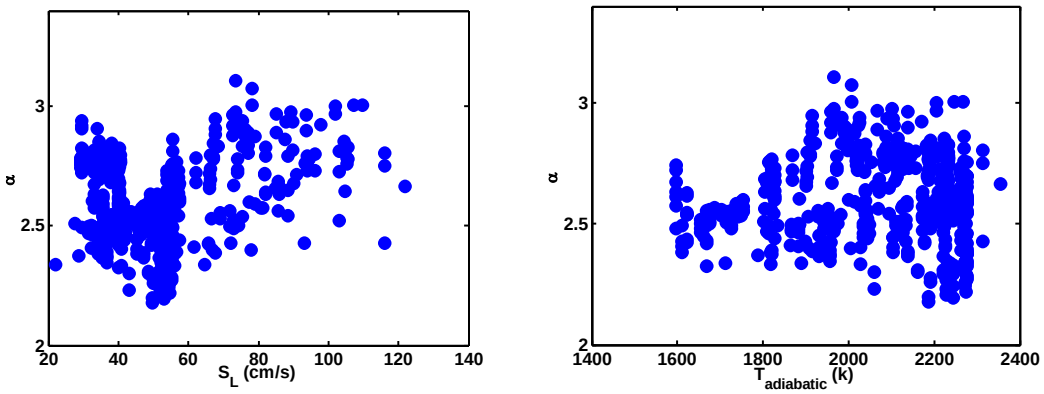

Figure 52.Dependence of high frequency decay exponent (α) upon a. u'/S_L b. F_{peak} c. S_L d. $T_{adiabatic}$

4. OASPL

It has already been shown that the heat release rate oscillations at frequencies around the peak frequency of acoustic emission are due to large scale motions of the flame at its tip. At these frequencies, the entire flame reacts to disturbances convected by the flow. Hence the overall noise produced by the flame should be characterized by the large scale heat release rate oscillation at a frequency characterized by the peak frequency. In Chapter 2 it was shown that the overall noise level produced by the flame is given by:

$$P = \frac{(\gamma-1)^2}{4\pi\rho_0 c_0^5}\int \overline{\frac{\partial q}{\partial t}\left(y, t-{}^{|\vec{x}-\vec{y}|}/_{c_0}\right)\frac{\partial q}{\partial t}\left(y+\Delta, t-{}^{|\vec{x}-\vec{y}-\vec{\Delta}|}/_{c_0}\right)} d^3\Delta d^3 y \quad (26)$$

In order to better understand how this integral is affected by the large scale heat release rate oscillation the integral is non-dimensionalized based on some characteristic large scale parameters of the flame.

(′) represents the non-dimensional form of any parameter and ($_{char}$) represents the characteristic value of those parameters:

$$P = P' P_{char}$$
$$q = q' \frac{Q_{char}}{V_{flame}} \quad (27)$$
$$t = t' \tau_{char}$$
$$x = x' x_{char}$$

Since we are interested in large scale heat release rate oscillations at a frequency around the peak frequency of acoustic emission, it is reasonable to assume that the characteristic heat release rate is actually the overall heat release rate of the flame and the time scale of heat release oscillation is the time period of oscillations near the peak frequency. Thus:

$$\frac{\partial q}{\partial t} \sim \frac{Q_{char}}{\tau_{char}} \quad (28)$$

where

$$Q_{char} = m_f H$$
$$\tau_{char} \sim \frac{L_{f,spread}}{U_{ave}} = \frac{1}{F_{peak}} \quad (29)$$

Furthermore the characteristic length scale associated in the integral has to be a flame length:

$$x_{char} = L_{f,spread} \quad (30)$$

Since the combustion has been shown to be a monopole type of source, the overall sound power can be characterized by the OASPL of any one of the microphone measurements. Thus the integral evaluating the overall sound pressure level can be non-dimensionalized to the form:

$$\frac{OASPL}{\left(F_{peak} m_f H\right)^2} \propto \frac{1}{P'} \int \overline{\frac{\partial q'}{\partial t'}\left(y', t' - \left|x' - y'\right| M\right) \frac{\partial q'}{\partial t'}\left(y' + \Delta', t' - \left|x' - y' - \Delta'\right| M\right)} d^3\Delta' d^3 y' \quad (31)$$

Figure 53a shows the correlation of the OASPL of combustion noise with respect to $(F_{peak}\ m_f\ H)^2$. We can see that the simple analysis adequately predicts the OASPL of combustion noise. A better fit for OASPL was determined using multivariate regression analysis of the OASPL, using the parameters F_{peak}, U_{ave}, (m_fH), S_L, D, Re, u', $L_{f,average}$, $L_{f,variance}$, and $L_{f,spread}$.

$$OASPL \propto F_{peak}^{2.47} U_{ave}^{0.93} \left(m_f H\right)^{2.23} S_L^{-0.37} D^{0.33} \mathrm{Re}^{-1.15} u'^{-0.02} L_{f,average}^{0.28} L_{f,variance}^{-0.95} L_{f,spread}^{0.59} \quad (32)$$

This produced a correlation that had a standard R^2 of 0.955. The multivariate regression method ANOVA prescribes a method to eliminate unnecessary parameters in a multivariate regression. This was used simplify equation 32 to the form:

$$OASPL \propto F_{peak}^{2.28} \left(m_f H\right)^{1.68} \quad (33)$$

This is plotted in Figure 53b. It can be seen that the new correlation was much simpler while losing very little in correlation (R^2 = 0.93). This relation follows closely the correlation put forth by the simplified analysis. The simplified model predicts OASPL with in ±5 dB whereas the Equation 33 predicts it with in ±4 dB. Thus the OASPL can be correlated using a very simple view of the noise production mechanism.

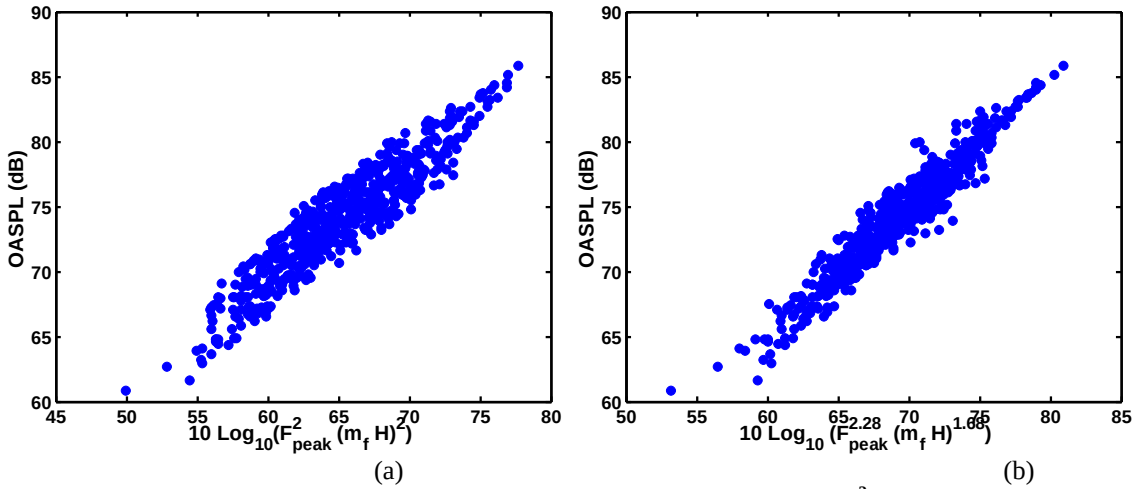

(a) (b)

Figure 53 Comparison of correlation for OASPL a. Simplified correlation, r^2 = 0.86 b. Regression analysis of current data, r^2 = 0.93

Thus all the parameters of combustion noise have been completely characterized.

Role of other flame length scales

Although the model predicts the flame length scale $L_{f,spread}$ as the only length scale parameter that can be used to characterize F_{peak} and acoustic compactness of combustion noise source, it is important to see whether the mean flame length can be used to characterize the same. The mean flame length is a very common parameter that is well documented in literature. Figure 54(a) compares F_{peak} with $U_{ave}/L_{f,average}$ while (b) compares K_{cutoff} as a function of $L_{f,average}^{-1}$. Figure 55(a) compares F_{peak} with $U_{ave}/L_{f,variance}$ while (b) compares K_{cutoff} as a function of $L_{f,variance}^{-1}$. They all show that both F_{peak} and the cutoff frequency for acoustic compactness can be characterized reasonably using any one of the three flame lengths. The Strouhal number correlation using mean flame length was also shown by Winkler *et al*[59].

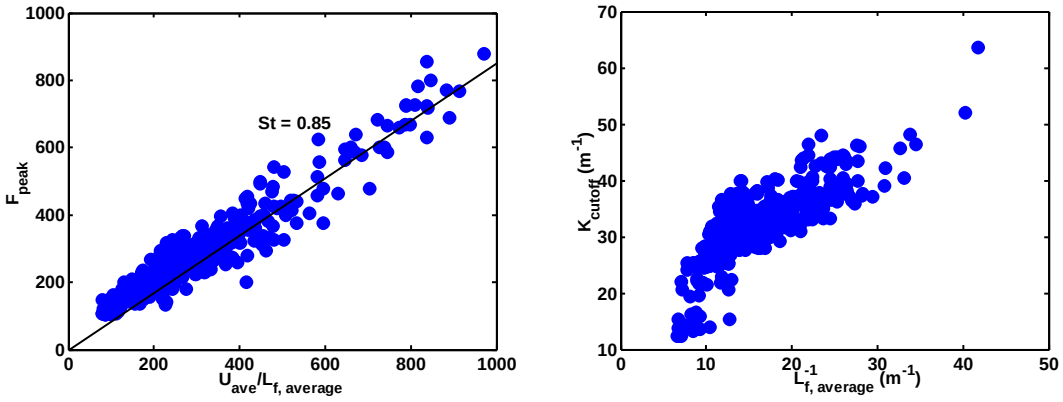

Figure 54 Employment of $L_{f,average}$ as a replacement for $L_{f,spread}$ in the correlation of peak frequency and cutoff frequency

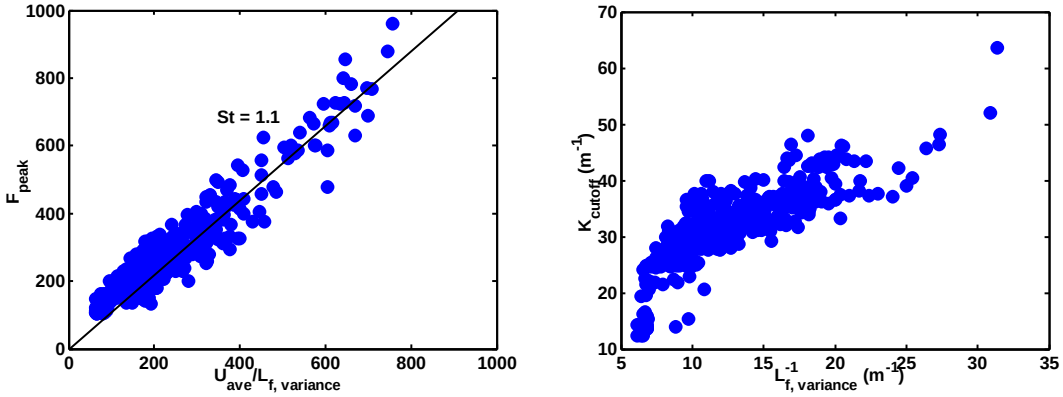

(a) (b)

Figure 55 Employment of $L_{f,variance}$ as a replacement for $L_{f,spread}$ in the correlation of peak frequency and cutoff frequency

However, $L_{f,average}$ being always smaller than $L_{f,variance}$, it doesn't represent the actual location of the combustion noise source. Hence the mean flame length cannot be used to locate the origin of combustion noise. Figure 56a clearly shows that the $L_{f,average}$ clearly underestimates the time lag between the microphones that were placed at 45° and 90° with respect to the burner axis. $L_{f,spread}$ being strongly affected by the cutoff set for its estimate, this is a very unreliable length scale to be used for time lag estimation between the two microphones. Hence in this case $L_{f,variance}$ is the only reliable flame length that can be used to estimate the origin of combustion noise.

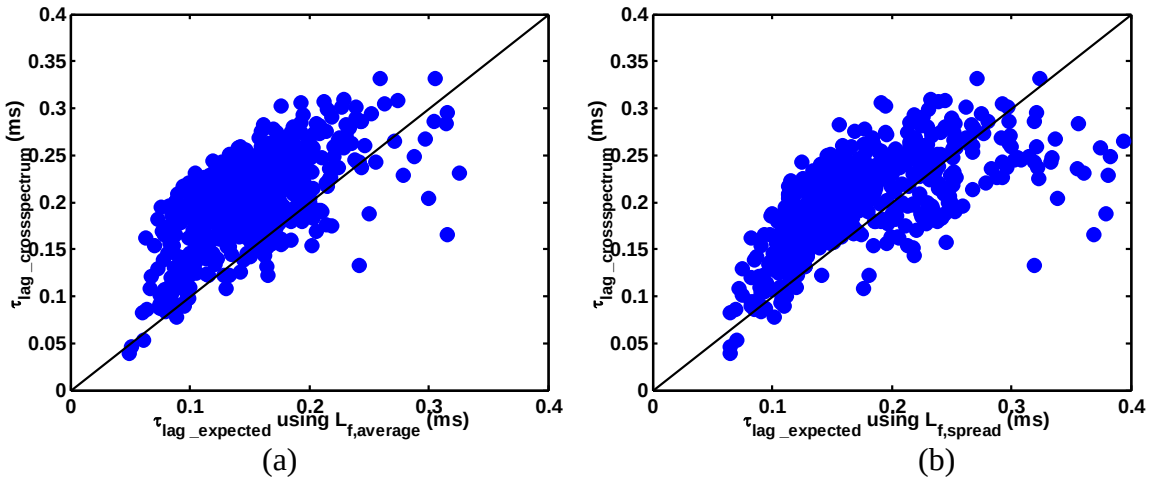

Figure 56 Employment of $L_{f,average}$, $L_{f,spread}$ as a replacement for $L_{f,variance}$ estimating the origin of combustion noise source

Furthermore even in the case of F_{peak} and cutoff frequency characterization, we have to exhibit caution. The relationship between the length scales might not be the same across different geometries. Hence, while comparing the characteristics of peak frequency and cutoff frequency across different flame stabilization mechanisms we have to use only the appropriate flame length scale.

Irrespective of which flame length we use, we still have to characterize how that parameter changes with the flow conditions. This is a more fundamental turbulent combustion problem and is beyond the scope of this research.

Limitations of Correlations

Although the scaling of combustion noise has been performed over a wide range of flow and geometry conditions, it still has severe restrictions on the flow conditions over which these correlations can be applied. The scaling of the parameters inherently assumes that the basic combustion zone characteristics remain the same across the range of flow conditions. However at low equivalence ratios, the flame tip (that has been shown to be the source location of combustion noise) weakens and eventually disappears. Figure

57 shows the disappearance of the tip in an open turbulent jet flame from a different burner design[46]. Although the combustor designs are different, this phenomenon was seen even in the current burner designs used in this dissertation.

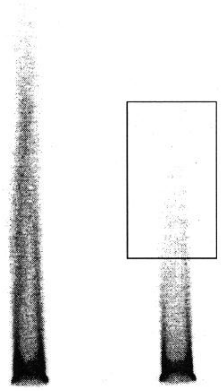

Figure 57 Photographs of flame showing disappearance of flame tip with decreasing equivalence ratios (U_{ave} = 9.7 m/s, D = 34.8 mm) of ϕ = 0.67, 0.61

This phenomenon significantly influences the low frequency noise production that has been shown to be produced in the flame tip zone. This can be seen in Figure 58, where the acoustic spectrum for the case with high equivalence ratio (and hence a very strong flame tip) has a sharp peak while the spectrum for the low equivalence ratio case (and hence a weaker flame tip) did not have a sharp peak. Furthermore the correlation for OASPL will over predict the overall noise produced in this condition as the absence of flame tip zone results in incomplete combustion that leads to lower noise production. Hence the flow conditions with partial flame extinction need to be treated separately, as their scaling will have to include flame extinction properties of the flame.

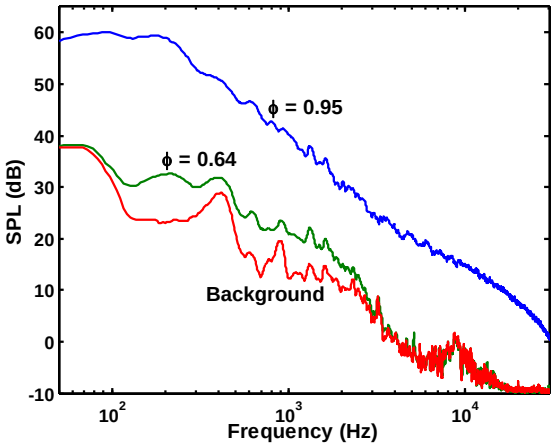

Figure 58 SPL vs. Frequency for a D = 34.8 mm, Fuel = Natural gas, U_{ave} = 9.7 m/s for the cases: ϕ = 0.95 (strong tip case) and ϕ = 0.64 (weak tip case)

CHAPTER 8

CONCLUSIONS AND FUTURE RECOMMENDATIONS

The objective of this research work was to measure the flow and acoustic properties of an open turbulent premixed jet flame and, thus, explain the spectral trends of combustion noise. In order to achieve this objective, a large database containing the acoustic signature, mean and turbulence velocity profiles, and high speed video of chemiluminescence images for each flame conditions was obtained. Measurements were performed for several burner diameters, flow velocities, turbulence intensities, fuels, and equivalence ratios.

These data were used to formulate a simplified model that provides a basis for a thorough understanding of the dynamics of a turbulent flame that causes its broadband noise production. This has led to a rational correlation of the parameters that describe a typical combustion noise spectrum: peak frequency (F_{peak}), low frequency slope (β), high frequency slope (α) and OASPL.

The important results that have been deduced in this dissertation are:

1. The actual location of combustion noise production was identified to be the flame tip zone. The location of the actual combustion noise source is characterized by its variance length scale $L_{f,variance}$. This parameter is quite similar to the "acoustic center" identified by Shivashankara[53] although he did not use it to describe the flame dynamics.
2. The cutoff frequency characterizing the acoustic compactness of combustion noise source is characterized by the spread of the flame tip zone ($L_{f,spread}$). This is a very important result because advanced techniques like the three microphone

techniques used to separate combustion noise from other flow noise assume that the combustion noise is coherent at all frequencies[60]; This result shows that assuming such a model can provide erroneous results, particularly at frequencies where the combustion is a non-compact source and its amplitude is comparable to the flow noise.

3. The frequency of peak acoustic emission F_{peak} has been found to be characterized by a Strouhal number whose characteristic velocity scale is the mean velocity U_{ave} and the characteristic length scale is the spread of the flame tip zone $L_{f,spread}$. This result resolves the conflicting correlations that have been published in the literature as the flame length encompasses the effects of the mean flow, turbulence and chemical kinetics that have been individually shown to affect F_{peak}.
4. The OASPL of combustion noise production was found to be proportional to $(F_{peak}\ m_f H)^2$ which closely resembles the source term in the wave equation.
5. The transfer function between the acoustic spectrum and the spectrum of heat release rate fluctuations has been shown to have an f^2 dependence at low frequencies. The actual measurement of the parameter characterizing the low frequency slope (β) was performed only for the cases with large F_{peak} values. Since the slope of the heat release fluctuations was essentially flat at those frequencies, the value of β was found to be ~2
6. The transfer function between the acoustic spectrum and spectrum of heat release rate fluctuations has been shown to be a constant at high frequencies. However a parametric study of the heat release fluctuations using high speed chemiluminesence images could not be performed with the available equipment.

Hence it is recommended that the characterization of the parameter α be further investigated either with the use of a photomultiplier or when higher speed cameras in conjunction with faster computers are available.

Overall the large scale oscillation of the flame has been found to be the chief contributor of noise from a combustion zone and hence explains the scaling of combustion noise parameters. This provides valuable insight into how the noise from other types of combustion systems, like a swirl stabilized flame or a bluff body stabilized flame etc, should scale.

For example in a swirl stabilized flame there are two dominant velocity vectors: the axial velocity and the azimuthal velocity. The large scale fluctuations travel along a helical path with the large scale structure of the flame being helical. Hence the flame length measured along the helical path and the mean velocity along the helical flow path should be the characteristic length and velocity scale for a Strouhal number scaling of its noise spectrum. However for a given swirler design, the velocity along the axial and azimuthal direction are related. Similarly, the flame length measured along the helical path will be related to its axial length. Hence a swirl stabilized flame should also have a Strouhal number scaling similar to the jet flame established in this study. When different swirler designs are compared, the ratio of the helical path flame length to its axial flame length will be the same as the ratio of the velocity along the helical path to its axial velocity. Hence we can expect the value of the Strouhal number across different swirler designs can be expected to be similar. The scaling established in this study just requires the large scale disturbances to travel along the flame length at a set mean velocity.

Overall this work provides a thorough understanding of combustion noise production mechanism and thus providing physics based correlations for combustion noise spectra. However, there is a need for further investigations in this area even for this simplified flame structure. Further characterization and correlation of the high frequency slope α is still needed. Furthermore, combustion noise has to be characterized for other flame stabilization mechanisms to ensure that the correlations that were established in this study are universal.

APPENDIX I: ERROR ANALYSIS

In order to ascertain the combined uncertainty, it is important to account for all the individual factors while assessing the uncertainty. The combined uncertainty in the measurement system is due to the following factors:

1. Influence of Microphone Calibration

The microphones were calibrated using a CEL 284/2 calibrator. The calibrator had an uncertainty of ±0.3dB @ 95% probability (implying a 2σ).

$$u_{calibrator} = 0.15dB$$

2. Influence of Microphone Response

The microphone manufacturers, Bruel & Kjaer, report that the 4191(1/2" microphone) has an uncertainty of 1dB and the 4939(1/4" microphone) has an uncertainty of 2dB within 95% confidence.

$$u_{1/2"microphone} = 0.5dB$$
$$u_{1/4"microphone} = 1dB$$

3. Influence of Filter Response

The digital manufacturer, Krohn-Hite, did not provide any information regarding its compliance to IEC 1260 standard. However based on its passband uncertainty they provided, it was assumed that the filter was a class 0 filter. Hence its combined uncertainty was assumed to be 0.21dB. However the filter was used for both the high pass and low pass filtering of the signal. Hence uncertainty of the filter has to be accounted twice in the final analysis.

$$u_{filter} = 0.21dB$$

4. Influence of Angle of Incidence

The microphones were carefully placed within ±10° from the direction of the source. Since the microphones were fairly insensitive to such small angles of incidence, the error due to variation in angle of incidence was neglected.

5. Influence of Microphone positioning

The position of the microphones was measured using a measuring tape. The uncertainty in the measurement of the distance between the microphone and the burner was estimated to be ±6.4mm. Since the microphones were placed at a distance of 1.02m from the burner, the uncertainty in the acoustic measurement assuming a $1/R^2$ dependence was found to be

$$u_{microphoneposition} = 20\log_{10}\left(\frac{1016+6.4}{1016}\right) = 0.05dB$$

6. Influence of Finite Fourier Transform

The spectral representation has an additional uncertainty due to the use of finite length fourier transform. The variance in acoustic pressure that is used for OASPL measurement also has uncertainty due to the use of finite number of samples in its estimate. However, since a large number of samples were used its estimate (1,048,576 samples) the uncertainty in its estimate is quite negligible. Similarly the 1/3 octave representation will also have negligible error since entire set of 1,048,576 samples were numerically filtered into appropriate frequency bins before the variance was estimated. In order to estimate the spectrum the 1,048,576 sample were divided into 64 bins and then the spectrum for the individual bins were estimated and then averaged. Furthermore the spectrum was further averaged in the frequency space across 15 neighboring frequency points. Hence the total uncertainty expected is given by:

$$u_{FFT} = 20\log_{10}\left(1+\frac{1}{\sqrt{64\times 15}}\right) = 0.28dB$$

The combined uncertainty of the measurement due to all its factors is given by:

$$u_c^2 = u_{calibrator}^2 + u_{microphone}^2 + 2u_{filter}^2 + u_{microphoneposition}^2 + u_{FFT}^2$$

For the 4191 microphone the combined uncertainty is:

$$u_{\frac{1}{2}\text{"mic-combined}} = \left(0.15^2 + 0.5^2 + 2\times 0.21^2 + 0.05^2 + 0.28^2\right)^{\frac{1}{2}} = 0.66dB$$

For the 4939 microphone the combined uncertainty is:

$$u_{\frac{1}{4}\text{"mic-combined}} = \left(0.15^2 + 1^2 + 2\times 0.21^2 + 0.05^2 + 0.28^2\right)^{\frac{1}{2}} = 1.1dB$$

In order to estimate the uncertainty at 95% probability we have to multiply a factor of 2 to these uncertainties, if we assume the underlying distribution of uncertainty to be Gaussian. Therefore the combined uncertainty of the microphones is given by:

$$u_{\frac{1}{2}\text{"mic-combined}} = 1.3dB \text{ and } u_{\frac{1}{4}\text{"mic-combined}} = 2.2dB$$

Furthermore the calculation of the combined uncertainty of OASPL measured by the microphones will have to neglect the uncertainty in FFT. Therefore the combined uncertainty in the OASPL is given by:

$$u_{\frac{1}{2}\text{"mic-combined}} = 1.2dB \text{ and } u_{\frac{1}{4}\text{"mic-combined}} = 2.1dB$$

APPENDIX II: ANECHOIC CHAMBER CHARACTERIZATION

Introduction

An anechoic chamber is a room that is insulated from external sound and prevents reverberation in order to measure the "pure sound" of a sound source without any interference. In other words, an anechoic chamber is a room to realize a free field environment. However a practical anechoic chamber has to be assessed for its ability to provide such a free field environment for all the frequencies of interest.

Among many methods proposed for the qualification of anechoic chambers, the method defined in ISO 3745[56] is widely used. This method is based on the fact that the sound pressure level decreases by 6 dB per doubling the distance in the free-field condition, which is known as the inverse square law. The objective of characterizing an anechoic chamber is to determine the maximum radius between a sound source and a microphone where the deviation from the inverse square law settles within some tolerance.

This method requires an omni-directional sound source or a monopole sound source. Ahuja[55] investigated the construction method of a device which provides laboratory simulation of point monopole and dipole sound sources. Saussus[61] evaluated the performance of a number of sound source designs for anechoic chamber qualification.

Measurements along radials extending from the source are called a traverse. Cunefare *et al*[62] evaluated the merits of continuous traverses versus discrete traverses. A continuous traverse is obtained by continuously moving a microphone along a radial and continuously recording acoustic data. A discrete traverse is obtained by moving a microphone with a discrete step and recording data at each step. They qualified the free-

field performance for both continuous and discrete traverses using pure tones and broadband random noises. Their pure tone analysis indicates that coarsely discrete samples cannot capture the complexity of the increased deviation with increasing frequency, thus continuous traverses are necessary for pure tones. On the other hand, even coarsely spaced discrete samples were found to be able to yield adequate representations for broadband noise analysis. They concluded anechoic chambers should be tested with pure tones and a continuous traveling system, however, their results implies discrete traverses have merits for broadband analysis since continuous traverses need a precisely controlled automated traverse system in addition to a large capacity of data storage. The purpose of our anechoic chamber is to analyze the acoustic properties of turbulent flames whose acoustic emissions are broadband in nature. Hence, we applied discrete traverse for our characterization of the chamber.

The purpose of this appendix is to present on the general descriptions and the acoustical characteristics of the anechoic chamber. We used a monopole sound source and two burners of different exit diameters (34.8 mm and 10.9 mm).

Sound sources

The acoustic data reported in this appendix were obtained from a point monopole sound source and two burners of different exit diameters (34.8 mm and 10.9 mm). The monopole sound source consists of an inverse conical horn mounted to an acoustic driver as shown in Figure 59.

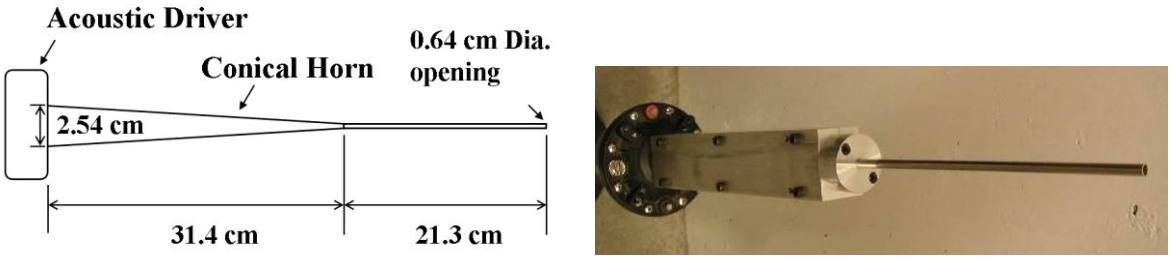

Figure 59 Sketch and photograph of point monopole sound source made using an inverse conical horn

Experimental Procedure

In order to assess the free-field performance of the chamber, noise spectra measurements along four paths were conducted for three types of sound sources: a point monopole sound source, two burners of different burner diameters (3.48 cm and 1.09 cm). The four paths were going horizontally from a sound source into four corners of the chamber as shown in Figure 60. These paths were chosen in order to take as many traverse data as possible. The four paths were labeled as A, B, C and D as shown in Figure 60.

A sound source was placed where a combustor should be placed; beneath the high temperature exhaust. Two microphones were used for each measurement: a reference microphone and a traverse microphone. The use of a reference microphone is advised in ISO 3745[56] in order to verify that the source output is consistent during the test.

A reference microphone was fixed at 101 cm distance from the sound source on the line starting horizontally from the source and going perpendicular to a side wall as shown in Figure 60.

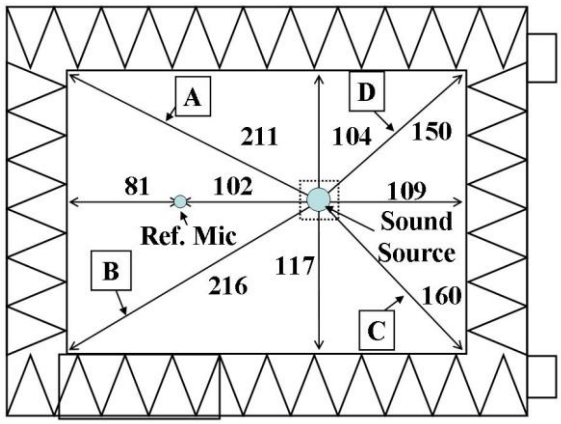

Figure 60 Definitions and dimensions (cm) of the four paths. Location of the sound source and the reference microphone

For each measurement, a traverse microphone was moved manually away from the sound source with the discrete interval of 10.16 cm along the four paths. The starting position of a measurement was at 20.32 cm distance from the sound source. A measurement was continued until the microphone cannot go closer to the walls.

The two microphones simultaneously measured the noise produced by the sound source. The raw acoustic data was converted into PSDs (in one third octaves) by using a series of numerical one third octave band filters.

Results and Discussion

Plot of the deviation from the reference sound pressure level versus distance from the source was used for assessing free-field performance of the chamber. The deviation from the reference sound pressure level is computed by

$$\Delta L(r) = L(r) - L_{ref} \qquad \textbf{(34)}$$

where L(r) is the sound pressure level measured by the traverse microphone at distance r from the sound source. L_{ref} is the sound pressure level measured by the reference microphone fixed at 102 cm distance from the source. Theoretically, the deviation $\Delta L(r)$

decreases by 6dB by doubling the distance from the source and becomes 0 at r = 102, if the sound source is omni-directional and the chamber is a perfect free-field environment.

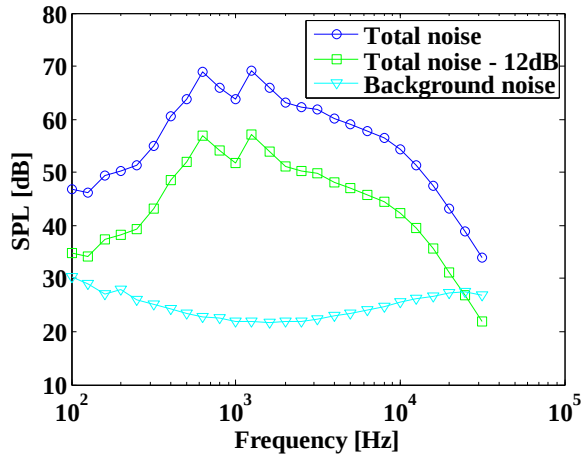

Figure 61 Sound spectra of the total noise and background noise measured at 102 cm distance from the monopole sound source on the path A

The ratio of background noise in total noise is an important factor when evaluating data. In general, if the background noise is smaller than the total noise by 12dB, it can be neglected. Figure 61 shows sound spectra of the total noise and background noise measured at 102 cm distance from the monopole sound source on the path A. In this case, the 12dB law indicates the background noise is dominant above 2500 Hz at which "Background noise" curve crosses with "Total noise – 12dB" curve.

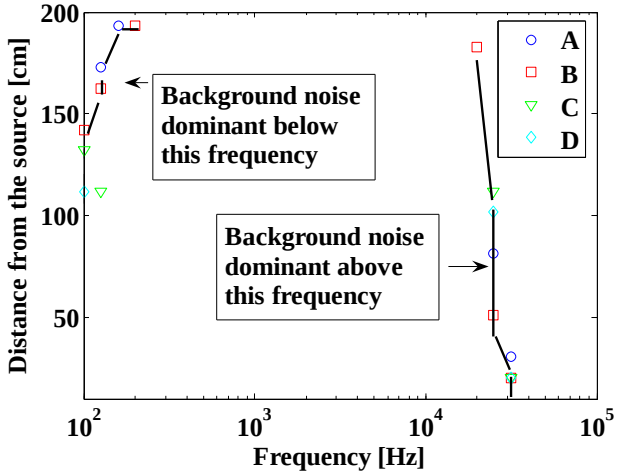

Figure 62 Frequency ranges where background noise is dominant in the anechoic chamber

Figure 62 shows the frequency range where background noise is dominant in the anechoic chamber. This plot can be generated by finding the crossing points of "Background" curves and "Total noise - 12dB" curves in sound spectra figures such as Figure 61 for monopole sound tests on all the four paths. Background noise can be neglected in the region encircled by the solid curves; data should be taken in this region. We must be very cautious about using this curve though because the two curves move closer to each other as the source signal strength decreases.

The results for the measurements along the path A are presented from Figure 63 to Figure 68. The results for the measurements along the path B are presented from Figure 69 to Figure 74. The results for the measurements along the path C are presented from Figure 75 to Figure 80. The results for the measurements along the path D are presented from Figure 81 to Figure 86.

The figures plot the deviation in the sound pressure level from that measured from a fixed reference microphone. The plots for most frequencies follow the inverse square law up to some distance from the source. The region, where the effect of the reflections from the walls becomes significant and, hence, cause it to deviate from the inverse $1/R^2$ law are indicated by vertical lines in the figures. This distance was estimated by finding the distance where the plot line starts to fluctuate beyond the error bands. However, some plots for low frequencies such as Figure 64 or Figure 65 do not show the $1/R^2$ trend, thus it is difficult to estimate the error band. Hence the lines indicating the wall effect are not plotted in those figures. The red lines indicate error band, and the absolute maximum deviation is defined as half of the width of an error band.

As we move the microphone farther from the source, reflection becomes significant for waves of low frequencies. On the other hand, if we keep the microphone close to the source, although we can achieve good signal to noise ratio and lower level of reflection, we run into the risk of measuring the near-field of the source. These two factors make it difficult for us to obtain data which follows inverse square law for low frequencies.

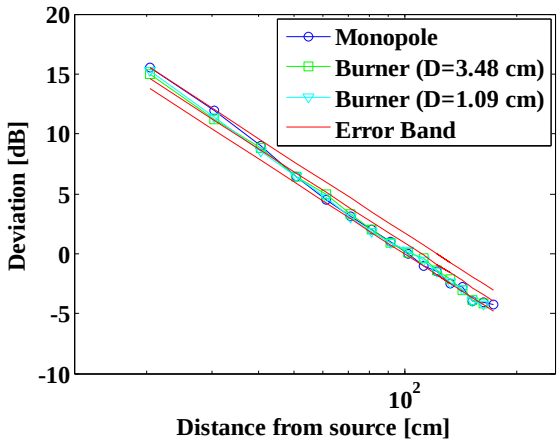

Figure 63 Deviation from reference sound pressure level versus distance from sound source. Data points taken for traverse A. Plot is for 100 Hz

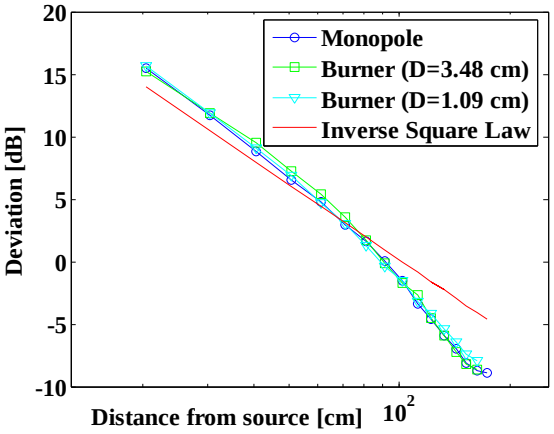

Figure 64 Deviation from reference sound pressure level versus distance from sound source. Data points taken for traverse A. Plot is for 125 Hz

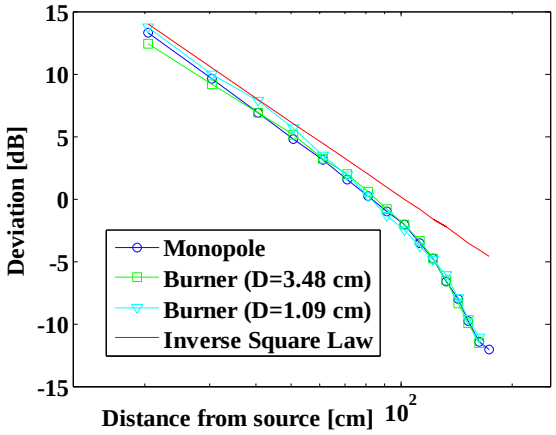

Figure 65 Deviation from reference sound pressure level versus distance from sound source. Data points taken for traverse A. Plot is for 160 Hz

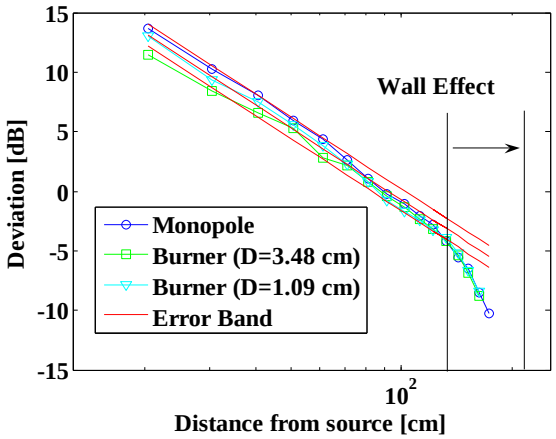

Figure 66 Deviation from reference sound pressure level versus distance from sound source. Data points taken for traverse A. Plot is for 200 Hz

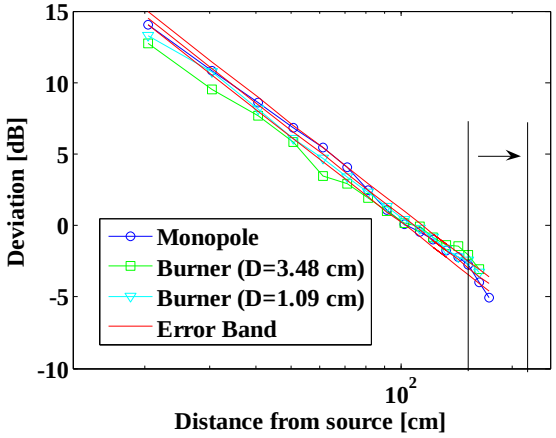

Figure 67 Deviation from reference sound pressure level versus distance from sound source. Data points taken for traverse A. Plot is for 250 Hz

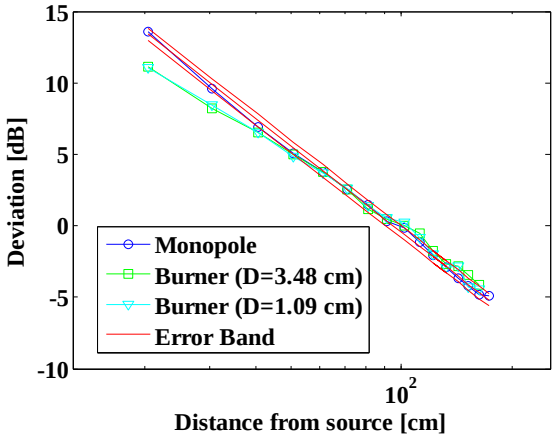

Figure 68 Deviation from reference sound pressure level versus distance from sound source. Data points taken for traverse A. Plot is for 1000 Hz

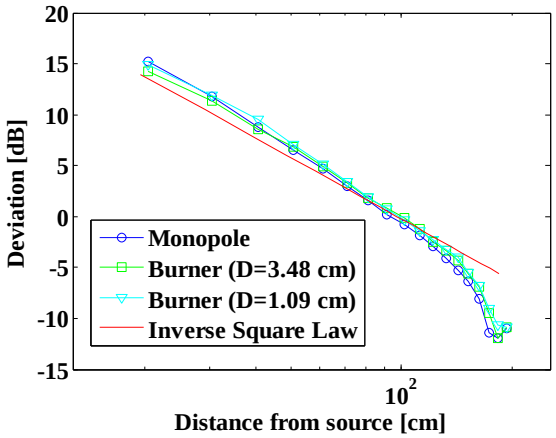

Figure 69 Deviation from reference sound pressure level versus distance from sound source. Data points taken for traverse B. Plot is for 100 Hz

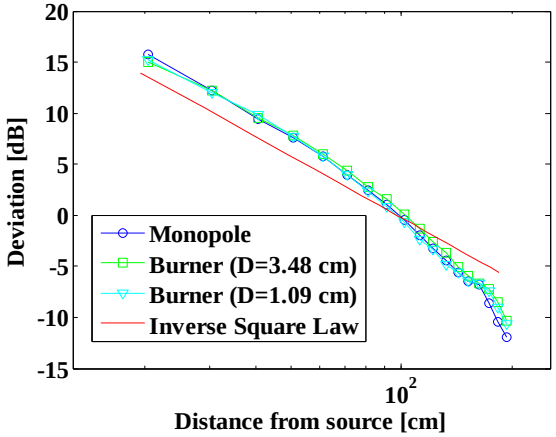

Figure 70 Deviation from reference sound pressure level versus distance from sound source. Data points taken for traverse B. Plot is for 125 Hz

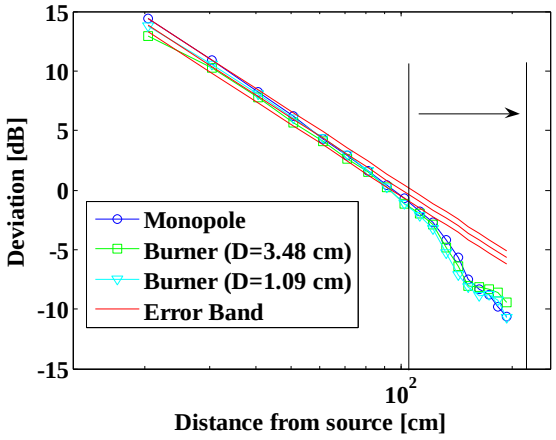

Figure 71 Deviation from reference sound pressure level versus distance from sound source. Data points taken for traverse B. Plot is for 160 Hz

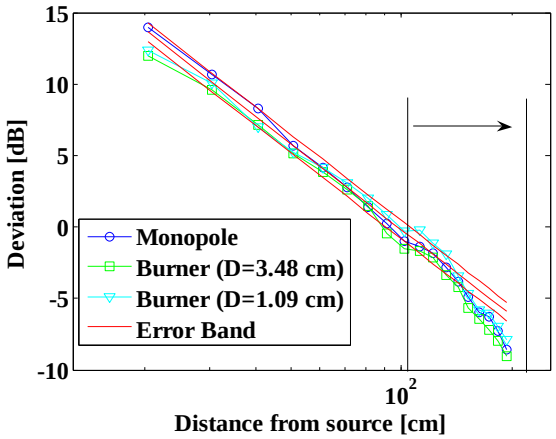

Figure 72 Deviation from reference sound pressure level versus distance from sound source. Data points taken for traverse B. Plot is for 200 Hz

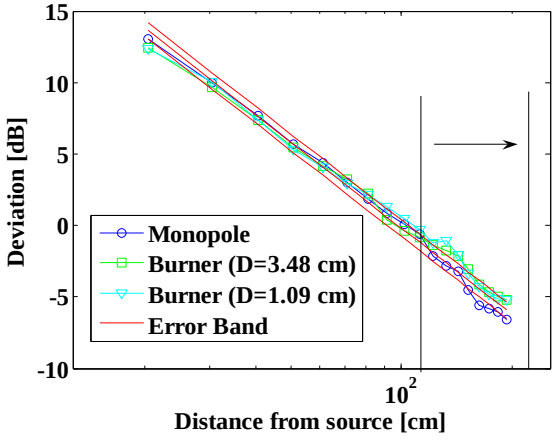

Figure 73 Deviation from reference sound pressure level versus distance from sound source. Data points taken for traverse B. Plot is for 250 Hz

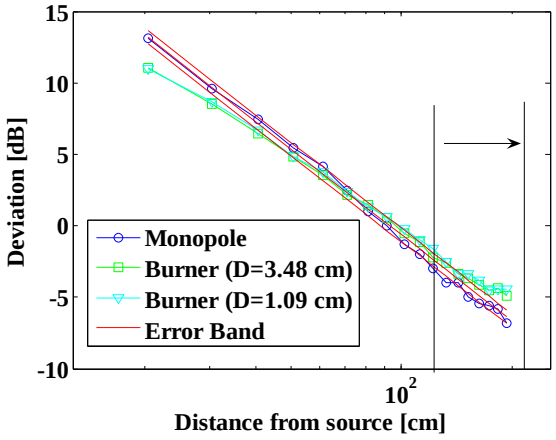

Figure 74 Deviation from reference sound pressure level versus distance from sound source. Data points taken for traverse B. Plot is for 1000 Hz

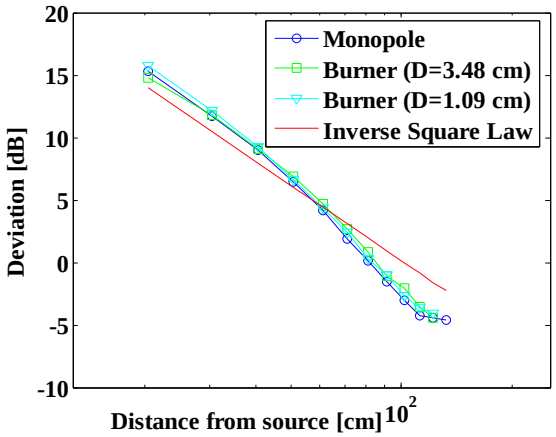

Figure 75 Deviation from reference sound pressure level versus distance from sound source. Data points taken for traverse C. Plot is for 100 Hz

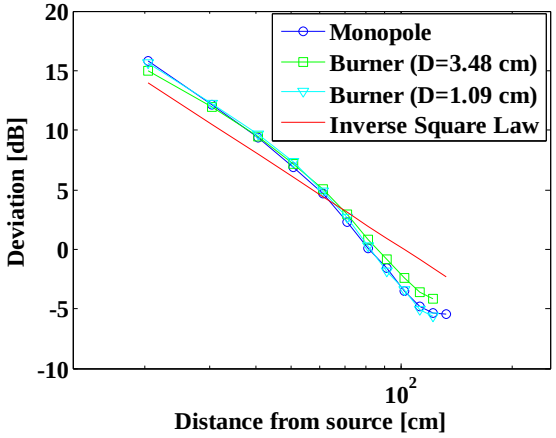

Figure 76 Deviation from reference sound pressure level versus distance from sound source. Data points taken for traverse C. Plot is for 125 Hz

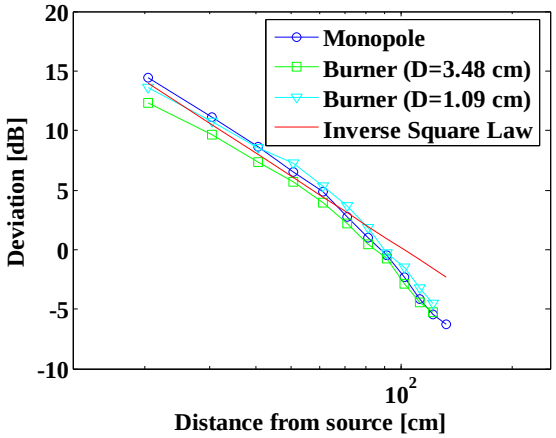

Figure 77 Deviation from reference sound pressure level versus distance from sound source. Data points taken for traverse C. Plot is for 160 Hz

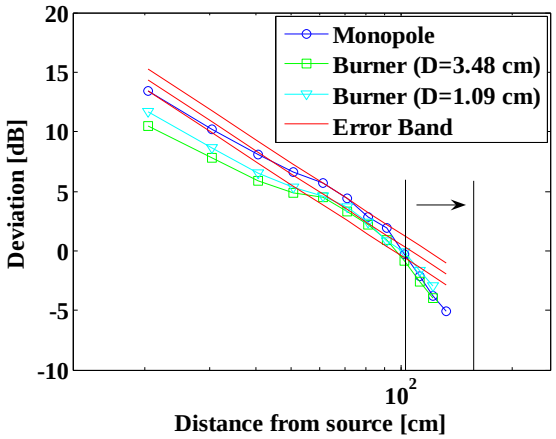

Figure 78 Deviation from reference sound pressure level versus distance from sound source. Data points taken for traverse C. Plot is for 200 Hz

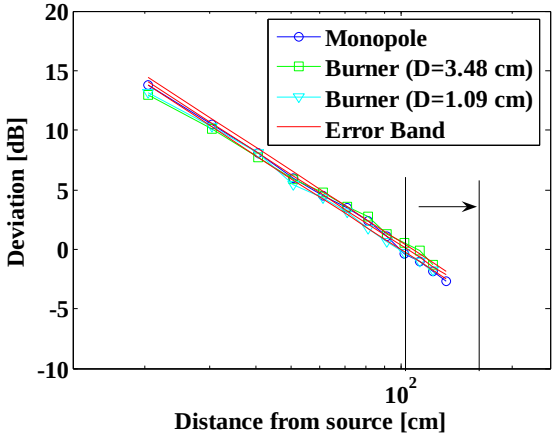

Figure 79 Deviation from reference sound pressure level versus distance from sound source. Data points taken for traverse C. Plot is for 250 Hz

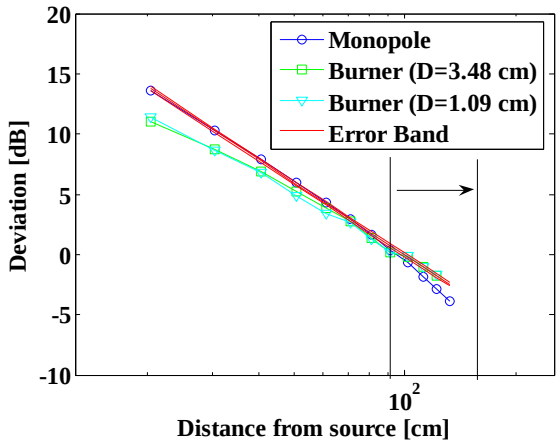

Figure 80 Deviation from reference sound pressure level versus distance from sound source. Data points taken for traverse C. Plot is for 1000 Hz

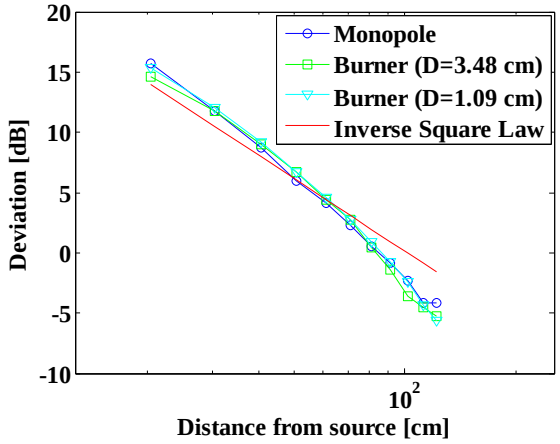

Figure 81 Deviation from reference sound pressure level versus distance from sound source. Data points taken for traverse D. Plot is for 100 Hz

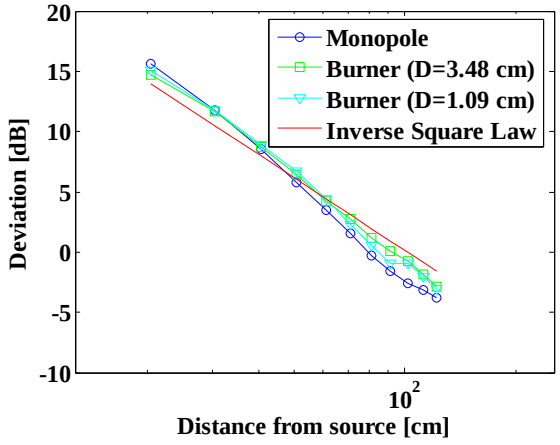

Figure 82 Deviation from reference sound pressure level versus distance from sound source. Data points taken for traverse D. Plot is for 125 Hz

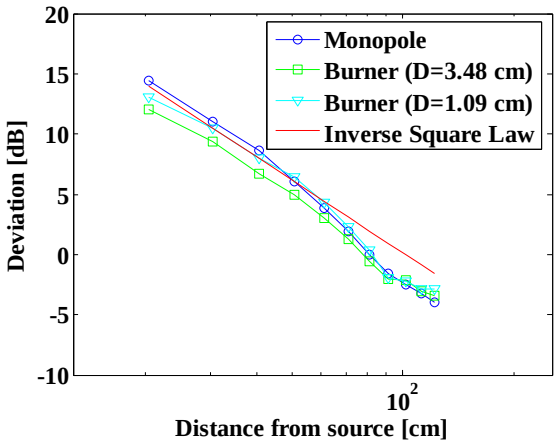

Figure 83 Deviation from reference sound pressure level versus distance from sound source. Data points taken for traverse D. Plot is for 160 Hz

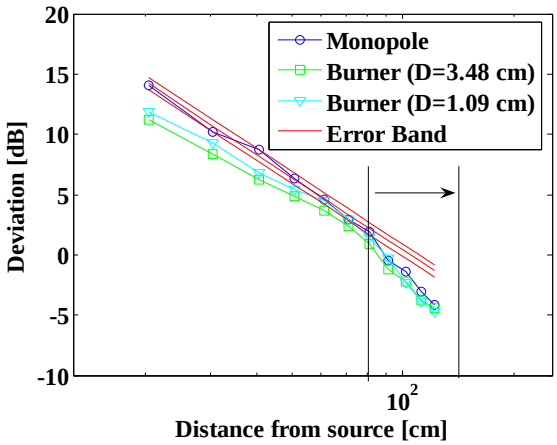

Figure 84 Deviation from reference sound pressure level versus distance from sound source. Data points taken for traverse D. Plot is for 200 Hz

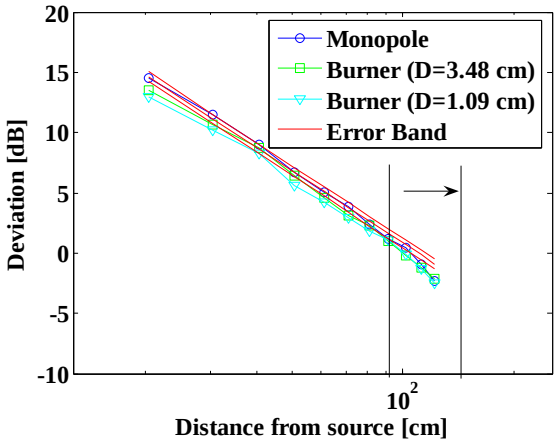

Figure 85 Deviation from reference sound pressure level versus distance from sound source. Data points taken for traverse D. Plot is for 250 Hz

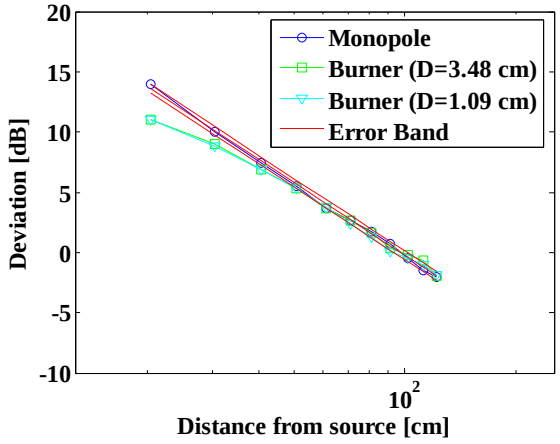

Figure 86 Deviation from reference sound pressure level versus distance from sound source. Data points taken for traverse D. Plot is for 1000 Hz

Observing the figures from Figure 63 to Figure 85, one can notice the plotted curves for burners are lower than that of a monopole sound source in the near-field, which indicates the microphone was not situated in a geometric far-field. A burner of larger diameter needs a larger distance to reach a geometric far-field.

It is also interesting to note that the plot for 100 Hz for the path A (Figure 63), unlike the trends in path B (Figure 69), the path C (Figure 75) and the path D (Figure 81), seems to follow inverse square law.

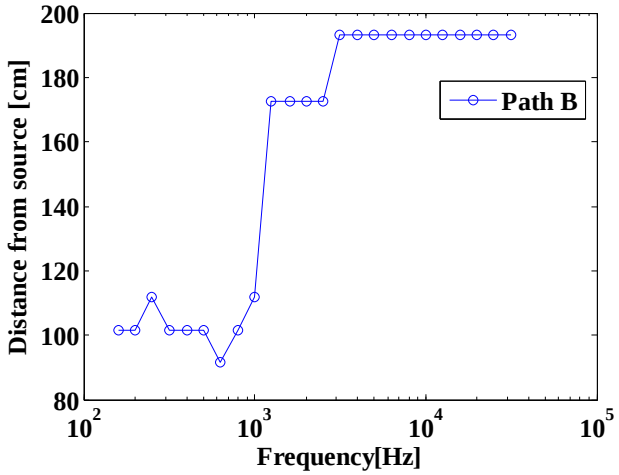

Figure 87 Distance from sound source when wall effect becomes significant for the path B versus frequency

Theoretically, the distance from the source where the effect of wall reflection becomes significant becomes longer as frequency increases, as shown in Figure 87. However, because of some uncertainties of data, such a tendency was not clearly observed for the data for the path A, C and D; these distances were estimated visually from figures and the test environments might have been slightly different in each measurement. The increasing curve is stopped at the distance of 193 cm because of the limitation of the room size; if the room size is larger, this line may continue to rise.

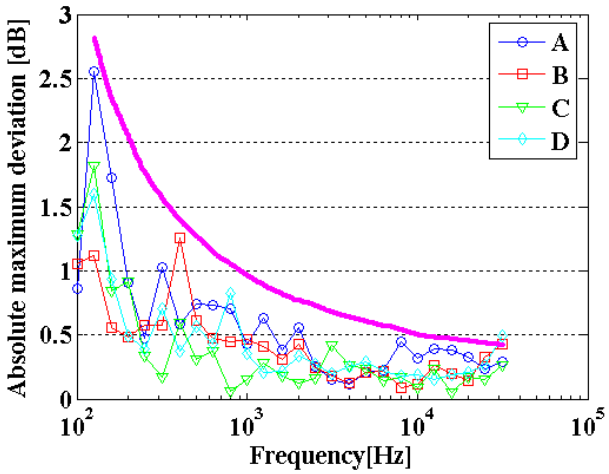

Figure 88 Frequency versus absolute maximum deviation from inverse square law (All the data points were used)

Figure 88 shows plots of frequency versus absolute maximum deviation from inverse square law for the data along the four paths. As stated earlier, it was difficult to determine error bands for low frequencies; however, we estimated error bands for low frequencies by measuring the deviation for the entire path.

Figure 89 shows similar plots for which only the data which were not much affected by background noises and wall reflections were used. Except for the last point of the path A, the other points follow the hand drawn curve as shown in the figure. It is reasonable that the absolute maximum deviation decreases with increasing frequency,

considering the property of anechoic wedges; the larger the frequency, the larger the absorption rate.

Absolute maximum deviations settle within 1dB above 400Hz for all the four paths and are attenuated down to 0.5 dB above 1250Hz. The maximum value of the deviation is 1.3 dB. This result indicates that our anechoic chamber can realize a free field environment properly.

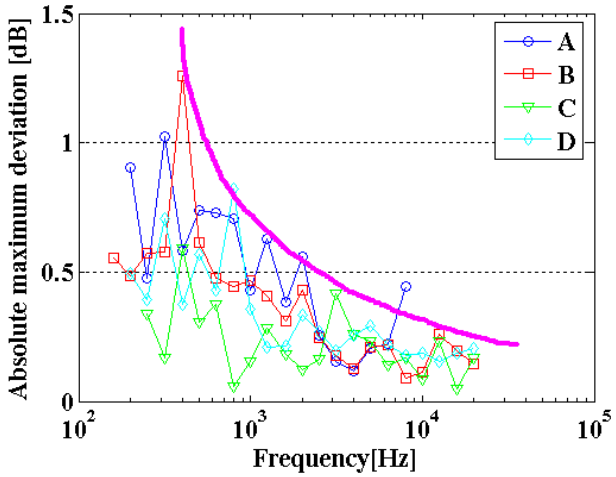

Figure 89 Frequency versus absolute maximum deviation from inverse square law (excludes error bands which were not justified were not used)

APPENDIX III: COHERENCE MEASUREMENTS AND SOURCE COMPACTNESS

In this appendix, the coherence function between two non-collinear measurements of sound from a distributed source is analyzed. Thereafter the validity to use the coherence function to estimate the frequency up to which this distribution is acoustically compact is being analyzed.

Let a set of infinitesimally small sources be distributed in a region defined by the circle of radius (l). The individual sources are random in nature. This means the autocorrelation for the individual correlation has the relationship:

$$\lim_{\tau \to \infty} R(\tau) = 0 \quad (35)$$

Let X and Y denote two measurement locations in the "far-field" of this distribution. The acoustic pressure felt at those two locations is compared – through coherence measurement - in this derivation. Figure 90 shows the schematic of the source distribution and its relationship with the locations of the measurement.

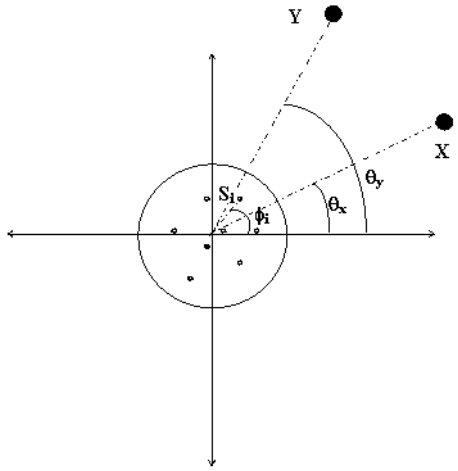

Figure 90 Schematic of a set of acoustic sources observed from two arbitrary non-collinear directions that are equidistant from the origin of sources

The coherence function is defined as:

$$\gamma_{xy}^2(\omega) = \frac{\left|P_{xy}(\omega)\right|^2}{P_{xx}(\omega)P_{yy}(\omega)} = \frac{\left|E\left(\hat{Y}(\omega)^* \hat{X}(\omega)\right)\right|^2}{E\left(\hat{X}(\omega)^* \hat{X}(\omega)\right)E\left(\hat{Y}(\omega)^* \hat{Y}(\omega)\right)} \quad (36)$$

where P_{xy} is the cross spectrum and P_{xx} and P_{yy} are the auto spectrum for the measurements made at X and Y. $\hat{X}$ and $\hat{Y}$ are the Fourier coefficients for the data taken at X and Y.

Simplifying Assumptions:

1. The individual source strengths $|S_i|^2$ equal
2. distances between X and Y from the origin are equal

The pressure perturbation felt at x is a superposition of the signals that were emanated from the individual sources.

$$X(t) = \sum \frac{S_i\left(t - R_{ix}/c\right)}{R_{ix}} \approx \frac{1}{R}\sum S_i\left(t - R_{ix}/c\right) \quad (37)$$

The Fourier transform of the time series is then:

$$\hat{X}(\omega) = \frac{1}{R}\sum \hat{S}_i(\omega) e^{\frac{-i\omega R_{ix}}{c}} \quad (38)$$

Using the far field approximation for the distance of the individual sources from X

$$R_{ix} \approx R - l_i \cos(\phi_i - \theta_x) \quad (39)$$

This leads for further simplification of Equation 36:

$$\hat{X}(\omega) = \frac{1}{R}\sum \hat{S}_i(\omega) e^{\frac{-i\omega R_{ix}}{c}} \approx \frac{e^{\frac{-i\omega R}{c}}}{R}\sum \hat{S}_i(\omega) e^{\frac{i\omega l_i \cos(\phi_i - \theta_x)}{c}} \quad (40)$$

For ease of derivation the terms that are common for the entire summation is dropped from the rest of the derivation. Thus we have:

$$\hat{X}(\omega) = \sum \hat{S}_i(\omega) e^{\frac{i\omega l_i \cos(\phi_i - \theta_x)}{c}} \text{ and } \hat{Y}(\omega) = \sum \hat{S}_i(\omega) e^{\frac{i\omega l_i \cos(\phi_i - \theta_y)}{c}} \quad (41)$$

Using the Fourier coefficients we can now calculate the cross spectrum:

$$\hat{Y}^*(\omega)\hat{X}(\omega) = \sum \hat{S}_i^*(\omega) e^{\frac{-i\omega l_i \cos(\phi_i - \theta_y)}{c}} \sum \hat{S}_i(\omega) e^{\frac{i\omega l_i \cos(\phi_i - \theta_x)}{c}} \quad (42)$$

which can be rewritten as:

$$\hat{Y}^*(\omega)\hat{X}(\omega) = \sum \hat{S}_i^*(\omega)\hat{S}_j(\omega) e^{\frac{i\omega\left(l_j \cos(\phi_j - \theta_x) - l_i \cos(\phi_i - \theta_y)\right)}{c}} \quad (43)$$

Thus the estimate of the cross spectrum is given by:

$$E\left(\hat{Y}^*(\omega)\hat{X}(\omega)\right) = E\left(\sum \hat{S}_i^*(\omega)\hat{S}_j(\omega) e^{\frac{i\omega\left(l_j \cos(\phi_j - \theta_x) - l_i \cos(\phi_i - \theta_y)\right)}{c}}\right) \quad (44)$$

However, the exponent is constant based on just geometry and will be the same for every realization of an ensemble for cross spectrum calculations

$$E\left(\hat{Y}^*(\omega)\hat{X}(\omega)\right) = \sum E\left(\hat{S}_i^*(\omega)\hat{S}_j(\omega)\right) e^{\frac{i\omega\left(l_j \cos(\phi_j - \theta_x) - l_i \cos(\phi_i - \theta_y)\right)}{c}} \quad (45)$$

The autospectrum can be estimated with the same procedure:

$$E\left(\hat{X}^*(\omega)\hat{X}(\omega)\right)=\sum E\left(\hat{S}_i^*(\omega)\hat{S}_j(\omega)\right)e^{\frac{i\omega\left(l_j\cos\left(\phi_j-\theta_x\right)-l_i\cos\left(\phi_i-\theta_x\right)\right)}{c}} \quad (46)$$

$$E\left(\hat{Y}^*(\omega)\hat{Y}(\omega)\right)=\sum E\left(\hat{S}_i^*(\omega)\hat{S}_j(\omega)\right)e^{\frac{i\omega\left(l_j\cos\left(\phi_j-\theta_y\right)-l_i\cos\left(\phi_i-\theta_y\right)\right)}{c}} \quad (47)$$

The coherence function between X and Y is now estimated for two different cases of source distribution:

1. the individual sources are completely independent of each other
2. the individual sources are coherent with each other

Case1: The individual sources are incoherent with each other.

This implies that the cross spectrum between the individual sources is zero for all frequencies:

$$E\left(\hat{S}_i^*(\omega)\hat{S}_j(\omega)\right)=0 \text{ for } i\neq j \quad (48)$$

This would reduce the terms in autospectral and cross spectral estimation to:

$$E\left(\hat{X}^*(\omega)\hat{X}(\omega)\right)=E\left(\hat{Y}^*(\omega)\hat{Y}(\omega)\right)=\sum E\left(\hat{S}_i^*(\omega)\hat{S}_i(\omega)\right) \quad (49)$$

$$\begin{aligned}E\left(\hat{Y}^*(\omega)\hat{X}(\omega)\right)&=\sum E\left(\hat{S}_i^*(\omega)\hat{S}_i(\omega)\right)e^{\frac{i\omega l_i\left(\cos\left(\phi_i-\theta_x\right)-\cos\left(\phi_i-\theta_y\right)\right)}{c}}\\&=\sum E\left(\hat{S}_i^*(\omega)\hat{S}_i(\omega)\right)e^{\frac{i2\omega l_i\sin\left(\frac{\theta_y-\theta_x}{2}\right)\sin\left(\phi_i-\frac{\theta_y+\theta_x}{2}\right)}{c}}\end{aligned} \quad (50)$$

Notation: $E\left(\hat{S}_i^*(\omega)\hat{S}_i(\omega)\right)=S^2$

Hence, if the number of individual sources is finite (=N), then the autospectrum will reduce to:

$$E\left(\hat{X}^*(\omega)\hat{X}(\omega)\right)=E\left(\hat{Y}^*(\omega)\hat{Y}(\omega)\right)=S^2N \quad (51)$$

Furthermore, the cross spectrum will reduce to:

$$E\left(\hat{Y}^*(\omega)\hat{X}(\omega)\right) = \sum S^2 e^{\frac{i2\omega l_i \sin\left(\frac{\theta_y-\theta_x}{2}\right)\sin\left(\phi_i-\frac{\theta_y+\theta_x}{2}\right)}{c}} = S^2 \sum e^{\frac{i2\omega l_i \sin\left(\frac{\theta_y-\theta_x}{2}\right)\sin\left(\phi_i-\frac{\theta_y+\theta_x}{2}\right)}{c}} \quad (52)$$

Having estimated the cross spectrum, we can now calculate the coherence function.

$$\begin{aligned}\left|E\left(\hat{Y}^*(\omega)\hat{X}(\omega)\right)\right|^2 &= \left(E\left(\hat{Y}^*(\omega)\hat{X}(\omega)\right)\right)^*\left(E\left(\hat{Y}^*(\omega)\hat{X}(\omega)\right)\right)\\ &= S^4\sum e^{\frac{-i2\omega l_i \sin\left(\frac{\theta_y-\theta_x}{2}\right)\sin\left(\phi_i-\frac{\theta_y+\theta_x}{2}\right)}{c}}\sum e^{\frac{i2\omega l_i \sin\left(\frac{\theta_y-\theta_x}{2}\right)\sin\left(\phi_i-\frac{\theta_y+\theta_x}{2}\right)}{c}}\\ &= S^4\sum e^{\frac{i2\omega\sin\left(\frac{\theta_y-\theta_x}{2}\right)\left(l_i sin\left(\phi_i-\frac{\theta_y+\theta_x}{2}\right)-l_j sin\left(\phi_j-\frac{\theta_y+\theta_x}{2}\right)\right)}{c}}\\ &= S^4N + S^4\sum_{i\neq j} e^{\frac{i2\omega\sin\left(\frac{\theta_y-\theta_x}{2}\right)\left(l_i sin\left(\phi_i-\frac{\theta_y+\theta_x}{2}\right)-l_j sin\left(\phi_j-\frac{\theta_y+\theta_x}{2}\right)\right)}{c}}\end{aligned} \quad (53)$$

When you start with N different sources, then the second term in the right hand side will have (N^2 - N) terms. It should be noted that $N^2 - N = N(N-1)$ which is always even. And hence the Equation 51 can be simplified to:

$$\begin{aligned}&S^4N + S^4\sum_{i\neq j} e^{\frac{i2\omega\sin\left(\frac{\theta_y-\theta_x}{2}\right)\left(l_i sin\left(\phi_i-\frac{\theta_y+\theta_x}{2}\right)-l_j sin\left(\phi_j-\frac{\theta_y+\theta_x}{2}\right)\right)}{c}}\\ &= S^4N + 2S^4\sum_{i<j}\cos\left(\frac{2\omega\sin\left(\frac{\theta_y-\theta_x}{2}\right)\left(l_i sin\left(\phi_i-\frac{\theta_y+\theta_x}{2}\right)-l_j sin\left(\phi_j-\frac{\theta_y+\theta_x}{2}\right)\right)}{c}\right)\end{aligned} \quad (54)$$

The second term in the RHS now will have N(N-1)/2 terms each can attain a maximum value of 1. Now that we have calculated the numerator term for coherence calculation, let us look at the denominator term. Based on Equation 49, the denominator should be simply:

$$E\left(\hat{X}^*(\omega)\hat{X}(\omega)\right)E\left(\hat{Y}^*(\omega)\hat{Y}(\omega)\right) = S^4N^2 \quad (55)$$

The coherence between the measurements at X and Y is given by the ratio of Equation 52 and Equation 53. As we can see that for the coherence value to be equal to 1, every one of the terms in the second part of the numerator (in Equation 52) should be equal to one. This could happen for two conditions:

1. the microphones are collinear ($\theta_x = \theta_y$) making coherence to be independent of ω
2. $\omega = 0$

Otherwise, as ω increases, the coherence will start to decrease. The term that would significantly contribute coherence dropping from 1 will be the one for which the expression inside the cosine, i.e. $\left(l_i sin\left(\phi_i - \frac{\theta_y + \theta_x}{2} \right) - l_j sin\left(\phi_j - \frac{\theta_y + \theta_x}{2} \right) \right)$ is the highest. The maximum value of this expression can assume is limited by *l* and it could be as high as 2*l*.

Thus it proves that for a distributed acoustic source, where the individual sources are independent of each other, the length scale of distribution alone will determine at what frequency that the coherence begins to roll off from 1. Coincidentally, it is the same *l* that would define the cutoff frequency up to which the distribution is acoustically compact. Hence finding a cutoff point based on coherence roll off is a good measure of the cutoff frequency for compactness described in textbooks.

It should also be noted that even though the coherence value starts dropping from 1 as we increase ω, the derivation does not rule out the possibility that the coherence value will rise again. However from a practical view-point, when you have a large number of sources spread randomly over the region, we cannot expect the value to ever rise back to 1 as it requires all the terms on the right hand side (of the numerator term) to

go to 1. Also at "high" frequencies, the RHS term will be extremely sensitive to small changes in the length scale term. Thus, at high frequencies, the second term (in the numerator) has a very high probability of achieving all the values between -1 and 1 irrespective of the distribution. Hence we can expect the coherence to die out at "high" frequencies. However the frequency at which the coherence completely dies out will be heavily influenced by the actual distribution of the sources whereas the frequency at which the coherence begins to drop is a much simpler function of the largest length scale of the distribution.

Case 2: All the individual sources are coherent with each other.

For a random source, this kind of relationship is possible only if the there is a linear relationship between any 2 source points, i.e.

$$S_2(t) = aS_1(t-\tau) + b \quad (56)$$

However since the S_i indicate the pressure perturbations only and they were assumed to be equal in strength:

$$b \equiv 0 \,\&\, a = \pm 1 \quad (57)$$

Thus we can relate every source with every other source by:

$$S_j(t) = \pm S_i(t-\tau_{ij}) \quad (58)$$

$$\hat{S}_j(\omega) = \hat{S}_i(\omega) e^{-i(2\pi\omega\tau_{ij} + n_{ij}\pi)} \text{ where } n_{ij} \text{ is either 0 or 1} \quad (59)$$

It should be noted that $\tau_{ij} = -\tau_{ji}$ and $\tau_{ij} + \tau_{jk} = \tau_{ik}$

Thus the cross spectrum term for this case should reduce to:

$$E\left(\hat{Y}^*(\omega)\hat{X}(\omega)\right) = E\left(\sum \hat{S}_i^*(\omega)\hat{S}_i(\omega) e^{\frac{i\omega\left(l_j\cos(\phi_j-\theta_x) - l_i\cos(\phi_i-\theta_y) - 2\pi c\tau_{ij}\right)}{c} - in_{ij}\pi}\right) \quad (60)$$

Using the same arguments and notation put forth for case1

$$E\left(\sum \hat{S}_i^*(\omega)\hat{S}_i(\omega)e^{\frac{i\omega\left(l_j\cos\left(\phi_j-\theta_x\right)-l_i\cos\left(\phi_i-\theta_y\right)-2\pi c\tau_{ij}\right)}{c}}\right)=S^2\sum e^{\frac{i\omega\left(l_j\cos\left(\phi_j-\theta_x\right)-l_i\cos\left(\phi_i-\theta_y\right)-2\pi c\tau_{ij}\right)}{c}-in_{ij}\pi} \quad (61)$$

Thus the numerator term for the coherence calculation can be given by

$$\text{Numerator}=S^4\sum e^{\frac{i\omega\left(\left(l_j\cos\left(\phi_j-\theta_x\right)-l_i\cos\left(\phi_i-\theta_y\right)-2\pi c\tau_{ij}\right)-\left(l_k\cos\left(\phi_k-\theta_x\right)-l_l\cos\left(\phi_l-\theta_y\right)-2\pi c\tau_{kl}\right)\right)}{c}-i\left(n_{ij}-n_{kl}\right)\pi} \quad (62)$$

The autospectral terms will reduce to

$$E\left(\hat{X}^*(\omega)\hat{X}(\omega)\right)=S^2\sum e^{\frac{i\omega\left(l_i\cos\left(\phi_i-\theta_x\right)-l_j\cos\left(\phi_j-\theta_x\right)-2\pi c\tau_{ij}\right)}{c}-in_{ij}\pi} \quad (63)$$

$$E\left(\hat{Y}^*(\omega)\hat{Y}(\omega)\right)=S^2\sum e^{\frac{i\omega\left(l_i\cos\left(\phi_i-\theta_y\right)-l_j\cos\left(\phi_j-\theta_y\right)-2\pi c\tau_{ij}\right)}{c}-in_{ij}\pi} \quad (64)$$

The denominator term will also reduce to

$$\text{Denomintor}=S^4\sum e^{\frac{i\omega\left(\left(l_j\cos\left(\phi_j-\theta_x\right)-l_i\cos\left(\phi_i-\theta_y\right)-2\pi c\tau_{ij}\right)-\left(l_k\cos\left(\phi_k-\theta_x\right)-l_l\cos\left(\phi_l-\theta_y\right)-2\pi c\tau_{kl}\right)\right)}{c}-i\left(n_{ij}-n_{kl}\right)\pi} \quad (65)$$

The numerator term (Equation 60) and the denominator term (Equation 63) are one and the same. Thus the coherence, between any 2 microphone locations, will be 1 at all frequencies irrespective of the size of the domain (as long as the measurement is in the far-field). Hence the coherence function is size independent when all the individual sources are coherent with each other. Then the traditional definition for compactness cannot be derived out of coherence relationships.

Thus after examining both the cases, we can conclude that coherence function between two different measurements is heavily influenced by the spatial coherence across the sources in the domain. Hence, the coherence function can be used to describe compactness only after it has been ensured that the sources are spatially incoherent with

each other. Furthermore the cutoff frequency for coherence roll off is also a function of the angle between the two measurements.

APPENDIX IV: OPERATING CONDITIONS

Diameter (mm)	U_{ave} (m/s)	Serial No.	Fuel	phi	u'/U_{ave} (%)	S_L (m/s)	F_{peak} (Hz)	OASPL (dB)	α	β
34.8	9.6	3481	Acetylene	0.71	8.5	1.06	249	85	2.83	0.00
34.8	9.6	3481	Acetylene	0.67	8.5	0.96	244	83	2.80	0.00
34.8	9.6	3481	Acetylene	0.63	8.5	0.86	225	82	2.67	0.00
34.8	9.6	3481	Acetylene	0.57	8.5	0.72	190	80	2.56	0.00
34.8	9.6	3481	Acetylene	0.52	8.5	0.57	161	76	2.39	0.00
34.8	8.6	3481	Acetylene	0.70	8.8	1.04	239	83	2.82	0.00
34.8	8.6	3481	Acetylene	0.66	8.8	0.94	225	82	2.76	0.00
34.8	8.6	3481	Acetylene	0.61	8.8	0.82	215	79	2.63	0.00
34.8	8.6	3481	Acetylene	0.55	8.8	0.66	156	76	2.42	0.00
34.8	7.5	3481	Acetylene	0.66	8.2	0.94	220	80	2.76	0.00
34.8	7.5	3481	Acetylene	0.61	8.2	0.81	186	77	2.58	0.00
34.8	7.5	3481	Acetylene	0.55	8.2	0.67	166	74	2.40	0.00
34.8	6.4	3481	Acetylene	0.64	8.3	0.90	200	77	2.68	0.00
34.8	6.4	3481	Acetylene	0.58	8.3	0.74	176	74	2.50	0.00
34.8	5.4	3481	Acetylene	0.62	8.3	0.85	190	74	2.66	0.00
34.8	5.4	3481	Acetylene	0.57	8.3	0.72	142	71	2.43	0.00
34.8	9.6	3482	Acetylene	0.71	9.4	1.06	249	84	2.78	0.00
34.8	9.6	3482	Acetylene	0.67	9.4	0.96	229	83	2.73	0.00
34.8	9.6	3482	Acetylene	0.63	9.4	0.86	215	81	2.63	0.00
34.8	9.6	3482	Acetylene	0.57	9.4	0.72	190	79	2.50	0.00
34.8	8.6	3482	Acetylene	0.70	8.6	1.04	239	83	2.86	0.00
34.8	8.6	3482	Acetylene	0.66	8.6	0.94	229	81	2.76	0.00
34.8	8.6	3482	Acetylene	0.61	8.6	0.82	200	80	2.64	0.00
34.8	8.6	3482	Acetylene	0.55	8.6	0.66	166	76	2.43	0.00
34.8	7.5	3482	Acetylene	0.66	8.5	0.95	229	80	2.78	0.00
34.8	7.5	3482	Acetylene	0.61	8.5	0.81	190	78	2.58	0.00
34.8	7.5	3482	Acetylene	0.56	8.5	0.68	166	74	2.39	0.00
34.8	6.4	3482	Acetylene	0.65	8.5	0.91	205	77	2.72	0.00
34.8	6.4	3482	Acetylene	0.59	8.5	0.75	176	75	2.54	0.00
34.8	5.4	3482	Acetylene	0.63	8.0	0.86	200	75	2.69	0.00
34.8	5.4	3482	Acetylene	0.58	8.0	0.73	161	72	2.50	0.00
34.8	8.6	3483	Acetylene	0.50	12.5	0.53	142	73	2.37	0.00
34.8	9.6	3481	Propane	1.06	8.5	0.55	146	80	2.27	0.00
34.8	9.6	3481	Propane	1.01	8.5	0.55	132	79	2.26	0.00
34.8	9.6	3481	Propane	0.95	8.5	0.52	112	78	2.22	0.00
34.8	9.6	3481	Propane	0.91	8.5	0.50	103	76	2.18	0.00
34.8	8.6	3481	Propane	1.02	8.8	0.55	142	78	2.22	0.00
34.8	8.6	3481	Propane	0.95	8.8	0.52	117	77	2.21	0.00
34.8	7.5	3481	Propane	1.02	8.2	0.55	127	76	2.26	0.00
34.8	7.5	3481	Propane	0.97	8.2	0.53	107	75	2.20	0.00
34.8	6.4	3481	Propane	1.03	8.3	0.55	142	76	2.34	0.00
34.8	6.4	3481	Propane	0.96	8.3	0.53	107	73	2.24	0.00
34.8	5.4	3481	Propane	1.03	8.3	0.55	146	74	2.38	0.00
34.8	9.6	3482	Propane	1.06	9.4	0.55	151	81	2.29	0.00

34.8	9.6	3482	Propane	1.01	9.4	0.55	137	80	2.24	0.00
34.8	9.6	3482	Propane	0.95	9.4	0.52	117	77	2.21	0.00
34.8	8.6	3482	Propane	1.02	8.6	0.55	146	79	2.35	0.00
34.8	8.6	3482	Propane	0.95	8.6	0.52	117	77	2.27	0.00
34.8	7.5	3482	Propane	1.02	8.5	0.55	142	78	2.37	0.00
34.8	7.5	3482	Propane	0.97	8.5	0.53	122	76	2.31	0.00
34.8	7.5	3482	Propane	0.91	8.5	0.50	112	75	2.26	0.00
34.8	6.4	3482	Propane	1.03	8.5	0.55	137	76	2.40	0.00
34.8	6.4	3482	Propane	0.96	8.5	0.53	112	74	2.33	0.00
34.8	5.4	3482	Propane	1.03	8.0	0.55	137	74	2.46	0.00
34.8	9.6	3483	Propane	1.06	12.5	0.55	151	81	2.32	0.00
34.8	9.6	3483	Propane	1.01	12.5	0.55	142	80	2.31	0.00
34.8	9.6	3483	Propane	0.95	12.5	0.52	112	78	2.23	0.00
34.8	9.6	3483	Propane	0.91	12.5	0.50	107	77	2.20	0.00
34.8	8.6	3483	Propane	1.02	12.5	0.55	142	79	2.29	0.00
34.8	8.6	3483	Propane	0.95	12.5	0.52	112	77	2.23	0.00
34.8	7.5	3483	Propane	1.02	12.6	0.55	137	77	2.32	0.00
34.8	7.5	3483	Propane	0.97	12.6	0.53	117	76	2.29	0.00
34.8	7.5	3483	Propane	0.91	12.6	0.50	107	75	2.28	0.00
34.8	6.4	3483	Propane	1.03	12.8	0.55	137	76	2.37	0.00
34.8	6.4	3483	Propane	0.96	12.8	0.53	122	74	2.33	0.00
34.8	5.4	3483	Propane	1.03	12.4	0.55	146	74	2.38	0.00
34.8	5.4	3483	Propane	0.96	12.4	0.53	137	73	2.34	0.00
34.8	9.6	3481	Natural Gas	1.00	8.5	0.40	142	77	2.53	0.00
34.8	8.6	3481	Natural Gas	1.02	8.8	0.40	132	77	2.55	0.00
34.8	6.4	3481	Natural Gas	1.02	8.3	0.40	122	74	2.59	0.00
34.8	5.4	3481	Natural Gas	1.04	8.3	0.40	107	72	2.62	0.00
34.8	9.6	3482	Natural Gas	0.95	9.4	0.38	132	77	2.54	0.00
34.8	8.6	3482	Natural Gas	1.02	8.6	0.40	146	78	2.59	0.00
34.8	7.5	3482	Natural Gas	1.01	8.5	0.40	137	76	2.61	0.00
34.8	6.4	3482	Natural Gas	1.02	8.5	0.40	146	75	2.65	0.00
34.8	9.6	3483	Natural Gas	1.00	12.5	0.40	142	78	2.55	0.00
34.8	8.6	3483	Natural Gas	1.02	12.5	0.40	132	78	2.59	0.00
34.8	7.5	3483	Natural Gas	1.01	12.6	0.40	132	76	2.62	0.00
34.8	6.4	3483	Natural Gas	1.02	12.8	0.40	132	74	2.68	0.00
34.8	5.4	3483	Natural Gas	1.04	12.4	0.40	122	73	2.68	0.00
34.8	5.4	3483	Natural Gas	0.98	12.4	0.39	103	72	2.68	0.00
17.3	26.1	1731	Acetylene	0.72	2.3	1.07	405	86	3.00	0.00
17.3	26.1	1731	Acetylene	0.68	2.3	0.98	396	85	2.92	0.00
17.3	26.1	1731	Acetylene	0.63	2.3	0.88	366	84	2.86	0.00
17.3	26.1	1731	Acetylene	0.59	2.3	0.77	332	83	2.81	0.00
17.3	26.1	1731	Acetylene	0.55	2.3	0.66	288	81	2.69	0.00
17.3	26.1	1731	Acetylene	0.51	2.3	0.55	254	79	2.56	0.00
17.3	26.1	1731	Acetylene	0.47	2.3	0.44	215	77	2.54	0.00
17.3	26.1	1731	Acetylene	0.43	2.3	0.33	151	73	2.74	0.00
17.3	21.8	1731	Acetylene	0.64	2.3	0.88	347	82	2.94	0.00
17.3	21.8	1731	Acetylene	0.59	2.3	0.75	332	81	2.83	0.00
17.3	21.8	1731	Acetylene	0.54	2.3	0.62	264	79	2.68	0.00
17.3	21.8	1731	Acetylene	0.49	2.3	0.48	225	76	2.53	0.00

17.3	21.8	1731	Acetylene	0.44	2.3	0.36	171	72	2.54	0.00
17.3	17.4	1731	Acetylene	0.58	2.4	0.73	303	78	2.88	0.00
17.3	17.4	1731	Acetylene	0.51	2.4	0.56	244	76	2.66	0.00
17.3	17.4	1731	Acetylene	0.45	2.4	0.39	181	71	2.45	0.00
17.3	13.1	1731	Acetylene	0.56	2.4	0.68	269	74	2.88	0.00
17.3	13.1	1731	Acetylene	0.51	2.4	0.56	229	72	2.68	0.00
17.3	13.1	1731	Acetylene	0.47	2.4	0.45	205	70	2.55	0.00
17.3	13.1	1731	Acetylene	0.43	2.4	0.34	156	67	2.38	0.00
17.3	8.7	1731	Acetylene	0.58	2.3	0.73	278	71	3.11	0.00
17.3	8.7	1731	Acetylene	0.52	2.3	0.57	200	67	2.74	0.00
17.3	8.7	1731	Acetylene	0.45	2.3	0.40	156	64	2.42	0.00
17.3	21.8	1732	Acetylene	0.51	9.2	0.55	327	82	2.67	0.00
17.3	21.8	1732	Acetylene	0.46	9.2	0.42	259	78	2.57	0.00
17.3	17.4	1732	Acetylene	0.51	9.6	0.56	322	80	2.69	0.00
17.3	17.4	1732	Acetylene	0.48	9.6	0.47	273	78	2.58	0.00
17.3	17.4	1732	Acetylene	0.45	9.6	0.39	239	75	2.51	0.00
17.3	13.1	1732	Acetylene	0.52	10.0	0.57	273	76	2.67	0.00
17.3	13.1	1732	Acetylene	0.47	10.0	0.45	229	73	2.50	0.00
17.3	13.1	1732	Acetylene	0.43	10.0	0.34	181	69	2.49	0.00
17.3	8.7	1732	Acetylene	0.52	12.6	0.57	249	72	2.71	0.00
17.3	8.7	1732	Acetylene	0.45	12.6	0.40	200	68	2.49	0.00
17.3	26.1	1733	Acetylene	0.59	4.7	0.77	361	84	2.89	0.00
17.3	26.1	1733	Acetylene	0.55	4.7	0.66	327	82	2.79	0.00
17.3	26.1	1733	Acetylene	0.51	4.7	0.55	278	81	2.68	0.00
17.3	26.1	1733	Acetylene	0.47	4.7	0.44	225	78	2.56	0.00
17.3	26.1	1733	Acetylene	0.43	4.7	0.33	161	74	2.67	0.00
17.3	21.8	1733	Acetylene	0.59	4.8	0.75	347	82	2.94	0.00
17.3	21.8	1733	Acetylene	0.54	4.8	0.62	303	80	2.78	0.00
17.3	21.8	1733	Acetylene	0.49	4.8	0.48	254	77	2.59	0.00
17.3	21.8	1733	Acetylene	0.44	4.8	0.36	200	74	2.54	0.00
17.3	17.4	1733	Acetylene	0.58	5.3	0.73	332	79	2.97	0.00
17.3	17.4	1733	Acetylene	0.51	5.3	0.56	269	76	2.75	0.00
17.3	17.4	1733	Acetylene	0.45	5.3	0.39	205	73	2.51	0.00
17.3	13.1	1733	Acetylene	0.60	5.6	0.78	317	77	3.07	0.00
17.3	13.1	1733	Acetylene	0.56	5.6	0.68	298	75	2.95	0.00
17.3	13.1	1733	Acetylene	0.51	5.6	0.56	249	73	2.76	0.00
17.3	13.1	1733	Acetylene	0.47	5.6	0.45	210	70	2.55	0.00
17.3	13.1	1733	Acetylene	0.43	5.6	0.34	156	66	2.43	0.00
17.3	8.7	1733	Acetylene	0.58	4.1	0.73	264	71	2.98	0.00
17.3	8.7	1733	Acetylene	0.52	4.1	0.57	220	69	2.77	0.00
17.3	8.7	1733	Acetylene	0.45	4.1	0.40	186	66	2.55	0.00
17.3	26.1	1734	Acetylene	0.59	3.3	0.77	356	83	2.84	0.00
17.3	26.1	1734	Acetylene	0.55	3.3	0.66	303	82	2.74	0.00
17.3	26.1	1734	Acetylene	0.51	3.3	0.55	273	80	2.63	0.00
17.3	26.1	1734	Acetylene	0.47	3.3	0.44	225	77	2.55	0.00
17.3	26.1	1734	Acetylene	0.43	3.3	0.33	142	73	2.72	0.00
17.3	21.8	1734	Acetylene	0.59	3.2	0.75	347	82	2.90	0.00
17.3	21.8	1734	Acetylene	0.54	3.2	0.62	283	79	2.72	0.00
17.3	21.8	1734	Acetylene	0.49	3.2	0.48	244	77	2.55	0.00

17.3	21.8	1734	Acetylene	0.44	3.2	0.36	190	73	2.54	0.00
17.3	17.4	1734	Acetylene	0.58	3.2	0.73	317	79	2.92	0.00
17.3	17.4	1734	Acetylene	0.51	3.2	0.56	254	76	2.68	0.00
17.3	17.4	1734	Acetylene	0.45	3.2	0.39	205	72	2.50	0.00
17.3	13.1	1734	Acetylene	0.60	3.1	0.78	308	76	3.00	0.00
17.3	13.1	1734	Acetylene	0.56	3.1	0.68	283	75	2.91	0.00
17.3	13.1	1734	Acetylene	0.51	3.1	0.56	249	73	2.75	0.00
17.3	13.1	1734	Acetylene	0.47	3.1	0.45	205	70	2.52	0.00
17.3	13.1	1734	Acetylene	0.43	3.1	0.34	161	67	2.41	0.00
17.3	8.7	1734	Acetylene	0.58	2.9	0.73	264	71	2.93	0.00
17.3	8.7	1734	Acetylene	0.52	2.9	0.57	215	68	2.73	0.00
17.3	8.7	1734	Acetylene	0.45	2.9	0.40	166	64	2.43	0.00
17.3	26.1	1731	Propane	1.01	2.3	0.55	205	81	2.34	0.00
17.3	26.1	1731	Propane	0.95	2.3	0.52	181	81	2.35	0.00
17.3	26.1	1731	Propane	0.89	2.3	0.49	146	80	2.31	0.00
17.3	21.8	1731	Propane	1.02	2.3	0.55	220	80	2.45	0.00
17.3	21.8	1731	Propane	0.95	2.3	0.52	210	79	2.40	0.00
17.3	21.8	1731	Propane	0.87	2.3	0.47	195	77	2.37	0.00
17.3	21.8	1731	Propane	0.79	2.3	0.41	137	75	2.40	0.00
17.3	17.4	1731	Propane	1.03	2.4	0.55	225	78	2.54	0.00
17.3	17.4	1731	Propane	0.94	2.4	0.52	200	77	2.47	0.00
17.3	17.4	1731	Propane	0.84	2.4	0.45	176	75	2.38	0.00
17.3	17.4	1731	Propane	0.75	2.4	0.37	151	72	2.37	0.00
17.3	13.1	1731	Propane	1.05	2.4	0.55	210	76	2.62	0.00
17.3	13.1	1731	Propane	0.99	2.4	0.54	200	75	2.54	0.00
17.3	13.1	1731	Propane	0.92	2.4	0.51	200	75	2.53	0.00
17.3	13.1	1731	Propane	0.86	2.4	0.47	186	73	2.46	0.00
17.3	13.1	1731	Propane	0.80	2.4	0.41	171	72	2.44	0.00
17.3	13.1	1731	Propane	0.73	2.4	0.35	142	69	2.37	0.00
17.3	8.7	1731	Propane	1.09	2.3	0.55	200	72	2.76	0.00
17.3	8.7	1731	Propane	0.99	2.3	0.54	195	71	2.65	0.00
17.3	8.7	1731	Propane	0.89	2.3	0.49	181	69	2.53	0.00
17.3	8.7	1731	Propane	0.80	2.3	0.41	151	67	2.47	0.00
17.3	8.7	1731	Propane	0.70	2.3	0.32	112	64	2.41	0.00
17.3	17.4	1732	Propane	1.03	11.5	0.55	303	83	2.59	0.00
17.3	17.4	1732	Propane	0.94	11.5	0.52	283	82	2.53	0.00
17.3	17.4	1732	Propane	0.84	11.5	0.45	225	79	2.45	0.00
17.3	17.4	1732	Propane	0.75	11.5	0.37	151	73	2.37	0.00
17.3	13.1	1732	Propane	1.05	12.8	0.55	269	79	2.67	0.00
17.3	13.1	1732	Propane	0.99	12.8	0.54	259	78	2.58	0.00
17.3	13.1	1732	Propane	0.92	12.8	0.51	249	77	2.56	0.00
17.3	13.1	1732	Propane	0.86	12.8	0.47	220	76	2.51	0.00
17.3	13.1	1732	Propane	0.80	12.8	0.41	205	75	2.49	0.00
17.3	13.1	1732	Propane	0.73	12.8	0.35	166	71	2.40	0.00
17.3	8.7	1732	Propane	1.09	15.0	0.55	229	75	2.71	0.00
17.3	8.7	1732	Propane	0.99	15.0	0.54	225	74	2.61	0.00
17.3	8.7	1732	Propane	0.89	15.0	0.49	210	72	2.57	0.00
17.3	8.7	1732	Propane	0.80	15.0	0.41	181	70	2.54	0.00
17.3	8.7	1732	Propane	0.70	15.0	0.32	151	67	2.46	0.00

17.3	8.7	1732	Propane	0.61	15.0	0.22	103	63	2.34	0.00
17.3	26.1	1733	Propane	1.01	4.7	0.55	205	82	2.34	0.00
17.3	26.1	1733	Propane	0.95	4.7	0.52	181	81	2.29	0.00
17.3	21.8	1733	Propane	1.02	4.8	0.55	244	80	2.50	0.00
17.3	21.8	1733	Propane	0.95	4.8	0.52	225	79	2.44	0.00
17.3	21.8	1733	Propane	0.87	4.8	0.47	200	78	2.38	0.00
17.3	17.4	1733	Propane	1.03	5.3	0.55	234	78	2.60	0.00
17.3	17.4	1733	Propane	0.94	5.3	0.52	225	77	2.50	0.00
17.3	17.4	1733	Propane	0.84	5.3	0.45	190	75	2.45	0.00
17.3	17.4	1733	Propane	0.75	5.3	0.37	161	72	2.39	0.00
17.3	13.1	1733	Propane	1.05	5.6	0.55	225	76	2.70	0.00
17.3	13.1	1733	Propane	0.99	5.6	0.54	225	75	2.65	0.00
17.3	13.1	1733	Propane	0.92	5.6	0.51	210	74	2.61	0.00
17.3	13.1	1733	Propane	0.86	5.6	0.47	205	74	2.58	0.00
17.3	13.1	1733	Propane	0.80	5.6	0.41	176	72	2.50	0.00
17.3	13.1	1733	Propane	0.73	5.6	0.35	156	70	2.45	0.00
17.3	13.1	1733	Propane	0.67	5.6	0.29	122	67	2.37	0.00
17.3	8.7	1733	Propane	1.09	4.1	0.55	210	72	2.81	0.00
17.3	8.7	1733	Propane	0.99	4.1	0.54	205	71	2.73	0.00
17.3	8.7	1733	Propane	0.89	4.1	0.49	186	70	2.63	0.00
17.3	8.7	1733	Propane	0.80	4.1	0.41	171	68	2.59	0.00
17.3	8.7	1733	Propane	0.70	4.1	0.32	132	65	2.50	0.00
17.3	26.1	1734	Propane	1.01	3.3	0.55	210	82	2.33	0.00
17.3	26.1	1734	Propane	0.95	3.3	0.52	195	81	2.32	0.00
17.3	26.1	1734	Propane	0.89	3.3	0.49	151	79	2.30	0.00
17.3	21.8	1734	Propane	1.02	3.2	0.55	239	80	2.45	0.00
17.3	21.8	1734	Propane	0.95	3.2	0.52	225	79	2.41	0.00
17.3	21.8	1734	Propane	0.87	3.2	0.47	190	78	2.39	0.00
17.3	21.8	1734	Propane	0.79	3.2	0.41	142	75	2.33	0.00
17.3	17.4	1734	Propane	1.03	3.2	0.55	234	78	2.59	0.00
17.3	17.4	1734	Propane	0.94	3.2	0.52	215	77	2.49	0.00
17.3	17.4	1734	Propane	0.84	3.2	0.45	190	75	2.40	0.00
17.3	17.4	1734	Propane	0.75	3.2	0.37	156	72	2.34	0.00
17.3	13.1	1734	Propane	1.05	3.1	0.55	220	75	2.70	0.00
17.3	13.1	1734	Propane	0.99	3.1	0.54	220	75	2.62	0.00
17.3	13.1	1734	Propane	0.92	3.1	0.51	210	74	2.57	0.00
17.3	13.1	1734	Propane	0.86	3.1	0.47	190	73	2.51	0.00
17.3	13.1	1734	Propane	0.80	3.1	0.41	176	72	2.46	0.00
17.3	13.1	1734	Propane	0.73	3.1	0.35	156	69	2.40	0.00
17.3	8.7	1734	Propane	1.09	2.9	0.55	210	72	2.86	0.00
17.3	8.7	1734	Propane	0.99	2.9	0.54	210	71	2.72	0.00
17.3	8.7	1734	Propane	0.89	2.9	0.49	186	70	2.61	0.00
17.3	8.7	1734	Propane	0.80	2.9	0.41	171	68	2.55	0.00
17.3	8.7	1734	Propane	0.70	2.9	0.32	132	65	2.48	0.00
17.3	21.8	1731	Natural Gas	1.03	2.8	0.40	215	78	2.64	0.00
17.3	21.8	1731	Natural Gas	0.95	2.8	0.38	195	77	2.68	0.00
17.3	21.8	1731	Natural Gas	0.90	2.8	0.35	176	75	2.73	0.00
17.3	17.4	1731	Natural Gas	1.02	2.9	0.40	210	76	2.67	0.00
17.3	17.4	1731	Natural Gas	0.95	2.9	0.38	190	75	2.71	0.00

17.3	17.4	1731	Natural Gas	0.88	2.9	0.34	181	75	2.69	0.00
17.3	17.4	1731	Natural Gas	0.82	2.9	0.29	161	72	2.72	0.00
17.3	13.1	1731	Natural Gas	0.95	3.2	0.38	171	73	2.75	0.00
17.3	13.1	1731	Natural Gas	0.91	3.2	0.36	161	72	2.75	0.00
17.3	13.1	1731	Natural Gas	0.86	3.2	0.33	156	71	2.73	0.00
17.3	13.1	1731	Natural Gas	0.82	3.2	0.30	142	69	2.74	0.00
17.3	17.4	1732	Natural Gas	1.02	11.5	0.40	254	80	2.75	0.00
17.3	17.4	1732	Natural Gas	0.95	11.5	0.38	254	79	2.76	0.00
17.3	17.4	1732	Natural Gas	0.88	11.5	0.34	229	77	2.77	0.00
17.3	17.4	1732	Natural Gas	0.82	11.5	0.29	181	75	2.76	0.00
17.3	13.1	1732	Natural Gas	1.04	12.8	0.40	239	77	2.77	0.00
17.3	13.1	1732	Natural Gas	0.95	12.8	0.38	239	76	2.79	0.00
17.3	13.1	1732	Natural Gas	0.90	12.8	0.36	229	75	2.79	0.00
17.3	13.1	1732	Natural Gas	0.86	12.8	0.33	210	74	2.79	0.00
17.3	13.1	1732	Natural Gas	0.82	12.8	0.29	195	72	2.79	0.00
17.3	8.7	1732	Natural Gas	0.88	15.0	0.34	190	70	2.82	0.00
17.3	8.7	1732	Natural Gas	0.82	15.0	0.29	161	67	2.75	0.00
17.3	21.8	1733	Natural Gas	1.03	5.6	0.40	215	79	2.68	0.00
17.3	21.8	1733	Natural Gas	0.95	5.6	0.38	205	78	2.70	0.00
17.3	17.4	1733	Natural Gas	1.02	6.0	0.40	220	76	2.73	0.00
17.3	17.4	1733	Natural Gas	0.95	6.0	0.38	205	75	2.77	0.00
17.3	17.4	1733	Natural Gas	0.88	6.0	0.34	186	74	2.75	0.00
17.3	17.4	1733	Natural Gas	0.82	6.0	0.29	166	72	2.76	0.00
17.3	13.1	1733	Natural Gas	0.95	7.0	0.38	200	74	2.81	0.00
17.3	13.1	1733	Natural Gas	0.90	7.0	0.36	195	73	2.81	0.00
17.3	13.1	1733	Natural Gas	0.86	7.0	0.33	181	71	2.79	0.00
17.3	13.1	1733	Natural Gas	0.82	7.0	0.29	161	69	2.78	0.00
17.3	8.7	1733	Natural Gas	0.88	8.5	0.34	156	67	2.85	0.00
17.3	21.8	1734	Natural Gas	1.03	3.9	0.40	215	79	2.65	0.00
17.3	21.8	1734	Natural Gas	0.95	3.9	0.38	200	77	2.70	0.00
17.3	21.8	1734	Natural Gas	0.84	3.9	0.31	137	74	2.76	0.00
17.3	17.4	1734	Natural Gas	1.02	4.0	0.40	220	76	2.70	0.00
17.3	17.4	1734	Natural Gas	0.95	4.0	0.38	205	75	2.72	0.00
17.3	17.4	1734	Natural Gas	0.88	4.0	0.34	186	74	2.74	0.00
17.3	17.4	1734	Natural Gas	0.82	4.0	0.29	171	72	2.76	0.00
17.3	13.1	1734	Natural Gas	0.95	4.2	0.38	195	73	2.77	0.00
17.3	13.1	1734	Natural Gas	0.90	4.2	0.36	186	72	2.78	0.00
17.3	13.1	1734	Natural Gas	0.86	4.2	0.33	166	71	2.76	0.00
17.3	13.1	1734	Natural Gas	0.82	4.2	0.29	156	69	2.74	0.00
10.9	21.8	1091	Acetylene	0.64	1.5	0.90	420	78	2.82	0.00
10.9	21.8	1091	Acetylene	0.61	1.5	0.82	386	78	2.79	0.00
10.9	21.8	1091	Acetylene	0.58	1.5	0.74	435	78	2.78	0.00
10.9	21.8	1091	Acetylene	0.55	1.5	0.66	391	77	2.72	0.00
10.9	21.8	1091	Acetylene	0.52	1.5	0.57	356	76	2.60	0.00
10.9	21.8	1091	Acetylene	0.49	1.5	0.49	352	76	2.55	0.00
10.9	21.8	1091	Acetylene	0.46	1.5	0.41	298	73	2.51	0.00
10.9	21.8	1091	Acetylene	0.43	1.5	0.33	249	70	2.58	0.00
10.9	19.0	1091	Acetylene	0.73	1.4	1.10	542	79	3.00	0.00
10.9	19.0	1091	Acetylene	0.69	1.4	1.02	527	79	3.00	0.00

10.9	19.0	1091	Acetylene	0.66	1.4	0.94	493	78	2.90	0.00
10.9	19.0	1091	Acetylene	0.62	1.4	0.85	454	77	2.89	0.00
10.9	19.0	1091	Acetylene	0.59	1.4	0.76	449	77	2.88	0.00
10.9	19.0	1091	Acetylene	0.55	1.4	0.67	400	76	2.79	0.00
10.9	19.0	1091	Acetylene	0.52	1.4	0.57	361	76	2.70	0.00
10.9	19.0	1091	Acetylene	0.48	1.4	0.48	332	74	2.54	0.00
10.9	19.0	1091	Acetylene	0.45	1.4	0.39	269	71	2.47	0.00
10.9	16.3	1091	Acetylene	0.52	1.3	0.57	327	73	2.67	0.00
10.9	16.3	1091	Acetylene	0.48	1.3	0.46	283	71	2.52	0.00
10.9	16.3	1091	Acetylene	0.44	1.3	0.36	215	67	2.43	0.00
10.9	21.8	1092	Acetylene	0.64	2.4	0.90	366	75	2.93	0.00
10.9	21.8	1092	Acetylene	0.61	2.4	0.82	332	74	2.83	0.00
10.9	21.8	1092	Acetylene	0.58	2.4	0.74	313	73	2.74	0.00
10.9	21.8	1092	Acetylene	0.55	2.4	0.66	278	71	2.66	0.00
10.9	21.8	1092	Acetylene	0.52	2.4	0.57	317	73	2.68	0.00
10.9	21.8	1092	Acetylene	0.49	2.4	0.49	303	72	2.60	0.00
10.9	21.8	1092	Acetylene	0.46	2.4	0.41	269	70	2.50	0.00
10.9	21.8	1092	Acetylene	0.43	2.4	0.33	239	68	2.48	0.00
10.9	19.0	1092	Acetylene	0.69	2.4	1.02	444	75	2.97	0.00
10.9	19.0	1092	Acetylene	0.66	2.4	0.94	439	75	2.96	0.00
10.9	19.0	1092	Acetylene	0.62	2.4	0.85	425	74	2.97	0.00
10.9	19.0	1092	Acetylene	0.59	2.4	0.76	381	74	2.90	0.00
10.9	19.0	1092	Acetylene	0.55	2.4	0.67	352	73	2.84	0.00
10.9	19.0	1092	Acetylene	0.52	2.4	0.57	317	72	2.73	0.00
10.9	19.0	1092	Acetylene	0.48	2.4	0.48	278	70	2.58	0.00
10.9	19.0	1092	Acetylene	0.45	2.4	0.39	229	67	2.48	0.00
10.9	16.3	1092	Acetylene	0.64	2.2	0.89	405	72	2.98	0.00
10.9	16.3	1092	Acetylene	0.60	2.2	0.79	376	72	2.87	0.00
10.9	16.3	1092	Acetylene	0.56	2.2	0.68	327	70	2.83	0.00
10.9	16.3	1092	Acetylene	0.52	2.2	0.57	293	69	2.66	0.00
10.9	16.3	1092	Acetylene	0.48	2.2	0.46	239	67	2.55	0.00
10.9	16.3	1092	Acetylene	0.44	2.2	0.36	181	62	2.43	0.00
10.9	21.8	1093	Acetylene	0.58	3.3	0.74	483	77	2.72	0.00
10.9	21.8	1093	Acetylene	0.55	3.3	0.66	435	76	2.67	0.00
10.9	21.8	1093	Acetylene	0.52	3.3	0.57	400	75	2.62	0.00
10.9	21.8	1093	Acetylene	0.49	3.3	0.49	366	74	2.56	0.00
10.9	21.8	1093	Acetylene	0.46	3.3	0.41	317	72	2.56	0.00
10.9	21.8	1093	Acetylene	0.43	3.3	0.33	269	69	2.61	0.00
10.9	19.0	1093	Acetylene	0.55	2.8	0.67	498	77	2.78	0.00
10.9	19.0	1093	Acetylene	0.52	2.8	0.57	435	75	2.68	0.00
10.9	19.0	1093	Acetylene	0.48	2.8	0.48	356	73	2.57	0.00
10.9	19.0	1093	Acetylene	0.45	2.8	0.39	298	70	2.52	0.00
10.9	16.3	1093	Acetylene	0.52	2.7	0.57	366	72	2.61	0.00
10.9	16.3	1093	Acetylene	0.48	2.7	0.46	293	69	2.48	0.00
10.9	16.3	1093	Acetylene	0.44	2.7	0.36	200	63	2.63	0.00
10.9	21.8	1094	Acetylene	0.52	6.2	0.57	415	77	2.61	0.00
10.9	21.8	1094	Acetylene	0.49	6.2	0.49	396	76	2.57	0.00
10.9	21.8	1094	Acetylene	0.46	6.2	0.41	342	74	2.53	0.00
10.9	21.8	1094	Acetylene	0.43	6.2	0.33	264	71	2.63	0.00

10.9	19.0	1094	Acetylene	0.52	6.5	0.57	425	77	2.64	0.00
10.9	19.0	1094	Acetylene	0.48	6.5	0.48	361	74	2.53	0.00
10.9	19.0	1094	Acetylene	0.45	6.5	0.39	303	72	2.50	0.00
10.9	16.3	1094	Acetylene	0.52	6.9	0.57	386	74	2.54	0.00
10.9	16.3	1094	Acetylene	0.48	6.9	0.46	313	71	2.49	0.00
10.9	16.3	1094	Acetylene	0.44	6.9	0.36	215	66	2.61	0.00
10.9	21.8	1091	Propane	1.04	1.5	0.55	317	78	2.55	0.00
10.9	21.8	1091	Propane	0.99	1.5	0.54	313	78	2.53	0.00
10.9	21.8	1091	Propane	0.94	1.5	0.52	293	77	2.49	0.00
10.9	21.8	1091	Propane	0.89	1.5	0.49	283	76	2.47	0.00
10.9	21.8	1091	Propane	0.85	1.5	0.46	273	76	2.46	0.00
10.9	21.8	1091	Propane	0.80	1.5	0.42	244	75	2.45	0.00
10.9	21.8	1091	Propane	0.75	1.5	0.37	205	73	2.47	0.00
10.9	21.8	1091	Propane	0.70	1.5	0.32	132	68	2.60	0.00
10.9	19.0	1091	Propane	1.02	1.4	0.55	313	77	2.55	0.00
10.9	19.0	1091	Propane	0.97	1.4	0.53	293	76	2.54	0.00
10.9	19.0	1091	Propane	0.91	1.4	0.50	288	76	2.48	0.00
10.9	19.0	1091	Propane	0.86	1.4	0.47	293	76	2.50	0.00
10.9	19.0	1091	Propane	0.80	1.4	0.42	269	75	2.47	0.00
10.9	19.0	1091	Propane	0.75	1.4	0.37	239	73	2.42	0.00
10.9	19.0	1091	Propane	0.69	1.4	0.31	176	68	2.47	0.00
10.9	16.3	1091	Propane	1.06	1.3	0.55	283	76	2.65	0.00
10.9	16.3	1091	Propane	0.99	1.3	0.54	293	76	2.64	0.00
10.9	16.3	1091	Propane	0.93	1.3	0.51	273	75	2.55	0.00
10.9	16.3	1091	Propane	0.80	1.3	0.42	244	72	2.44	0.00
10.9	16.3	1091	Propane	0.74	1.3	0.36	220	71	2.43	0.00
10.9	21.8	1092	Propane	1.04	2.4	0.55	273	74	2.58	0.00
10.9	21.8	1092	Propane	0.99	2.4	0.54	283	75	2.59	0.00
10.9	21.8	1092	Propane	0.94	2.4	0.52	269	74	2.55	0.00
10.9	21.8	1092	Propane	0.89	2.4	0.49	264	74	2.53	0.00
10.9	21.8	1092	Propane	0.85	2.4	0.46	254	73	2.51	0.00
10.9	21.8	1092	Propane	0.80	2.4	0.42	234	72	2.51	0.00
10.9	21.8	1092	Propane	0.75	2.4	0.37	229	71	2.50	0.00
10.9	21.8	1092	Propane	0.70	2.4	0.32	215	69	2.50	0.00
10.9	21.8	1092	Propane	0.66	2.4	0.27	156	64	2.51	0.00
10.9	19.0	1092	Propane	1.02	2.4	0.55	273	74	2.63	0.00
10.9	19.0	1092	Propane	0.97	2.4	0.53	269	73	2.61	0.00
10.9	19.0	1092	Propane	0.91	2.4	0.50	264	73	2.58	0.00
10.9	19.0	1092	Propane	0.86	2.4	0.47	254	72	2.57	0.00
10.9	19.0	1092	Propane	0.80	2.4	0.42	239	71	2.52	0.00
10.9	19.0	1092	Propane	0.75	2.4	0.37	215	69	2.50	0.00
10.9	19.0	1092	Propane	0.69	2.4	0.31	186	66	2.48	0.00
10.9	16.3	1092	Propane	1.06	2.2	0.55	264	72	2.75	0.00
10.9	16.3	1092	Propane	0.99	2.2	0.54	264	72	2.69	0.00
10.9	16.3	1092	Propane	0.93	2.2	0.51	259	71	2.63	0.00
10.9	16.3	1092	Propane	0.86	2.2	0.47	244	70	2.58	0.00
10.9	16.3	1092	Propane	0.80	2.2	0.42	229	69	2.56	0.00
10.9	16.3	1092	Propane	0.74	2.2	0.36	200	66	2.52	0.00
10.9	16.3	1092	Propane	0.67	2.2	0.29	161	63	2.49	0.00

10.9	21.8	1093	Propane	1.04	3.3	0.55	337	77	2.55	0.00
10.9	21.8	1093	Propane	0.99	3.3	0.54	327	76	2.54	0.00
10.9	21.8	1093	Propane	0.94	3.3	0.52	308	76	2.51	0.00
10.9	21.8	1093	Propane	0.89	3.3	0.49	298	75	2.52	0.00
10.9	21.8	1093	Propane	0.85	3.3	0.46	278	74	2.49	0.00
10.9	21.8	1093	Propane	0.80	3.3	0.42	259	73	2.49	0.00
10.9	21.8	1093	Propane	0.75	3.3	0.37	229	72	2.48	0.00
10.9	21.8	1093	Propane	0.70	3.3	0.32	181	69	2.50	0.00
10.9	19.0	1093	Propane	1.02	2.8	0.55	327	76	2.58	0.00
10.9	19.0	1093	Propane	0.97	2.8	0.53	317	75	2.57	0.00
10.9	19.0	1093	Propane	0.91	2.8	0.50	313	75	2.52	0.00
10.9	19.0	1093	Propane	0.86	2.8	0.47	293	74	2.52	0.00
10.9	19.0	1093	Propane	0.80	2.8	0.42	288	73	2.50	0.00
10.9	19.0	1093	Propane	0.75	2.8	0.37	244	71	2.49	0.00
10.9	19.0	1093	Propane	0.69	2.8	0.31	186	68	2.50	0.00
10.9	16.3	1093	Propane	1.06	2.7	0.55	317	75	2.60	0.00
10.9	16.3	1093	Propane	0.99	2.7	0.54	317	74	2.59	0.00
10.9	16.3	1093	Propane	0.93	2.7	0.51	308	74	2.55	0.00
10.9	16.3	1093	Propane	0.86	2.7	0.47	283	73	2.52	0.00
10.9	16.3	1093	Propane	0.80	2.7	0.42	254	71	2.52	0.00
10.9	16.3	1093	Propane	0.74	2.7	0.36	215	68	2.48	0.00
10.9	19.0	1094	Propane	1.02	6.5	0.55	337	77	2.54	0.00
10.9	19.0	1094	Propane	0.97	6.5	0.53	322	77	2.51	0.00
10.9	19.0	1094	Propane	0.91	6.5	0.50	308	76	2.50	0.00
10.9	19.0	1094	Propane	0.86	6.5	0.47	288	75	2.49	0.00
10.9	19.0	1094	Propane	0.80	6.5	0.42	259	74	2.47	0.00
10.9	19.0	1094	Propane	0.75	6.5	0.37	200	71	2.47	0.00
10.9	16.3	1094	Propane	1.06	6.9	0.55	332	76	2.61	0.00
10.9	16.3	1094	Propane	0.99	6.9	0.54	327	76	2.55	0.00
10.9	16.3	1094	Propane	0.93	6.9	0.51	327	76	2.51	0.00
10.9	16.3	1094	Propane	0.86	6.9	0.47	288	74	2.49	0.00
10.9	16.3	1094	Propane	0.80	6.9	0.42	264	73	2.48	0.00
10.9	16.3	1094	Propane	0.74	6.9	0.36	190	68	2.50	0.00
10.9	21.8	1091	Natural Gas	1.02	1.5	0.40	278	76	2.77	0.00
10.9	21.8	1091	Natural Gas	0.95	1.5	0.38	259	75	2.80	0.00
10.9	21.8	1091	Natural Gas	0.89	1.5	0.35	229	73	2.85	0.00
10.9	21.8	1091	Natural Gas	0.82	1.5	0.30	200	71	2.91	0.00
10.9	19.0	1091	Natural Gas	1.05	1.4	0.40	273	75	2.76	0.00
10.9	19.0	1091	Natural Gas	0.97	1.4	0.39	254	74	2.78	0.00
10.9	19.0	1091	Natural Gas	0.90	1.4	0.35	234	73	2.81	0.00
10.9	19.0	1091	Natural Gas	0.82	1.4	0.30	195	69	2.94	0.00
10.9	16.3	1091	Natural Gas	1.04	1.3	0.40	269	74	2.77	0.00
10.9	16.3	1091	Natural Gas	0.95	1.3	0.38	244	73	2.79	0.00
10.9	16.3	1091	Natural Gas	0.87	1.3	0.33	220	70	2.77	0.00
10.9	16.3	1091	Natural Gas	0.82	1.3	0.30	215	69	2.79	0.00
10.9	21.8	1092	Natural Gas	1.02	2.4	0.40	254	73	2.80	0.00
10.9	21.8	1092	Natural Gas	0.95	2.4	0.38	239	72	2.81	0.00
10.9	21.8	1092	Natural Gas	0.89	2.4	0.35	229	71	2.82	0.00
10.9	21.8	1092	Natural Gas	0.82	2.4	0.30	210	69	2.83	0.00

10.9	19.0	1092	Natural Gas	1.05	2.4	0.40	239	72	2.80	0.00
10.9	19.0	1092	Natural Gas	0.97	2.4	0.39	234	71	2.81	0.00
10.9	19.0	1092	Natural Gas	0.90	2.4	0.35	225	70	2.80	0.00
10.9	19.0	1092	Natural Gas	0.82	2.4	0.30	190	67	2.78	0.00
10.9	16.3	1092	Natural Gas	1.04	2.2	0.40	234	71	2.83	0.00
10.9	16.3	1092	Natural Gas	0.95	2.2	0.38	220	69	2.85	0.00
10.9	16.3	1092	Natural Gas	0.87	2.2	0.33	210	67	2.80	0.00
10.9	16.3	1092	Natural Gas	0.82	2.2	0.30	171	65	2.78	0.00
10.9	21.8	1093	Natural Gas	1.02	3.3	0.40	303	75	2.78	0.00
10.9	21.8	1093	Natural Gas	0.95	3.3	0.38	269	74	2.80	0.00
10.9	19.0	1093	Natural Gas	1.05	2.8	0.40	298	74	2.77	0.00
10.9	19.0	1093	Natural Gas	0.97	2.8	0.39	278	73	2.81	0.00
10.9	19.0	1093	Natural Gas	0.90	2.8	0.35	259	71	2.81	0.00
10.9	19.0	1093	Natural Gas	0.82	2.8	0.30	195	67	2.92	0.00
10.9	16.3	1093	Natural Gas	1.04	2.7	0.40	288	72	2.77	0.00
10.9	16.3	1093	Natural Gas	0.95	2.7	0.38	269	71	2.79	0.00
10.9	16.3	1093	Natural Gas	0.87	2.7	0.33	239	69	2.80	0.00
10.9	16.3	1093	Natural Gas	0.82	2.7	0.30	229	67	2.82	0.00
10.9	19.0	1094	Natural Gas	1.05	6.5	0.40	288	75	2.77	0.00
10.9	19.0	1094	Natural Gas	0.97	6.5	0.39	273	74	2.78	0.00
10.9	19.0	1094	Natural Gas	0.90	6.5	0.35	244	72	2.81	0.00
10.9	16.3	1094	Natural Gas	1.04	6.9	0.40	293	74	2.75	0.00
10.9	16.3	1094	Natural Gas	0.95	6.9	0.38	278	73	2.79	0.00
10.9	16.3	1094	Natural Gas	0.87	6.9	0.33	225	70	2.82	0.00
6.4	40.2	0641	Acetylene	0.71	0.8	1.05	767	80	2.76	2.13
6.4	40.2	0641	Acetylene	0.66	0.8	0.94	718	79	2.73	2.21
6.4	40.2	0641	Acetylene	0.61	0.8	0.82	669	78	2.71	2.41
6.4	40.2	0641	Acetylene	0.56	0.8	0.69	601	77	2.55	2.27
6.4	40.2	0641	Acetylene	0.51	0.8	0.56	464	74	2.50	2.44
6.4	40.2	0641	Acetylene	0.46	0.8	0.42	376	71	2.56	2.13
6.4	32.2	0641	Acetylene	0.76	0.8	1.16	688	77	2.43	2.25
6.4	32.2	0641	Acetylene	0.70	0.8	1.03	669	76	2.52	2.31
6.4	32.2	0641	Acetylene	0.64	0.8	0.88	601	75	2.54	2.17
6.4	32.2	0641	Acetylene	0.58	0.8	0.73	562	74	2.49	2.21
6.4	32.2	0641	Acetylene	0.51	0.8	0.56	459	72	2.33	2.68
6.4	32.2	0641	Acetylene	0.45	0.8	0.40	337	69	2.33	2.99
6.4	48.3	0642	Acetylene	0.59	0.8	0.77	630	79	2.60	2.39
6.4	48.3	0642	Acetylene	0.55	0.8	0.67	586	78	2.53	2.54
6.4	48.3	0642	Acetylene	0.51	0.8	0.55	479	76	2.47	2.53
6.4	40.2	0642	Acetylene	0.71	0.8	1.05	771	81	2.79	2.19
6.4	40.2	0642	Acetylene	0.66	0.8	0.94	728	80	2.79	2.15
6.4	40.2	0642	Acetylene	0.61	0.8	0.82	659	78	2.72	2.38
6.4	40.2	0642	Acetylene	0.56	0.8	0.69	576	76	2.53	2.32
6.4	40.2	0642	Acetylene	0.51	0.8	0.56	479	74	2.46	2.53
6.4	32.2	0642	Acetylene	0.76	0.7	1.16	723	78	2.75	2.02
6.4	32.2	0642	Acetylene	0.70	0.7	1.03	664	77	2.73	2.41
6.4	32.2	0642	Acetylene	0.64	0.7	0.88	601	76	2.65	2.34
6.4	32.2	0642	Acetylene	0.58	0.7	0.73	557	75	2.53	2.18
6.4	32.2	0642	Acetylene	0.51	0.7	0.56	444	72	2.38	2.72

6.4	32.2	0643	Acetylene	0.76	0.8	1.16	801	79	2.80	1.94
6.4	32.2	0643	Acetylene	0.70	0.8	1.03	723	77	2.81	2.24
6.4	32.2	0643	Acetylene	0.64	0.8	0.88	684	77	2.79	2.32
6.4	32.2	0643	Acetylene	0.58	0.8	0.73	596	75	2.67	2.37
6.4	32.2	0643	Acetylene	0.51	0.8	0.56	513	73	2.56	2.54
6.4	32.2	0643	Acetylene	0.45	0.8	0.40	400	70	2.54	2.89
6.4	24.1	0643	Acetylene	0.60	0.8	0.79	625	73	2.59	2.28
6.4	24.1	0643	Acetylene	0.52	0.8	0.57	469	70	2.44	2.50
6.4	32.2	0644	Acetylene	0.66	2.4	0.93	854	77	2.43	1.97
6.4	32.2	0644	Acetylene	0.60	2.4	0.78	728	75	2.40	1.94
6.4	32.2	0644	Acetylene	0.53	2.4	0.62	640	73	2.41	1.98
6.4	24.1	0644	Acetylene	0.79	2.3	1.22	962	78	2.66	2.34
6.4	24.1	0644	Acetylene	0.71	2.3	1.05	879	77	2.64	2.28
6.4	24.1	0644	Acetylene	0.63	2.3	0.86	781	75	2.56	2.03
6.4	24.1	0644	Acetylene	0.54	2.3	0.65	586	71	2.34	2.11
6.4	32.2	0641	Propane	1.09	0.8	0.55	396	73	2.42	0.00
6.4	32.2	0641	Propane	0.99	0.8	0.54	386	73	2.39	0.00
6.4	32.2	0641	Propane	0.90	0.8	0.49	347	72	2.42	0.00
6.4	32.2	0641	Propane	0.80	0.8	0.42	313	71	2.46	0.00
6.4	24.1	0641	Propane	1.06	0.8	0.55	327	70	2.34	0.00
6.4	24.1	0641	Propane	0.94	0.8	0.52	327	69	2.29	0.00
6.4	24.1	0641	Propane	0.81	0.8	0.43	303	68	2.23	0.00
6.4	32.2	0642	Propane	1.09	0.7	0.55	371	74	2.50	0.00
6.4	32.2	0642	Propane	0.99	0.7	0.54	371	74	2.43	0.00
6.4	32.2	0642	Propane	0.90	0.7	0.49	327	72	2.43	0.00
6.4	32.2	0642	Propane	0.80	0.7	0.42	273	70	2.50	0.00
6.4	24.1	0642	Propane	1.06	0.6	0.55	347	71	2.37	0.00
6.4	24.1	0642	Propane	0.94	0.6	0.52	342	71	2.31	0.00
6.4	24.1	0642	Propane	0.81	0.6	0.43	308	68	2.30	0.00
6.4	32.2	0643	Propane	1.09	0.8	0.55	420	74	2.49	0.00
6.4	32.2	0643	Propane	0.99	0.8	0.54	381	73	2.46	0.00
6.4	24.1	0643	Propane	1.06	0.8	0.55	361	72	2.42	0.00
6.4	24.1	0643	Propane	0.94	0.8	0.52	352	71	2.36	0.00
6.4	24.1	0641	Natural Gas	1.08	0.0	0.40	308	69	2.49	0.00
6.4	24.1	0641	Natural Gas	0.99	0.0	0.39	298	69	2.54	0.00
6.4	24.1	0641	Natural Gas	0.90	0.0	0.36	259	67	2.59	0.00
6.4	32.2	0642	Natural Gas	1.01	0.7	0.40	293	71	2.73	0.00
6.4	32.2	0642	Natural Gas	0.94	0.7	0.38	254	69	2.82	0.00
6.4	32.2	0642	Natural Gas	0.88	0.7	0.34	200	66	2.91	0.00
6.4	24.1	0642	Natural Gas	1.08	0.6	0.40	288	70	2.56	0.00
6.4	24.1	0642	Natural Gas	0.99	0.6	0.39	283	69	2.55	0.00
6.4	24.1	0642	Natural Gas	0.90	0.6	0.36	254	67	2.58	0.00
6.4	24.1	0643	Natural Gas	1.08	0.8	0.40	317	70	2.64	0.00
6.4	24.1	0643	Natural Gas	0.99	0.8	0.39	313	69	2.70	0.00
6.4	24.1	0643	Natural Gas	0.90	0.8	0.36	273	67	2.79	0.00

REFERENCES

[1] S. Nair "Acoustic Characterization of Flame Blowout Phenomenon",Ph.D., Georgia Institute of Technology, 2006.

[2] M. J. Lighthill "On sound generated aerodynamically. II. Turbulence as a source of sound", Proceedings of the Royal Society of London, Series A (Mathematical and Physical Sciences), 222, 1954, 1-32.

[3] S. L. Bragg "Combustion noise", Journal of the Institute of Fuel, 36, 1963, 12-16.

[4] W. C. Strahle "On Combustion Generated Noise", Journal of Fluid Mechanics, 49, 1971, 399-414.

[5] W. C. Strahle "Combustion Noise", Progress in Energy and Combustion Science, 4, 1978, 157-176.

[6] H. A. Hassan "Scaling of Combustion-Generated Noise", Journal of Fluid Mechanics, 66, 1974, 445-453.

[7] H. H. Chiu and M. Summerfield "Theory of Combustion Noise", Princeton University Report 1136.

[8] P. E. Doak "Analysis of Internally Generated Sound in Continuous Materials. III. The Momentum Potential Field Description of Fluctuating Fluid Motion as a Basis for a Unified Theory of Internally Generated Sound", Journal of Sound and Vibration, 26, 1973, 91-120.

[9] S. Kotake "On Combustion Noise Related to Chemical Reactions", Journal of Sound and Vibration, 42, 1975, 399-410.

[10] D. G. Crighton, A. P. Dowling, J. E. Ffowcs Williams, M. Heckl and F. G. Leppington "Modern Methods in Analytical Acoustics", Springer, Berlin, 1992.

[11] A. P. Dowling "Mean Temperature and Flow Effects on Combustion Noise", AIAA Paper 1979-0590.

[12] W. C. Strahle "Refraction, Convection and Diffusion Flame Effects in Combustion Generated Noise", 1973.

[13] W. C. Strahle "A More Modern Theory of Combustion Noise", Plenum Press, New York, NY, 1985, 103-114.

[14] R. D. Giammar and A. A. Putnam "Combustion Roar of Premix Burners, Singly and in Pairs", Combustion and Flame, 18, 1972, 435-438.

[15] W. C. Strahle and B. N. Shivashankara "A Rational Correlation of Combustion Noise Results from Open Turbulent Premixed Flames", Combust Inst, Pittsburgh, Pa, 1974.

[16] P. Clavin and E. D. Siggia "Turbulent Premixed Flames and Sound Generation", Combustion Science and Technology, 78, 1991, 147-155.

[17] P. Clavin "Dynamics of Combustion Fronts in Premixed Gases: From Flames to Detonations", Combust Inst, Pittsburgh, Pa, USA, 2000.

[18] R. G. Huff "Theoretical Prediction of the Acoustic Pressure Generated by Turbulence-Flame Front Interactions", Journal of Vibration, Acoustics, Stress, and Reliability in Design, 108, 1986, 315-321.

[19] J.-M. Truffaut, G. Searby and L. Boyer "Sound Emission by Non-Isomolar Combustion at Low Mach Numbers", Combustion Theory and Modelling, 2, 1998, 423-428.

[20] R. B. Price, I. R. Hurle and T. M. Sugden "Optical Studies of the Generation of Noise in Turbulent Flames", Combust Inst, Pittsburgh, Pa, USA, 1968.

[21] B. N. Shivashankara, W. C. Strahle and J. C. Handley "Evaluation of Combustion Noise Scaling Laws by an Optical Technique", AIAA Journal, 13, 1975, 623-627.

[22] G. K. Mehta, M. K. Ramachandra and W. C. Strahle "Correlations between Light Emission, Acoustic Emission and Ion Density in Premixed Turbulent Flames", Combust Inst, Pittsburgh, Pa, USA, 1981.

[23] J. S. Fox and C. Bertrand "Use of Saturation Currents as a Measure of Combustion Noise in Premixed Flames", Combust Inst, Pittsburgh, Pa, USA, 1981.

[24] J. Wäsle, A. Winkler and T. Sattelmayer "Spatial coherence of the heat release fluctuations in turbulent jet and swirl flames", Flow, Turbulence and Combustion, 75, 2005, 29-50.

[25] B. N. Shivashankara and R. W. Crouch "Noise Characteristics of a Can-Type Combustor", Journal of Aircraft, 14, 1977, 751-756.

[26] D. C. Mathews and N. F. Rekos "Prediction and Measurement of Direct Combustion Noise in Turbopropulsion Systems", Journal of Aircraft, 14, 1977, 850-859.

[27] E. A. Krejsa "Combustion Noise From Gas Turbine Aircraft Engines Measurement of Far-Field Levels", NASA-TM-88971.

[28] C. K. W. Tam, N. N. Pastouchenko, J. Mendoza and D. Brown "Combustion Noise of Auxiliary Power Units", AIAA Paper 2005-2829.

[29] N. A. Cumpsty "Jet Engine Combustion Noise: Pressure, Entropy and Vorticity Perturbations produced by Unsteady Combustion or Heat Addition", Journal of Sound and Vibration, 66, 1979, 527-544.

[30] M. Muthukrishnan, W. C. Strahle and D. H. Neale "Separation of Hydrodynamic, Entropy, and Combustion Noise in a Gas Turbine Combustor", AIAA Journal, 16, 1978, 320-327.

[31] B. N. Shivashankara "Gas Turbine Core Noise Source Isolation by Internal-to-Far-Field Correlations", Journal of Aircraft, 15, 1978, 597-600.

[32] E. A. Krejsa "New Technique for the Measurement of Core Noise from Aircraft Engines", AIAA Paper 1981-1587.

[33] E. A. Krejsa "Application of 3-Signal Coherence to Core Noise Transmission", 1983,

[34] A. A. Putnam "Combustion Roar of Seven Industrial Gas Burners", Journal of the Institute of Fuel, 49, 1976, 135-138.

[35] J. K. Kilham and N. Kirmani "The Effect of Turbulence on Premixed Flame Noise", Combust Inst, Pittsburgh, Pa, 1979.

[36] J. P. Roberts and H. G. Leventhall "Noise Sources in Turbulent Gaseous Premixed Flames", Applied Acoustics, 6, 1973, 301-308.

[37] American Gas Institute Report BR-3-5, "Guide for the Design of Low Noise Level Combustion Systems", 1971.

[38] J. R. Mahan "A Critical Review of Noise Prodiction Models for Turbulent, Gas-Fueled Burners", NASA Contractor Report 3803.

[39] K. N. R. Ramohalli and P. K. Seshan "Acoustic Emissions Reveal Combustion Conditions",

[40] F. E. J. Briffa, C. J. Clark and G. T. Williams "Combustion Noise", Journal of the Institute of Fuel, 46, 1973, 207-216.

[41] S. Kotake and K. Takamoto "Combustion Noise: Effects of the Shape and Size of Burner Nozzle", Journal of Sound and Vibration, 112, 1987, 345-354.

[42] R. N. Kumar "Further Experimental Results on the Structure and Acoustics of Turbulent Jet Flames", AIAA paper 1975-0523.

[43] G. Petela and R. Petela "Diagnostic Possibilities on the Basis of Premixed Flame Noise Levels", Combustion and Flame, 52, 1983, 137-147.

[44] S. Kotake and K. Takamoto "Combustion Noise: Effects of the Velocity Turbulence of Unburned Mixture", Journal of Sound and Vibration, 139, 1990, 9-20.

[45] T. J. B. Smith and J. K. Kilham "Noise Generation by Open Turbulent Flames", Journal of the Acoustical Society of America, 35, 1963, 715-724.

[46] R. Rajaram and T. Lieuwen "Parametric Studies of Acoustic Radiation from Turbulent Premixed Flames", Combustion Science and Technology, 175, 2003, 2269-2298.

[47] B. N. Shivashankara, W. C. Strahle and J. C. Handley "Combustion Noise Radiation by Open Turbulent Flames", Progress in Astronautics and Aeronautics, 37, 1975, 277-296.

[48] W. C. Strahle "Combustion Noise Source", Noise Control Foundation, Poughkeepsie, NY, USA, 1983, 379-388.

[49] J. Stephenson and H. A. Hassan "Spectrum of Combustion-Generated Noise", Journal of Sound and Vibration, 53, 1977, 283-288.

[50] D. I. Abugov and O. I. Obrezkov "Acoustic Noise in Turbulent Flames", Combustion, Explosion, and Shock Waves, 14, 1978, 606-612.

[51] A. Belliard "Etude expérimentale de l'émission sonore des flammes turbulentes",PhD Thesis, Universités d'Aix-Marseille, 1997.

[52] T. J. B. Smith "Combustion Noise",PhD Thesis, The University of Leeds, 1961.

[53] B. N. Shivashankara "An Experimental Study of Noise Produced by Open Turbulent Flames",Georgia Institute of Technology, 1974.

[54] B. D. Videto and D. A. Santavicca "A Turbulent Flow System for Studying Turbulent Combustion Porcess", Combustion Science and Technology, 76, 1991, 159-164.

[55] K. K. Ahuja "Designing clean jet-noise facilities and making accurate jet-noise measurements", International Journal of Aeroacoustics, 2, 2003, 371-412.

[56] ISO 3745:2003, "Acoustics Determination of Sound Power Levels of Noise Sources using Sound Pressure Precision Methods for Anechoic and Hemi-anechoic Rooms", 2003.

[57] J. S. Bendat and A. G. Piersol "Random data : analysis and measurement procedures", Wiley, 2000.

[58] J. Wäsle, A. Winkler and T. Sattelmayer "Influence of the Combustion Mode on Acoustic Spectra of Open Turbulent Swirl Flames", 2005.

[59] A. Winkler, J. Wäsle and T. Sattelmayer "Experimental Investigations on the Acoustic Efficiency of Premixed Swirl Stabilized Flames ", AIAA paper 2005-2908

[60] E. A. Krejsa "Application of 3-Signal Coherence to Core Noise Transmission", AIAA Paper 1983-0759.

[61] P. Saussus and K. A. Cunefare "Sound Sources for Anechoic Chamber Qualification", Noise Conference, 2003.

[62] K. A. Cunefare, V. B. Biesel, J. Tran, R. Rye, A. Graf, M. Holdhusen and A.-M. Albanese "Anechoic chamber qualification: Traverse method, inverse square law analysis method, and nature of test signal", Journal of the Acoustical Society of America, 113, 2003, 881-892.